NANOSTRUCTURED PHOSPHORUS-BASED COMPOUNDS AND THEIR APPLICATION TOWARDS ELECTROCHEMICAL HYDROGEN GENERATION

ANKUSH

A thesis submitted for the partial fulfilment of

the degree of Doctor of Philosophy

Institute of Nano Science and Technology (INST) Mohali

Knowledge City, Sector 81, SAS Nagar, Manauli, P.O. 140306, Punjab, India

Indian Institute of Science Education and Research (IISER) Mohali

Knowledge City, Sector 81, SAS Nagar, Manauli, P.O. 140306, Punjab, India

November 2022

Dedicated to
my family

Declaration

The work presented in this thesis has been carried out by me under the guidance of Dr. Menaka Jha at the Institute of Nano Science and Technology, Mohali, India. This work has not been submitted in part or in full for a degree, a diploma, or a fellowship to any other university or institute. Whenever contributions of others are involved, every effort is made to indicate this clearly, with due acknowledgement of collaborative research and discussions. This thesis is a bonafide record of original work done by me and all sources listed within have been detailed in the bibliography.

Ankush

In my capacity as the supervisor of the candidate's thesis work, I certify that the above statements made by the candidate are true to the best of my knowledge.

Dr. Menaka Jha

Acknowledgement

This endeavor would not have been accomplished without the support of countless people.

I wish to express my gratitude to my supervisor **Dr. Menaka Jha** for her support, encouragement, valuable suggestions and motivating guidance. It was a privilege to work with her. Her immense knowledge helped me in conducting the research and writing of this thesis. Thank you so much for being so understanding and supportive over the past five years.

I also appreciate my Ph.D. committee members, **Dr. Kamalakannan Kailasam** and **Dr. Vivek Bagchi** who generously provided feedback, suggestions and knowledge during each evaluation years. I would also like to thanks **Prof. Amitava Patra**, Director, INST and **Prof. Ashok Kumar Ganguli**, founding Director, INST Mohali for infrastructure and support. Additionally, this endeavor would not have been possible without the financial support from the CSIR, India. I would like to acknowledge INST administration, technical and support staff.

A big appreciation and great thanks to all the members of my C-12 lab, first and foremost my senior and roommate **Dr. Krishna Kumar** Yadav who helped me to learn the new tools and techniques during the initial years of my Ph.D, **Dr. Sunaina** for her kind help and support, **Dr. Sujit** and his wife (Paromita bhabi), who were always there to give valuable suggestions, guidance and amazing fish curry recipes for us. I would like to thank **Ms. Ritika** (clean room), for her help in experiments and lab work throughout my Ph.D. I am grateful to **Ms. Supriya** (Chutki) for her argumentative nature, who was always ready to fight in which I always used to win. However, you were always my best friend and I am thankful for your help and support during my Ph.D. I would like to appreciate a Korean-Chinese girl, **Ms. Kritika**, who is nice and cool and **Ms. Arushi** (Aloo Burger) for her kind and helpful nature. I would also like to thank other members of our lab including **Nausad** (zombie), **Sapna**, **Sushma**, Anima, Heena, Bilal Ahmed, Muskan and Harish for their help in the lab, I enjoyed working with them.

This journey would not have been possible without friends, who were always there for help, enjoyment and encouragement. I would like to appreciate one of my best friends, **Dr. Navneet** who was always there to help me in the presentations and accompanying me during

shopping. I would also thank my roommates, **Dr. Krishna** (sleeping owl), **Dr. Venu** (baiya G) and **Dr. Naimat** for the room parties, food recipes from different states together and their great company. I am thankful to so called roommates **Sushil** (for spicy food) and **Ashish Bhatt** (Chakhna-chor) on weekend parties. I am also thankful to **Dr. Zubair** (kanjoos) who was always short of money but still managed to hang out with us on loan basis.

I am thankful to my batchmates Mujeeb, Tanmay, Vianni, Rimple, Shikha, Aakriti, Gaurav and Avinash for their help during initial years of Ph.D which make my stay comfortable in INST.

I want to extend my gratitude to INST researcher scholars including Dr. Rajinder, Dr. Sunil, Dr. Kalpesh, Mujeeb, Deepak, Rohit, Mayank, Jasveer, Hitasha, Saumadri, Riyaj, Rejaul, Neha, Pushpendra, Anas, Aditi, Arti, Arshdeep, Deepika, Pulkit, Ravi, Satish, Vibhav, Ajit, Hari, Anamika, Mansi, Devender, Ajay, Bhawna, Arpana, choti Neha, Priyanka, Himadri, Mamta, Anshu, Bibek, Manish, Taniya, Navpreet, Manisha, Subhajit, Varun, KK, Vikas, Ashish, Ashima, Sonu, Rakesh, Dr. Jha throughout my journey. I am thankful to instrument operators Ashwinder, Baljeet and Neha.

I would like to thank cricket, volley ball and football team especially **Chirag** for arranging inter-institute matches during weekends. I really enjoyed playing with them and for the memorable moments. I am thankful to cycling group for our morning cycle trips to sukhna lake during lockdown. I would also like to thank badminton friends with whom I used to play after a whole day of work and I had a great time playing with my badminton partner **Dr. Nand**. I am also thankful to chai group for debates during tea time.

Lastly, I would like to acknowledge my parents, mother and father for their support, trust and encouragement in every phase of my life. I would also like to thanks my brother and my sister for always being there as friend and to support me in my decision.

I dedicate this thesis to all of them, as it would not have been possible without any of them.

Ankush

Abbreviations

SEM	***Scanning electron microscopy***
FESEM	***Field emission scanning electron microscopy***
TEM	***Transmission electron microscopy***
SAED	***Selected area electron diffraction pattern***
EDX	***Energy-dispersive X-ray spectroscopy***
HRTEM	***High resolution transmission electron microscopy***
STEM	***Scanning transmission electron microscopy***
XPS	***X-ray photoelectron spectroscopy***
UV-vis	***Ultraviolet-visible***
Ω	***Ohm***
CPE	***Constant phase element***
Y_0	***CPE constant***
Ω	***Angular frequency***
N	***Exponent of CPE***
RHE	***Revirsible hydrogen electrode***
PXRD	***Powder X-ray diffraction***
HTXRD	***High-temperature X-ray diffraction***
2θ	***Bragg's angle***
D	***Interplanar distances***
(hkl)	***Miller indices***
AFM	***Atomic force microscopy***
CPD	***Contact potential difference***
TGA	***Thermogravimetric analysis***
DTA	***Diffrantial thermogravimetric analysis***
BET	***Brunauer-Emmett-Teller***
BJH	***Barrett-Joyner-Halenda***
nm	***Nanometer***
Mm	***Millimetre***
TX 100	***Triton X-100***

Min	***Minutes***
eV	***Electronvolt***
IR	***Infrared***
mA	***Milliampere***
μA	***Microampere***
Cm	***Centimeter***
Λ	***Wavelength***
Å	***Angstrom***
N	***Wavenumber***
H	***Plank's constant***
M	***Micro***
J	***Current density***
E	***Electric field***
A_R	***Richardson constant***
k	***Boltzmann constant***
nA	***Nanoampere***
Φ	***Work function***
mL	***Milliliter***
LSV	***Linear sweep voltammetry***
CV	***Cyclic voltammetry***
MS	***Mott- schottkey***
EIS	***Electrochemical impedance spectroscopy***
HER	***Hydrogen evolution reaction***
OER	***Oxygen evolution reaction***
E_{CB}	***Conduction band edge***
E_{VB}	***Valence band edge***
Wt %	***Weight percentage***
V/V %	***Volume percentage***
w/w	***Weight by weight***
t	***Time***
JCPDS	***Joint Committee on Powder Diffraction Standards***

mA	***Milliampere***
V	***Voltage***
w. r. t.	***with respect to***
ln	***Natural logarithm***
Log	***Logarithm***
i. e.	***That is***
T	***Temperature***
h	***Hours***
s	***Seconds***
M	***Molar***
g	***Gram***
mg	***Milligram***
H_2SO_4	***Sulphuric acid***
PPT	***Part per trillion***
PPM	***Part per million***
Si	***Silicone***
$Co_2P_4O_{12}$	***Cobalt cyclotetraphosphate***
$Ni_2P_4O_{12}$	***Nickel cyclotetraphosphate***
$CoNiP_4O_{12}$	***Cobalt nickel cyclotetraphosphate***
rGO	***Reduced graphene oxide***
Co_2P	***Cobalt phosphide***
FeP	***Iron phosphide***
ECSA	***Electrochemical active surface area***
Rs	***Solution resistance***
GS	***Graphite sheet***
CG	***Graphene oxide***
UG	***Nitrogen-doped graphene oxide***
KOH	***Potassium hydroxide***
EDLC	***Electric double-layer capacitance***
CA	***Contact angle***
R_{ct}	***Charge transfer resistance***

Abstract

The development of sustainable, eco- friendly and renewable energy sources is required to address the increasing demand for energy and environmental concerns. Hydrogen (H_2) is one of the most appealing renewables for future energy applications. At present, steam methane reforming method is used for large scale production of hydrogen which also consumes conventional fossil fuels and releases greenhouse gases such as CO_2. The generation of hydrogen through water splitting gains much researcher's attention due to no generation of carbon footprint. Hydrogen production from the electrolysis of water is one of the superior techniques owing to the production of high purity hydrogen at large scale without emission of greenhouse gases. The electrolysis of water is carried out in two half-reactions, which are hydrogen evolution reaction (HER) and oxygen evolution reaction (OER). The well-known equation for half-cell reaction of HER is $2H^+ (aq) + 2e^- \rightarrow H_2 (g)$. To carry out this half-cell reaction, materials based on platinum are considered as the best electrocatalyst. However, the expensive nature of platinum and its less abundancy make them obstructed to be used in large scale production of H_2. Therefore developing cost-effective and highly efficient electrocatalysts for the hydrogen evolution reaction (HER) is critical to promoting hydrogen generation from mild techniques. In the present thesis, we have developed a low-temperature process to synthesize ultrathin $Co_2P_4O_{12}$ and $Ni_2P_4O_{12}$ nanosheets. The $Co_2P_4O_{12}$ and $Ni_2P_4O_{12}$ nanosheets show an efficient catalytic activity towards HER and high stability due to presence of $P_4O_{12}^{4-}$ cyclic ring in acidic medium. Further, the catalytic activity of metal cyclotetraphosphate was enhanced by synergistic effect of bimetallic cyclotetraphosphates ($CoNiP_4O_{12}$). Despite that composite of bimetallic cyclotetraphosphates with reduced graphene oxide (rGO) has also been explored to increase its surface area and electronic properties. We have also investigated transition metal phosphides for HER. In this we have synthesized cobalt phosphide (Co_2P) nanorods and iron phosphide (FeP) nanoparticles. Co_2P nanorods and FeP nanoparticles shows an excellent activity towards HER in an acidic media.
In summary, this thesis focuses on stabilization of various phosphorous based materials and demonstrates the potential of their electrocatalytic properties. The synthesized materials showed promising catalytic activity towards hydrogen generation.

Table of Contents

List of Figures

List of Tables

Chapter 1

Introduction

1.1. Renewable energy for sustainable development

Nature basically evolved from closed material cycles in which the resources underwent numerous chemical transformations. Finally, at a particular stage, it branches off to the initial product to guarantee a perspective of the material energy supply. In nature, there are numerous examples of this concept, such as the oxygen, carbon, and nitrogen cycles.[1,2] More resources than ever before have been exploited without remorse, especially since the beginning of the industrialization and urbanization scenario. As a result, humanity has many challenges to overcome. Due to the dramatically expanding demand and the deteriorating environment brought on by the use of fossil fuels, energy and the environment are two of the major ever-growing concerns of modern human society.[3] The exponential rise in energy consumption caused by the expansion of the global economy and human population has only recently been met by increased production of fossil fuels like coal, oil, or gas, which are expected to run out in about 100 years.[4] Since the beginning of the industrial age, fossil fuels like coal and oil have been the world's main source of energy. Currently, these sources provided 70% of the world's energy needs.[5,6] The advantage of fossil fuels is that they contain concentrated free energy. It took thousands of years for these intricate molecules to evolve naturally into their current state. It also has the benefit of being relatively simple to extract energy through the consumption of these fuels. However, these non-renewable energy sources cause serious environmental issues since they release carbon dioxide.[4,7] The global energy consumption in 2012 was 5.79 $*10^{20}$ J, while the potential energy demand is predicted to increase to 8.60 * 10^{20} J by 2040. Additionally, according to the International Energy Agency, global energy demand will rise by 30% until 2040, and CO_2 emissions would nearly triple to 35.7 Gt annually by that time.[8–10] The extensive usage of natural fuels increases both the amount of greenhouse gases emitted and energy consumption. In the modern world, resources are becoming scarce; greenhouse gas emissions are showing major impact as increase in global warming. Additionally, fossil fuels cannot be considered an ideal energy source due to inequities in global distribution, declining accessibility, and widespread environmental problems. If the appropriate action is not taken, the "Intergovernmental Panel on Climate Change" has already warned that average surface temperatures and atmospheric CO_2 concentrations will rise.[11,12] The sustainable development of environment friendly, carbon-neutral energy sources is forcing scientists to discover a new alternative to meet the

world's energy needs. This critical issue has now become a global challenge. The majority of nations are making efforts to meet energy needs and reduce carbon emissions. These issues drove scientists and the general public to seek out alternative conversion technologies that would be environmentally benign and able to meet both household demands and requirements.[8] The majority of energy demand supply comes from fossil fuels, although there is a strong trend toward replacing fossil fuels with renewable resources including solar, wind, and hydro energy, among others. Our current technological capabilities have already made it possible for us to use alternative sources of energy like wind, turbines, solar cells, biomass plants, and more.[10] The significant investment made in the research and development of renewable energy sources has led to an increase in their proportion of the world's electricity output. Numerous obstacles need to be overcome with the goal of increasing renewable energy's contribution to businesses and households on a daily basis. The production of energy from unconventional sources like the sun and wind is limited by the laws of nature rather than being endowed with an endless supply of energy. Additionally, we must take into account elements like the economy, the environment, and human health when considering the utilization of renewable energy sources.[13] As a result, a cleaner, carbon-neutral fuel would ultimately be a superior option, especially in light of the current energy crisis and the need to store intermittent energy supply. Using these many energy sources, whether there is a surplus or a shortage of renewable energy, is one approach to reduce the demand for energy. These renewable energy sources are unpredictable and if they are not used wisely, energy will be wasted. Utilizing all the energy generated during the fullest production hours is not always simple. If it were feasible to somehow store energy during peak production hours and release it when needed, it might completely shift the landscape of renewable energy.[6] The main focus right now is on either properly storing energy or connecting to an energy storage system. The widely used storage methods of today are a part of a system that includes mechanical storage, thermal storage and batteries.[13,14] Each type of storage technology has advantages and disadvantages of its own. All of these technologies will be covered in the section that follows.

1.2. Hydrogen: Future of clean energy

The addressing of global energy issues in near future using the chemical fuels derived from renewable sources will be one of the biggest accomplishments. One of the key scientific

issues of the twenty-first century is the generation of hydrogen from water splitting. A molecule that is readily available and may be found in our surroundings in both gaseous and liquid form is hydrogen. Hydrogen is used as a future energy carrier despite having the highest energy content by weight but the lowest energy content by volume. Compared to petroleum, hydrogen has a heating value that is three times greater and produces no hazardous emissions.

1.3. Hydrogen economy for sustainable development

The phrase "hydrogen economy" was initially used by J. B. S. Haldane and Professor John Bockris.[15] The economy primarily focused on the idea of hydrogen being used as a viable fuel source because it is one of the safest and clean energy sources available. Despite these appealing characteristics, molecular hydrogen is not abundantly available and must be produced from various hydrogen-combined sources using a variety of energy sources.[16,17] Since the economy is still developing, it's possible that one of the biggest infrastructure projects will involve it in the near future. It is mainly associated with hydrogen reservoirs, their transfer, and its usage in various ways. Because of its carbon-free byproducts, hydrogen is an appealing energy transporter and potentially one of the clean energy sources. Thus, the development of what is now known as the hydrogen economy is required to explore the cleanest and safest carbon-free energy reservoir. There is no question that the transition from traditional energy-based technology to hydrogen-based technology will solve many of the world's energy and environment related concerns in the near future. The hydrogen economy revolved around the manufacture, distribution, and use of hydrogen rather than fossil fuels.[9,18] As previously stated, the majority of energy-storing equipment has been created solely for electric energy storage, but hydrogen storage is a very distinct concept. Hydrogen is highly dependent on the chemical sector because it lacks natural resources. The 1973 oil crisis was a major influence in recognizing the necessity of the alternate energy sources. The idea of hydrogen energy was initially introduced during this period. The first conference devoted to the production, use, and marketing of hydrogen took place in 1974, and a group called the "International association from hydrogen energy" was established. The organization's primary goal is to use and promote hydrogen as an energy carrier in the energy industry and businesses that are related to energy. The potential of hydrogen as a revolutionary material for various industries has enhanced its scalability. The optimization of

hydrogen-based industries is now being advanced. It is extremely difficult to determine whether industrialization is even feasible when all energy sources must first be converted into hydrogen-based technologies due to technical limitations of the existing infrastructure.[17,19,20] Efforts are being made worldwide for the promotion and establishment of this change, which is technically based on the hydrogen economy. Fuel reservoirs, which will be depleted in the near future, have had a significant impact on the extraction of hydrogen from fossil fuels. Therefore, it is vital to switch from one technology to another while actively looking for non-fossil fuel sources of hydrogen. The transportation, energy, and industrial sectors, as well as the defense and aviation industries, among others, would present numerous opportunities. In the near future, it is anticipated that inexhaustible energy sources will be able to meet the growing energy demands for hydrogen generation.

1.4. Significance of hydrogen economy

A fundamental component of the earth, hydrogen is most frequently found in water (H_2O). More and more artificial hydrogen is created as a result of industrialization, and this production is essential to the advancement of human society. The following methods are typically used to produce hydrogen[21]:

- Hydrogen production from partial oxidation or steam reforming process using fossil fuels
- Electrolysis of saline in soda factories, iron manufacture, ethylene production, and oil refineries
- Methane fermentation and steam gasification processes
- Photocatalysis, Electrocatalysis etc.

Artificially produced hydrogen is typically used in industrial processes such as the manufacturing of ammonia, methanol, and metals, furthermore providing power for rockets and fuel cells. Thus, hydrogen being an essential intermediate product for industrial operations is not a surprise, when both production and consumption are taken into account. However, hydrogen properties like high energy density and water as a byproduct are what make it relevant to sustainable development. Despite not being an energy resource that occurs naturally on Earth, hydrogen has a huge potential to assist sustainable growth as a clean and efficient energy source for the production of clean renewable energy. Hydrogen has the highest mass energy density of any fuel (120 MJ/kg); it is considered as a great

medium of energy storage and transport. In the early 1970s, Gregory et al. showed the advantages of using hydrogen as a carrier for long-distance energy transfer. Compared to power transmission via high-voltage lines, transporting hydrogen through a pipeline would be substantially more cost-efficient and economical, excluding the expense of infrastructure building. At that time, it seemed difficult to build a pipeline network just for transporting hydrogen due to the high initial investment. More options for transporting hydrogen have recently become available, such as using 278 Hydrogen Economy pressurized tanks, fuel cells, or existing pipes that could provide a low-cost regional hydrogen network (however the issue of hydrogen embrittlement in existing pipelines needs to be solved).[22] Furthermore, the widespread use of FCVs (fuel cell vehicles) will result in the formation of a hydrogen network via road transportation infrastructure. In the near future, it is anticipated that hydrogen transportation cost will drop significantly.[17] Hydrogen is the best option for both short-term and long-term energy storage when it comes to cost, efficiency and ease of energy conversion, especially when a lot of storage is required (*Table 1.1*).

Table 1.1. Energy Storage Technologies

Technology	Power capacity	Discharge duration
Supercapacitors	10 kW-10 MW	Seconds
Flywheel	10 kW-10 MW	Seconds -minutes
Battery	1 kW-100 MW	Seconds-days
Compressed Air Energy Storage	100 MW-1 GW	Hours -weeks
Pumped Hydrogen Storage	100 MW-1 GW	Minutes-weeks
Hydrogen	100 MW-1 GW	Hours-seasons

On the other hand, hydrogen might be extensively used during FCVs and power generation systems for businesses and homes where traditional fossil fuel burning would result in air pollution. At the moment, fossil fuels or surplus renewable energy generation are often used to make hydrogen for the energy supply. FCVs have an energy conversion efficiency of 40% to 60%, which is 2 to 3 times that of a hydrogen internal combustion engine (ICE), whereas traditional vehicles only convert 10% to 15% of the energy contained in gasoline to traction.[23] Despite the fact that converting fossil fuels into hydrogen and then back to electricity potentially results in an energy loss, hydrogen has less weight and is simpler to

transport and recharge than batteries, which must be proportionately larger to accommodate the needed capacity [24]. Given a 700 bar hydrogen storage capacity on board, a single FCV refueling could typically support 400–500 km of driving.[22] Additionally, while travelling over 150 miles, an additional weight for the battery is unavoidable for an electric vehicle, but an FCV powered by hydrogen can prevent this. Since brown coal, a low-quality fossil fuel, can also be used to make hydrogen, increasing the amount of hydrogen imported from politically stable coal-rich nations would increase energy security.

These two characteristics lead to the belief that developing and using hydrogen technology is crucial for sustainable development. A "hydrogen economy," which is typically referred to as having the benefits of increasing energy security, improving energy efficiency, and reducing the negative effects on the environment. Recognizing this issue, the world's major nations began to develop, adopt, and test hydrogen technology in the 1990s, resulting in a hydrogen boom. Nowadays, many significant nations have already released the roadmap for the hydrogen economy in order to direct research priorities and judiciously distribute social and financial resources depending on their individual circumstances.[25] Some of them, in particular, Japan, Korea, the EU, and the United States, are research and development leaders, whereas China and India lag behind due to massive local markets.

1.5. Energy Sector Challenges

In the 20th century, the world's energy consumption rose quickly due to the rapid economic expansion in both developed and developing nations, and it is predicted that this trend would continue in the 21st century. More than half of the primary energy demand is met by fossil fuels like coal, oil, and gas, which creates two major issues: an energy shortfall, and emissions from combustion. One common solution to the above issues is to encourage the production of electricity from renewable sources to replace the usage of fossil fuels. According to the International Energy Agency (IEA), by 2040, the share of renewable energy in primary energy consumption will be close to 20%. On the other hand, it is anticipated that from 2020 to 2040, the overall amount of fossil energy would remain steady. It highlights a specific problem in reducing energy consumption in the delivery of power and heat, as well as in the transportation and manufacturing sectors. On the supply side, the approach is to encourage additional alternative low-carbon energy resources while enhancing energy

conversion efficiency. The purpose of hydrogen-based fuel cell technology is only to support such substitutes for the use of energy in buildings and transportation. As was previously indicated, hydrogen may be transported by pipeline and is simple to refill when travelling large distances. Additionally, a number of advanced power generating technologies, including biomass, solar, wind, and solar photovoltaic energy, have been widely used recently and will continue to be prominent in the future. Due to significant reductions in production costs and a suitable Feed-in-Tariff system, wind power and solar PV now account for the majority of renewables-based electric power generation in major regions and nations. While balancing real-time power supply and consumption, unstable wind power and solar radiation also cause issues for the electrical system. In particular, under bright sunlight (if a large fraction of wind and solar PV is used in power generation), the reverse power flow may occur. When wind and solar power generation are extremely unstable, temporary energy storage is the standard for regulating the energy supply. Since hydrogen is appropriate for large capacity energy storage and is easy to transport and use everywhere, the importance of hydrogen energy is emphasized. The introduction of the hydrogen economy, as well as the completion of a CO_2-free supply chain from multiple sources, has been shown to be achievable after years of technological advancement and systemic integration for the hydrogen economy. It is expected that the hydrogen economy will play a significant role in improving the efficiency and use of low-carbon resources in power generation, in order to adapt to and mitigate the problem of climate change, due to the superior performance of hydrogen technology in the convenience of production, transmission, conversion, and environmental friendliness. The global market share of the hydrogen economy would increase as “deep decarbonization” advanced in major economies.

1.6. Water splitting

The production of gases by electric discharge during the water-splitting process has a long history. The electrostatic machine was used for the first time by scientists Jan Rudolph Deiman and Adriaan Paets van Troostwijk in 1789 in Haarlem, The Netherlands, to produce an electric discharge between two gold electrodes. To release the electric potential created between the two gold electrodes, they utilized a Leyden jar filled with water. A new type of gas was discovered to have generated at both electrodes when the opposite charge was applied on gold electrodes. Later, the gas evolved was identified as hydrogen and oxygen,

and gradually a potential application was realized. William Nicholson and Anthony Carlisle were the first to employ Alessandro Volta's voltaic column for water electrolysis in 1800.[26,27] Water splitting has been seen as a long-term remedy for energy issues for about 200 years. Water electrolysis was continuously improved until 1869, making it a low-cost and clever innovation for producing hydrogen in the scientific community. The Gramme machine for producing hydrogen was created at the same time by Zénobe Gramme in 1869. Later, Dmitry Lachinov created a process for producing hydrogen and oxygen at an industrial scale in 1888. Until 1930, a large number of electrolyzers and power plants of around 100 MW were created, which not only generated hydrogen but also became a completely carbon-neutral source of energy.[28] However, this method is somewhat limited by the abundant supply and ease of access to hydrocarbon and other energy sources like hydroelectricity from the ammonia fertilizer sector. Water electrolysis' importance was reaffirmed during the energy crisis of the 1970s, when special coverage was developed to address the issue of sustainable supply. By breaking down water into hydrogen and oxygen, it appears to be the simplest method for producing hydrogen and to supply sustainable energy. Therefore, by making improvements to the water electrolysis process, hydrogen may eventually be replaced as the main fuel source.[29] The process of electrolyzing water results in the development of hydrogen and oxygen gases as well as a byproduct with no carbon emissions. Three crucial methods for environmentally friendly H_2 synthesis include electrochemical water splitting, photo-electrochemical water splitting, and photocatalytic water splitting. There are many developing processes for producing hydrogen in the present, such as high-temperature steam electrolysis, in which water from steam is converted into gases when exposed to high heat, solar thermo-chemical water splitting (artificial photosynthesis), and biological hydrogen production, among others. These advanced processes primarily aim to produce hydrogen through various concepts. These terms are called for the sources used in the biasing process, which improves reaction kinetics by lowering activation energy.[30,31]

1.7. Fundamentals of water splitting

The building blocks of water molecules are molecules of hydrogen and oxygen. Any method of water breakdown results in the production of hydrogen and oxygen. Since hydrogen and oxygen are known to be gases at room temperature and to have extremely high gravimetric energy densities, mixing them with adequate means produces a significant amount of energy

and water as a byproduct. The energy component of such a chemical reaction is so enormous that it could result in an explosion. However, the response is not cynically realistic and does not result in such adversity. If we consider this idea in reverse, which would imply that producing hydrogen and oxygen from water by using excess energy may greatly alleviate our energy crisis. The process of splitting water essentially simulates the generation of hydrogen and oxygen at various electrolyzer electrodes. While not cost-competitive compared to other fuel energy systems, water splitting investigates the carbon-neutral method of hydrogen synthesis using renewable and environmentally benign energy sources. In fact, it provides a realistic and optimal method for producing hydrogen and oxygen. The method demonstrates that a reaction takes place at the electrode's surface, where the oxygen gas is evolved at the while the hydrogen gas gets evolved at the cathode surface. However, splitting the water is not a simple procedure; it requires energy to start the decomposition process. In a device known as an electrolyzer, an electrical charge transfer reaction leads to electrocatalytic water splitting. Thus, at the electrode-electrolyte contact, the electric supply initiates the water decomposition, which then transforms into chemical energy. Energy input for the electrolysis of water may come from thermal, electrical, or solar sources. These catalytic processes are referred to as photocatalytic water splitting, electrocatalytic water splitting, or photoelectrochemical water splitting, among others.[32,33] Due to the poor conductivity of pure water due to lack of ionic constituents a little amount of electrolytes, such as salt or acid is being added to increase the conductivity of water. The salt conducts electricity through electrically separated charged particles that, when given more electrical energy through electrodes made of metal or another conductive substance, gets collected on the electrode surface with the opposite charge. The following describes the overall reaction that occurs when water splits [34]:

$$2OH^- \rightarrow H_2O + \frac{1}{2}O_2 + \ +2e^- \qquad \text{At Anode} \qquad 1.1$$

$$2H_2O + 2e^- \rightarrow 2OH^- + H_2 \qquad \text{At Cathode} \qquad 1.2$$

$$2H_2O \rightarrow 2H_2 + O_2 \qquad \text{Overall reaction} \qquad 1.3$$

Between the two electrodes, there is an open circuit voltage that is known as the equilibrium potential due to the presence of reversibility and the lack of an external supply.

$$E^{\circ} = E_a^{\circ} - E_c^{\circ} \qquad \text{Overall electrode potential} \qquad 1.4$$

The half-cell electrode potentials are E_a° and E_c° for anode and cathode, respectively. The following relationship describes how the energy is transformed into the standard cell voltage:

$$\Delta G^{\circ} = nFE^{\circ} \qquad \text{Gibbs free energy} \qquad 1.5$$

Where 'F' is the Faraday constant, 'n' is number of electrons and $'E^{\circ}'$ is the standard cell voltage. The Gibbs free energy is G° = 237 kJ mol^{-1}, while the total enthalpy for splitting water is H° = 286 kJ mol^{-1}. The total voltage needed in this process for overall water splitting is 1.23 V, which is known as reversible voltage, according to equation (1.5), which includes Gibbs free energy and the enthalpy. The process potential ranges near to 1.23 V, which is practically believed to be the range at which the most efficient water splitting has happened. Two half-cell reactions shown in equations (1.1) and (1.2) are termed as oxygen evolution reaction (OER) and hydrogen evolution reaction (HER), respectively. These half-cell reactions typically involve oxidation and reduction, and they can be combined into a single term of equilibrium potential as shown below:

$$E_{eq} = E^{\circ} + {}^{RT}/_{nF}\, ln\, {}^{a_{\circ}}/_{a_r} \qquad \text{Nernst equation} \qquad 1.6$$

where E° is the standard electrode potential, E_{eq} is the equilibrium potential, R is gas constant, T is absolute temperature, n is number of elctrons, F is Faraday constant and ${}^{a_{\circ}}/_{a_r}$ activity ratio that corresponds to the species in the chemical reaction. Using Nernst equation; oxidation and reduction half-cell reaction can be written as follows:

$$E_{eq} = -0.591 \times pH + 1.23 \qquad \text{OER} \qquad 1.7$$

$$E_{eq} = -0.591 \times pH \qquad \text{HER} \qquad 1.8$$

As can be seen from the equation 1.7 and 1.8 that both OER and HER are *p*H dependent and if the calculation is based on hydronium ions in a reversible hydrogen electrode, the same scale can be made pH-independent. At any pH scale, the potential values for HER and OER will be 0 and 1.23 V relative to a reversible hydrogen electrode. These supporting ions slightly affect the activity, but the thermodynamics of water splitting essentially remain the same. The total potential needed to split water is 1.23 V, also known as the reversible electrode potential, and the energy required for the Gibbs free energy change and reaction enthalpy are 237 kJ mol^{-1} and 286 kJ mol^{-1}, respectively. The water-splitting reaction is

thermodynamically impossible at ambient temperature since this value of free energy is not attainable, and it can only take place if sufficient energy is provided. Overpotential is the additional energy used to break through the activation barrier and jump-start the intrinsically slow electrochemical reaction. Higher potential is also necessary due to the charge migration, bubble formation, and potential loss caused by the voltage supply. Although the impact of such a barrier cannot be completely disregarded, the overall kinetic barriers can be reduced by giving the reaction an intermediate state that requires less activation energy and can be finished with less energy. These redox-active species improve the overall efficiency of the process by acting as intermediates. This could only happen if the electrode material favors one side of the reaction and improves overall reaction kinetics by reducing the energy requirements. This intermediate reaction platform enables the interconversion of electrical and chemical potential energy at lower potential and at a rapid rate [35].

1.8. Hydrogen Evolution Reaction

In the current situation, particularly in the field of electrochemical reaction, hydrogen evolution is one of the most significant and difficult tasks that calls for effective strategy and exploration. The adsorption and desorption of hydrogen atoms at the electrode surface greatly influences the overall chemical kinetics. Adsorption and desorption require monoatomic intermediates that moderate hydrogen bonding at the electrode surface. The hydrogen generation by water splitting is quite fascinating due to the establishment and breaking of bond energies by careful electrocatalyst selection.[36]

1.9. Basics of electrochemical hydrogen evolution reaction

The cathodic and anodic half-cell reactions indicated in equations 1.2 and 1.3 have pH terms that cancel each other out, making the overall water splitting a pH-independent process. However, in the half cell process, *p*H becomes a critical component that impacts hydrogen generation efficiency. The potential necessary for each half cell reaction is directly impacted by the *pH* dependence in the system.[37] The Nernst equation, which was previously discussed in the preceding parts, shows that the potential falls by 59 mV for every unit higher in the electrolyte's *p*H. This equation demonstrates that the potential required for hydrogen evolution differs from the thermal equilibrium potential in acidic, alkaline, and neutral environments. However, a number of other factors that play a role in the larger overpotential

value are taken into account during hydrogen evolution. The real-time needed overpotential is modified by the presence of various environmental conditions, and the equation is expressed as follows:

$$E = E_{RHE} + iR + \eta \quad (1.9)$$

The performance of electrodes and the electrolyzer are primarily determined by the overpotential, which also provides a direct indication of an electrolyzer's effectiveness. By increasing the electrocatalyst's catalytic activity with the right choice of electrolyte, the value can be reduced. For example, platinum as an electrocatalyst can lower the overpotential voltage close to zero. Based on reaction rate and hydrogen production, the effectiveness of an electrolyzer or the activity of an electrocatalyst can be assessed. The generation of hydrogen is mostly influenced by the pH of the solution, which can be either acidic or alkaline. The entire hydrogen generation kinetics happens through different mechanisms, and the entire mechanism has been classified with various steps based on this. In the two-electron transfer process that the HER undergoes, the role of the electron and the step involved mostly determine the reaction rate, and the reaction rate is essentially characterized by the ΔG_H. The value of G_H reveals how the electrode and the hydrogen are bound together. A weak link between hydrogen and the electrode surface causes the adsorption (Volmer) step, which limits the overall reaction rate. In contrast, a strong bond between hydrogen and the electrode surface causes desorption (Heyrovsky/Tafel) step, which controls the reaction kinetics. The hydrogen evolution process is primarily composed of two steps. The first is the Volmer step, which is a universal step that is followed by either the Heyrovsky step or the Tafel reaction. After reduction, the proton in the electrolyte attaches to the electrode surface and forms a metal hydride bond. The hydrogen evolution is then carried out by an electrochemical step (Heyrovsky Step) or by a chemical reaction between adsorbed hydrogen atoms on the electrode's surface (Tafel Step). According to the reaction medium and Volmer step, the HER reaction converts proton or water into hydrogen, depending on the mechanism used to generate hydrogen (Volmer-Heyrovsky or Volmer-Tafel). The HER exhibits the following fundamental reactions:

In acidic conditions;

$$E + H_3O^+ + e^- \rightarrow E - H_{ads} + H_2O \quad \text{Volmer Step} \quad (1.10)$$

$$E - H_{ads} + H_3O^+ + e^- \rightarrow H_2 + H_2O \quad \text{Heyrovsky Step} \quad (1.11)$$

$$2E - H_{ads} \rightarrow 2E + H_2 \qquad \text{Tafel Step} \qquad 1.12$$

In alkaline conditions;

$$E + H_2O + e^- \rightarrow E - H_{ads} + OH^- \qquad \text{Volmer Step} \qquad 1.13$$

$$E - H_{ads} + H_2O + e^- \rightarrow H_2 + E + OH^- \qquad \text{Heyrovsky Step} \qquad 1.14$$

$$2E - H_{ads} \rightarrow 2E + H_2 \qquad \text{Tafel Step} \qquad 1.15$$

Here, E represents the electrocatalyst and $E - H_{ads}$ represents hydrogen atom adsorbed on the catalyst active sites. Tafel slope value acquired from the polarisation curve can be used to generalize the HER mechanism at active sites in an electrochemical process. The electrochemical reaction for hydrogen evolution is explained by the Tafel slope value, which measures how well the electrocatalysts are performing. However, additional parameters like applied potential and mass transfer in the porous structure could have an impact on the value of the Tafel slope. The well-known Butler-Volmer equation can be used to represent the HER electrochemical kinetics as shown below:

$$i = i_\circ \exp\left[\left(\alpha_a n\eta F/_{RT}\right) - \left(\alpha_c n\eta F/_{RT}\right)\right] \qquad 1.16$$

Here α_a and α_c are the transfer coefficients, n is the number of electrons involved in the reaction, η is the overpotential required to carry out the reaction, F is Faraday constant, R and T is gas constant and temperature respectively. In the expression, the first portion contributes to the anodic current and the second part represents the cathodic current, which are two separate types of currents that flow through an electrolyzer. If the applied potential of one term is higher than other term, so other term can be neglected in that case and the equation can be written as follows:

$$i_a = i_\circ \exp\left(\alpha_a n\eta F/_{RT}\right) \qquad 1.17$$

$$i_c = i_\circ \exp\left(\alpha_c n\eta F/_{RT}\right) \qquad 1.18$$

$$i_a = i_\circ \exp\left(\eta/_b\right) \qquad 1.19$$

$$i_c = i_\circ \exp\left(\eta/_b\right) \qquad 1.20$$

Here, $b = RT/_{\alpha_a n\eta F}$ and $b = RT/_{\alpha_c n\eta F}$ for anode and cathode respectively.

The equations could be written in terms of current density as

$$j_a = j^{\circ}\exp\left(\eta/_b\right) \quad 1.21$$

$$j_c = j^{\circ}\exp\left(\eta/_b\right) \quad 1.22$$

The overpotential for half-cell reaction can be calculated by rearranging the terms and simplifying the equation.

$$\eta = 2.303\left(RT/_{\alpha_a nF}\right)logj^{\circ} + 2.303\left(RT/_{\alpha_c nF}\right)logj^{\circ} \quad 1.23$$

This equation can be comparable to Tafel equation ($\eta = a + b\log j$), where $a = 2.303\left(RT/_{anF}\right)logj^{\circ}$ and $b = 2.303\left(RT/_{anF}\right)$ corresponds to constant quantity at particular condition and Tafel slope respectively. The significant insight in the mechanism or rate-determining step is practically reflected by the Tafel slope value. Generally, it is expressed as $mVdec^{-1}$ and should have small value as possible. It is simple to predict from the Tafel equation that overpotential can be reduced by using electrocatalysts that improve the kinetics of the electrode reaction by either offering higher values of the exchange current density (j°), without changing the reaction mechanism, or by reducing the slope of the equation, which means if there is an increase in charge transfer coefficient. The efficiency of HER process during electrolysis of water can be increased by using highly efficient electrocatalyst with low tafel slope and high exchange current density.[15,38]

1.10. Oxygen evolution reaction

Due to four proton-electron linked interactions, the oxygen evolution reaction (OER) is a complex process with a complicated mechanism. The pH of the medium has a significant impact on OER reaction. The reactions take place as follows:

In acidic conditions;

$$4H^+ + 4e^- \rightarrow 2H_2 \quad \text{At cathode} \quad 1.24$$

$$2H_3O \rightarrow O_2 + 4H^+ + 4e^- \quad \text{At anode} \quad 1.25$$

In alkaline conditions;

$$4H_2O + 4e^- \rightarrow H_2 + 4OH^- \quad \text{At cathode} \quad 1.26$$

$$4OH^- \rightarrow 2H_2O + O_2 + 4e^- \quad \text{At anode} \quad 1.27$$

1.11. Electrocatalyst

Since the beginning of civilization, when early humankind started producing alcohol through fermentation, the significance of catalysis has been understood. There has been no effort made to explain these phenomena throughout this period of catalysis; only private interpretation has been acknowledged. J. J. Berzelius, a Swedish scientist, observed an improvement in reaction kinetics when a specific substance was present for the Stockholm Academy in 1835. He identified the driving mechanisms behind this improvement, dubbed them catalytic forces, and developed the term "catalysis" for these substances. This is possibly the first time that catalysis has been recognized as widespread natural phenomena. According to a later statement by Wilhelm Ostwald, "there is probably no chemical reaction that cannot be affected catalytically." He explained how the catalyst works and how its presence speeds up reaction kinetics without changing the chemical process' thermodynamic equilibrium.[39] At that time, it was evident that including a catalyst in a chemical process could result in commercial or financial rewards in addition to resolving a time-consuming issue. Such material not only lowers the reaction's activation energy but also makes it more rapid and effective. Recent years have seen an increase in the perception of these materials as having strategic value and their use in a broad range of research fields. The growing concern over climate change and environmental safety has promoted the use of carbon-neutral energy storage and transportation methods. To steer the reaction process towards a particular product and prevent side reactions, a good catalyst should be extremely active toward the reactant species and highly selective toward one of the products. As a catalyst's performance is greatly influenced by changes in pH, temperature, and an intensely oxidizing or reductive environment, selectivity and stability are its primary concerns. In the field of electrocatalysis, these catalysts are classified as homogeneous and heterogeneous catalysts.[40,41] The homogeneous catalyst primarily exists as the same phase as the reactant in the chemical reaction, which makes the process of separating each substance labor- and energy-intensive. However, the heterogeneous catalyst is particularly well suited for the catalytic process since it is a diverse phase in comparison to the reactant. In electrochemical processes, the electrocatalyst and electrocatalysis concentrate on the material's catalytic activity at the electrode surface. The first pioneers to introduce the idea of electrolysis and research the electrode reaction were Bowden and Rideal in 1928. However, other scientists, including

Bockris and Khan, claim that T. Grubb coined the word "electrocatalysis" in 1936 while working on fuel cells. The method depends on the transfer of electrons for oxidation or reduction at the electrode material's surface or within the electrode itself. By introducing an intermediate state into the reaction process, it changes the reaction kinetics and reduces the activation energy. In order to create a connection with reaction kinetics, the electrocatalysis method examines the material properties in a solution. The material that serves as an electrocatalyst in a chemical reaction has a different activation energy, which in turn affects how differently reactants, products, and intermediates are bonded. Because the electrode material has altered thermodynamics, the surface catalytic reaction takes place via distinct reaction routes. Therefore, any alteration or modification in the material or its property alters the kinetic process. This explains how effectively a material can improve an electrochemical reaction while the conditions are the same. The strength of the chemical bonding between the electrode and the electrolyte affects the reaction kinetics. An appropriate choice of electrocatalyst could greatly improve the efficiency of an electrolyzer. Continued efforts are made to find such materials to enhance electrode stability as well as to lower investment and operating costs. The catalyst's practical applicability required a compromise between various analyses of the data. The importance of a catalyst is always determined by its relative performance in terms of electrocatalytic activity, thermodynamic stability, durability, and its primary manufacturing cost issue. The synthesis process and/or the composite material's built-in synergy both have the potential to increase the material's activity. Then, replacing the noble material with a non-noble one may also succeed in achieving the goal. Non-noble materials have a low tendency for electrocatalytic reactions. One of the processes that only depend on the electrode characteristics is water splitting.[42]

1.12. Parameters for evaluating efficient electrochemical HER catalysts

1.12.1. Overpotential

Under normal circumstances, the HER standard electrode potential is zero. An electrocatalyst's corresponding overpotential is the absolute value of the difference between thermodynamic potential and actual potential for HER. A high performance electrocatalyst attains the same current density at a lower overpotential. The polarisation curves can be obtained by plotting current density vs. overpotential. The overpotential can be primarily separated into activation overpotential and concentration overpotential depending on where

the polarization on the electrode originated. By implementing the appropriate electrocatalysts, the latter can be significantly reduced. The main cause of concentration overpotential is the differential in ion concentrations between the electrode surface and the bulk solution, which is brought on by ions' sluggish diffusion rates. However, because of the diffusion layer, stirring can only partially lower the concentration overpotential, which could interfere with the electrode reaction. Resistance overpotential, also referred to as junction overpotential, is a significant additional overpotential that develops at the measuring system's surfaces and interfaces. The measured overpotential of the electrode will be higher than its actual value due to additional voltage drop brought on by resistance across surfaces and interfaces. IR compensation is a helpful technique to achieve correct electrocatalyst overpotential and eliminate this form of overpotential. The resistance overpotential in a three electrode measurement system is mostly caused by resistance between the working electrode's surface and the Luggin capillary's tip. The R in the IR compensation is this resistance. The value of R can be directly measured by many electrochemical workstations. At high frequencies, the value can also be read out directly from the leftmost Nyquist curve–X-axis intersection. The following connections represent how the IR compensation is expressed.

$$E_{correction} = I \times R \tag{1.28}$$

$$E_{corrected} = E_{uncorrected} - E_{correction} = E_{uncorrected} - I \times R \tag{1.29}$$

Where E represents potential and I represents the system's current. Because the current is so little at that point, the correction has a slight impact on the beginning overpotential, according to the equation. The $E_{correction}$ and the shift of the polarization curves will, however, both grow in size as the current increases.

1.12.2. Tafel slope and exchange current density

The Tafel slope can be calculated by fitting the linear areas of Tafel plots to the Tafel equation by replotting the polarisation curves (overpotential vs. log|current density|). The Tafel slope's value is most frequently obtained in this way. The Tafel slope's lower value indicates that a smaller overpotential was required to increase the same current density, which suggests that the charge transfer kinetics were faster. Hu's group suggests a different approach to acquiring the Tafel slope, which has recently gained the support of researchers

[43]. They calculated the slope of the log Rct vs. overpotential linear fitting plots using the impedance data to derive the Tafel slopes. The electrochemical impedance spectroscopy (EIS) data of the electrocatalyzed HER reaction can be fitted with an equivalent electric circuit, where Rct is the equivalent circuit's charge transfer resistance. This approach can only reflect the charge transfer kinetics of the electrode reaction in the tafel slopes that are obtained. Tafel slopes obtained from polarisation curves, however, may also take into account the contribution from catalyst resistance, which may be brought on by a high catalyst loading or a low electrical conductivity of the electrocatalysts.

The exchange current density is determined at the point where the extrapolated linear portion of Tafel plots meets the X-axis. The anodic current density and cathodic current density are equal at equilibrium. The exchange current density is equal to this value of current density in both directions. The intrinsic characteristic of the electrode reaction, which is entirely dependant on the catalyst, electrolyte, and temperature, is exchange current density. It illustrates the capacity for electron transfer and the complexity of an electrode reaction. Exchange current density is the internal cause of overpotential. Larger exchange current density electrode reactions require smaller overpotential to carry out the reaction.

1.12.3. Moderate binding energy

A good HER electrocatalyst should usually have a free energy of hydrogen adsorption that is neither too strong nor too weak.[44] The poor adsorption makes it harder for the proton and electrocatalyst to combine. In contrast, it will be challenging to remove the highly adsorbed H_{ads} from the catalytic surface. The catalyst becomes poisoned as a result of the active sites on the catalytic surface being continuously occupied. Given that the normal hydrogen electrode potential is zero, a good HER electrocatalyst should have hydrogen bonding Gibbs free energies that are almost equal to zero. DFT simulations are always used to determine the Gibbs free energy of hydrogen adsorption. The Sabatier Volcano can be found by plotting the exchange current density versus the Gibbs free energy of hydrogen adsorption. Better HER activity is displayed by the electrocatalyst with a plot towards the volcano's crest.[45]

1.12.4. Stability

Another crucial method for assessing HER electrocatalysts is stability. Galvanostatic or potentiostatic electrolysis and cyclic voltammetry (CV) are the two methods used to measure stability. Potential cycles that include the onset HER potential are repeated in CV. The stability of the electrocatalyst is improved by a decrease in the overpotential for a given current density after hundreds of CV cycles. According to voltammograms, a steady electrocatalyst's polarisation curve should vary minimally compared to the initial one over CV cycles. Galvanostatic (or potentiostatic) electrolysis is the time-dependent variation of an electrocatalyst's potential (or current density) at constant current density (or overpotential). Due to the fact that 10 mA/cm^2 is the most widely used standard in HER electrocatalysis and solar fuel production, this type of electrolysis frequently employs this number. The duration can range from several to dozens of hours, with higher duration implying more stability.

1.12.5. Faradic efficiency

The Faradic efficiency in HER refers to how effectively electrons supplied by an external circuit are transferred to power the HER. When heat or byproducts of the electrode reaction are produced, faradic losses could happen. Both the theoretical and actual amounts of H2 generation are required to calculate Faradic efficiency. Galvanostatic or potentiostatic electrolysis can be used to compute theoretical hydrogen generation through integration. Gas chromatography (GC) or a water–gas displacement method can both be used to measure the actual hydrogen generation. The Faradic efficiency is the ratio of theoreticalxdd to actual hydrogen production.

1.13. Non-noble metal electrocatalyst

A sustainable method for producing hydrogen is water electrolysis, which uses power from renewable energy sources. However, the water electrolysis reactions for hydrogen evolution (HER) and oxygen evolution (OER) are both kinetically slow, which results in low efficiency in the related electrolysis apparatus. Additionally, the commercialization of contemporary electrocatalysts that can efficiently catalyse both HER and OER is greatly constrained by the need for expensive and scarce noble metals like platinum. Therefore, there has been a greater emphasis on creating high-performance and affordable non-noble metal electrocatalysts to replace noble ones. Transition metal-based catalysts such as chalcogenides, nitrides,

phosphides and selenides with varied structures show good catalytic activity for HER. Among these catalysts, phosphorous based materials like Transition metal phosphate and phosphides have been widely used as electrocatalysts. The activity of these materials has further been increased by the introduction of oxygen which enhanced the intrinsic conductivity and also activated the catalytic sites as a result of elongation of M-P bond. As a result of their enhanced catalytic activity and special structure, extensive attention has been drawn towards phosphorous based materials.

1.13.1. Phosphorus based materials

Phosphorus is the one of the most abundant element on earth. The concentration of phosphorus is about one gram per kilogram in the earth crust. Phosphorus is very reactive element, so it is never found alone and generally found in minerals as phosphate. In the present thesis, we have chosen transition metal phosphate and phosphide for our work.

1.13.1.1. Transition metal phosphates

Transition metal phosphates (TMPi) are important among the noble metal-free materials because they are inexpensive, abundant on earth, environmentally friendly and have high stability. TMPi have been used for energy storage and efficient energy conversion applications due to their distinctive chemical/physical and tunable properties.[46–48] TMPi are likely to form layered structure with open framework. The diverse oxidation state of metals in TMPi improves their redox behavior and allows them to have strong protonic conductivity.[49] The cobalt phosphate shows superior electrocatalytic activity towards OER has been reported in neutral medium.[50] It has been demonstrated that the phosphate group not only functions as a proton receptor to maintain the catalyst systems long-term stability but also causes distortion in structure of cobalt, making it easier for water molecules to bind and as a result enhances the OER activity. In addition to the OER, transition metal phosphates may also have some activity towards the oxygen reduction reaction (ORR).[51] However, metal phosphates' weak electrical conductivity and tendency to aggregate limit their ability to boost catalytic performance further. In order to improve conductivity and catalyze the OER/ORR or OER/HER with metal phosphates, heteroatom-doped carbon materials can be used as a solution to this problem. For instance, a composite of TMPi and graphene oxide (GO) aerogels has been used as the air cathode of a Zn-air battery, showing great potential for

practical rechargeable batteries.[52] Additionally, because to their open architectures with big channels and cavities that enable high charge/ion conductivity and charge storage capacity, transition metal phosphates are a very interesting candidate for supercapacitors.[53] Hence, it has been reported the superior electrochemical capacitance behavior of transition metal phosphates with a high specific capacitances and robust stability after numerous cycles.[54–56] The architectures and morphologies of transition metal phosphates have a significant impact on their electrochemical properties. It has been possible to create a variety of porous transition metal phosphates with various porous morphologies and structures. Transition metal phosphates have a variety of structures, including 1D nanowire, 2D nanosheet and 3D nanostructures.[57–59] Each structure has distinct characteristics and related applications.

1.13.1.2. Transition metal phosphides

The "transition metal–phosphorus-based materials" (TMPs) have drawn a lot of attention because of their enormous potential for use in electrochemical energy conversion and storage technologies, including water electrolysis, fuel cells, and metal–air batteries. TMPs were initially discovered in the 18th century. Unexpectedly, it took almost 200 years until any noteworthy TMPs uses were discovered. Up to the 1960s, TMPs were gradually used in metallurgy, hydrodesulfurization (HDS), hydrodenitrogenation (HDN), hydroprocessing (HPC), insecticides, photocatalytic degradation, lithium ion batteries, and other fields. The development and use of TMPs were severely hampered for many years in the early days since the majority of metal phosphide syntheses were undertaken under high temperatures and/or pressures using combustible elemental phosphorus (P) as the phosphorus source. Early research studies revealed that amorphous transition metal–phosphorus "alloy" film electrodes produced by room temperature electrodeposition had strong activity towards HER. And at the time, people believed that rather than the catalysts themselves, the elevated HER activity of these electrodes resulted from the metals altered electronic structure as a result of hydrogen adsorption during electrochemical preparation. Based on calculations using density functional theory (DFT), Liu and Rodriguez discovered in 2005 that the Ni_2P (001) behaved substantially like the [NiFe] hydrogenase, foreseeing that Ni_2P would be a highly active HER catalyst.[60] After discovering that the Ni_2P (001) in 2005, Liu and Rodriguez raised the first experimental report on nanoscale TMPs for high performance electrochemical hydrogen

evolution in 2013. This study used an anion-exchange method to synthesize nanoporous FeP nanosheets, which demonstrated excellent electrocatalytic activity toward HER with low overpotential and a small Tafel slope.[61] Schaak, Lewis, and colleagues reported Ni_2P hollow nanoparticles as an active HER electrocatalyst nearly at the same time.[62] The analogous mechanism between HDS and HER, in which both underwent the process of reversibly attaching and dissociating a hydrogen atom, served as the inspiration for this work.[60] As a result, Ni_2P with a nearly 100% HDS conversion was chosen as the research model. Additionally, the as-prepared Ni_2P nanoparticles had a high density of exposed (001) facets, which verified the validity of the earlier theoretical prediction. The activity and stability of TMPs toward HER were significantly increased in 2014 when Sun and colleagues produced various TMP nanostructure arrays directly on three-dimensional (3D) substrates through gas-solid interaction without surfactants. These ground-breaking studies mark the beginning of TMPs' glory as very effective HER electrocatalysts.[63–65]

1.14. Characterization techniques

1.14.1. Power x-ray Diffraction

X-ray powder diffraction (XRD) is an analytical, non-destructive technique used for the determination of properties like phase identification, geometry, lattice constant, orientation and defects of a crystalline material and can provide information on unit cell dimensions. Thus, this is a useful technique in the identification of unknown materials that does not require elaborate sample preparation. Powder samples are finely grounded, homogenized, and then directly loaded on the XRD sample holder.[66,67] PXRD was discovered by Max von Laue in 1912. X-ray diffraction is based on constructive interference of monochromatic X-rays and a crystalline sample. The principle of X-ray diffraction is based on Bragg's Law explained by Lawrence Bragg. These X-rays are generated by a cathode ray tube with a particular wavelength (usually ranging from 0.7 to 2θ), filtered to produce monochromatic radiation, and directed toward the sample which then gets scattered from the lattice planes of the crystal separated by the inter-planar distance 'd' as shown in *Figure 1.1*. These scattered waves when undergo constructive interference, conditions for Bragg's Law are satisfied ($n\lambda = 2dsin\theta$) which states that when the X-ray is incident onto a crystal surface, its angle of incidence, θ, will reflect with the same angle of scattering, θ. And, when the path

difference, d is equal to a whole number, n, of wavelength, λ, constructive interference will occur. These diffracted X-rays are then detected, processed and counted by a detector which is the output to a device such as a computer monitor. The diffraction pattern of each material is unique due to unique d-spacing so the conversion of the diffraction peaks to d-spacing allows identification of the material. A slight shift in the Bragg's peak indicates a change in the lattice constant of the structure. Usually, this is achieved by comparing of d-spacing of material with standard reference patterns. Due to the random orientation of the powdered material, all possible diffraction directions of the lattice are achieved by scanning the sample through a range of 2Θ angles. The technique is also used for particle size determination by using the Scherer formula (Equation 1.26) by relating particle size to the peak width.

$$D = \frac{K\lambda}{BCos\theta_B} \qquad 1.30$$

Where λ is the wavelength of the X-rays, *D* is the size of the crystal, *B* is the full-width half maxima of the diffraction peak, θ_B is the diffraction angle, and K is the Scherrer's constant of the order of unity for the usual crystal.[68,69] Experimental diffraction pattern can also be refined further with calculated profiles and background using rietveld refinement (3). In this thesis, powder XRD measurements were performed to study the crystal structures of the materials. Here, Bruker Eco D8 setup using Cu Kα radiation (λ = 0.154056 nm) was used to obtain XRD patterns. The schematic representation of bragg equation and typical image of PXRD instrument is shown in *Figure 1.1* and *Figure 1.2* respectively

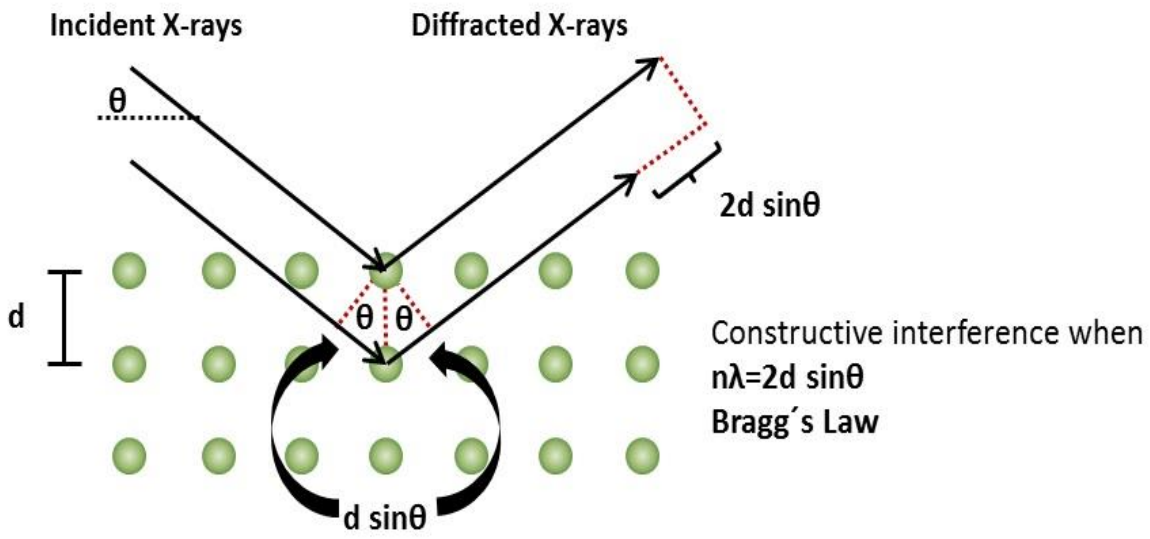

Figure 1.1. Schematic representation of the Bragg equation

1.14.1.1. High-temperature X-ray diffraction

The information on crystallinity and phase change of materials in the necessary temperature range has been obtained using X-ray diffraction studies at varying high temperatures. The same Bragg's diffraction technique is used in in-situ high-temperature X-ray diffraction. Additional distinctive information is provided by in-situ high-temperature X-ray diffraction, such as temperature-dependent phase transitions, thermal changes in structural parameters, and variations in the actual structural parameters with temperature.

Figure 1.2. A typical view of PXRD instrument

1.14.2. Fourier Transform Infrared Spectroscopy

FTIR is the most common form of infrared spectroscopy which is basically concerned with the vibration of molecules. The vibrational energy in the bond will change after selectively absorption of specific wavelength radiations by the covalent bonds of the molecules. The type of vibration (stretching or bending) induced by the infrared radiation relies on the atoms

in the bond as each functional group has its own distinct vibrational energy [70]. Different bonds and functional groups absorb different frequencies; therefore, transmittance (or absorption) pattern is different for different molecules, which can be used to recognize a molecule through the combination of all of the functional groups. Hence, this analytical technique is used for the identification of organic, polymeric and in some cases inorganic materials, multilayer film characterization, particle analysis and differentiating among the molecules. FTIR basically works on the principle that when infrared (IR) radiation passes through a sample, some of the radiation is absorbed and some are passed through (transmitted). The resulting spectrum of molecular absorption and transmission creates a molecular fingerprint of the sample. Infrared absorption spectroscopy commonly used 4000 ~ 400 cm^{-1} region because of the presence of the absorption radiation of most organic compounds and inorganic ions in this region.[71]

Major parts of FTIR include: 1) IR source such as mid-IR ceramic source, a near-IR halogen lamp, or a far-IR mercury lamp, 2) an interferometer, heart of FTIR, which consists of a beam splitter (to split the light from a source into two paths with half the light going to a stationary mirror and the other half going to a moving mirror), a stationary mirror, a moving mirror, and a timing laser and 3) a detector. Common beam splitter materials are KBr (375 – 12,000 cm^{-1}), Quartz (4,000 – 25,000 cm^{-1}), and Mylar (30 – 680 cm^{-1}). The beams from both the mirrors are recombined back at the beam splitter and directed toward the sample. Constructive and destructive interference are formed due to the difference in the path of the mirrors over the course of time. The position of the moving mirror is determined with the help of a laser (e.g. HeNe lasers) of known wavelength. Detectors such as Si-photodiodes for visible and near-IR, convert photons into measurable electric signals to be sent to the computer. The "output" of the interferometer is not the spectroscopy spectrum we use, but the signal versus mirror position (and, thus, time) graph known as an "interferogram." The Fourier transform, to decode the individual frequencies, is used to convert the interferogram into the infrared spectroscopy spectrum graph within the computer, in order to make an identification.[70,72]

1.14.3. Thermogravimetric analysis

During a thermogravimetric analysis (TGA), the sample's weight or mass can be determined as a function of time or temperature. Typically, the sample is heated during the TGA analysis at a specific heating rate or at a fixed temperature (isothermal measurement). The choice of temperature depends on the kind of information about the sample that is needed. The environment used for the TGA will be crucial. The weight, mass, or percentage of mass measured in the TGA curve in relation to time or temperature. The first derivative of the TGA curve involving temperature or time has been utilized for TGA analysis, which represents the mass change rate and is known as the differential thermogravimetric (DTA) curve. The TGA/DTA can provide the following kinds of information.

- Learn about volatile elements, gas desorption and adsorption, moisture evaporation, crystallization water loss, and other volatile compounds
- The metal's oxidation temperature in any atmosphere
- Manufacturing synthetic temperatures for novel materials
- Prediction of magnetic property change (Curie transition)

In TGA curve only weight loss is observed but DTA curves shows endothermic and exothermic peaks from which we can determine melting and crystallization or transition. The endothermic peak and exothermic peaks are observed due to adsorption of energy and release of energy respectively during thermal treatment. A typical view of TGA/DTA instrument has been shown in *Figure 1.3.*

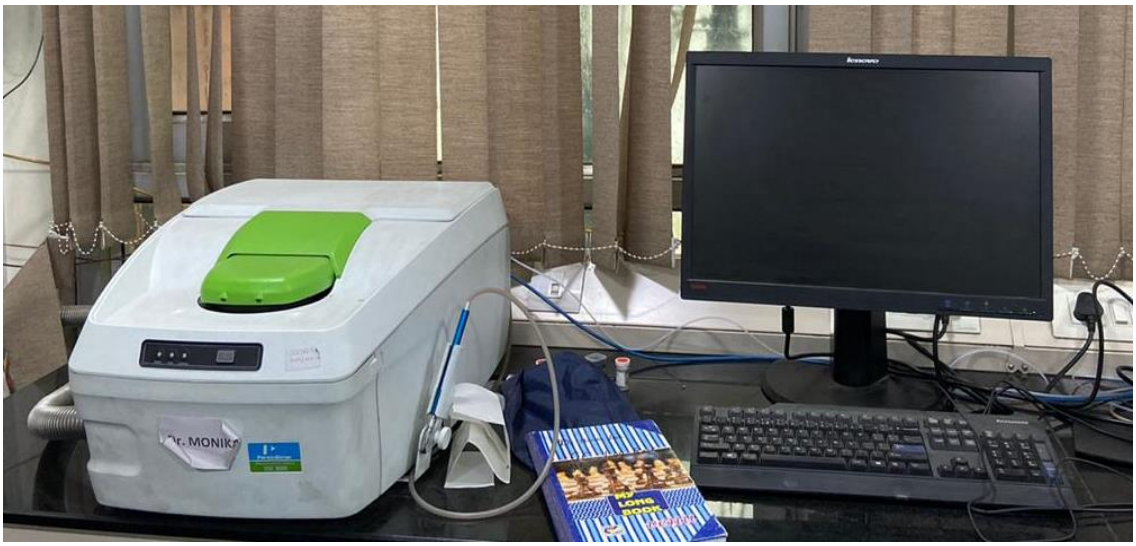

Figure 1.3. TGA system for studying the thermal stability of compounds

1.14.4. Transmission Electron Microscopy

A microscopy technique called Transmission electron microscopy (TEM) may provide images with extremely high resolution down to a level of few Angstroms (0.19 nm). Through the interaction of electrons passing through a sample, it can image thin (100s nms) materials. The study of nano-scale morphological and chemical properties of materials down to almost atomic levels is made possible by the detection of a variety of consequent secondary signals.[73]

Electrons are emitted from an electron source at the top of the microscope and move through a vacuum in the column of the instrument. The electrons are directed into the target specimen after being focused into a very tiny beam using electromagnetic lenses. After travelling through the specimen, the electrons strike a detector. Traditional bright field imaging relies on the sample's compositional density and crystal orientation to determine how incident electrons scatter and disappear from the beam. The amount of unscattered electrons creates a "shadow image" of the specimen, with various densities of the specimen's components represented in varying degrees of darkness. The typical image of TEM instrument is shown in *Figure 1.4.*

1.14.4.1. Electron diffraction

It is also possible to use electron diffraction (ED) to examine the crystal structure of samples having regular atomic structure (crystalline material). By mapping the back focal plane to the imaging device, discrete regions of electron localization caused by positive interference in the back focal plane may then be seen. The specimen's crystal structure can then be determined using the diffraction patterns.

1.14.4.2. Energy-Dispersive Spectrometer

An energy-dispersive spectrometer (EDS) inside the TEM can also detect X-ray emission caused by the primary electron beam interacting with the material. The spectra produced can be used to identify the constituent elements since the resulting X-ray energy are indicative of the atomic structure of the element from which they came.

Figure 1.4. A typical image of TEM

1.14.5. Scanning electron microscope

A scanning electron microscope (SEM) is a type of electron microscope that gives the image of a sample by using high energy electron beam. It is considered as a non- destructive technique as there is no volume loss of the sample.[74] The main components of SEM include source of electron, high vacuum column to travel electrons, electron detector, sample chamber and a computer for the display of images.[75–77] The high energy electron beam by interacting with the sample produces various signals including secondary electrons, backscattered electrons, and characteristic X-rays. These signals are then collected by detectors to form images displayed on computer screen.[78] In typical SEM, normally low energy secondary and high energy backscattered electrons are detected by Everhart-Thornley detector and solid state detector respectively. Secondary electron is always emitted from the surface of the sample when incoming electron beam undergoes inelastic scattering with the atoms of the sample. As a result, a part of the energy is transferred to another electron which is emitted from the surface after gaining sufficient energy and is termed as a secondary electron.[79,80] It gives information about the surface's topography, morphology, composition of material and gives 2-dimesnsional image. While the backscattered electrons are produced due to elastic interactions between the beam and sample and are useful in giving contrasts in composition in multiphase samples (i.e. for rapid phase discrimination). They have the same energy as that of the primary electron beam. Characteristic X-ray photon or an Auger electron is emitted and comes to its ground state, when primary electron beam collides with the atom and eject core electron. These electrons are useful for elemental and quantitative compositional analysis of a sample. The typical image of SEM instrument is shown in *Figure 1.5*.

Figure 1.5. A typical image of SEM

1.14.6. Atomic force microscopy

Binnig, Quate, and Gerber originally showed atomic force microscopy (AFM), a high-resolution non-optical imaging technology, in 1985.[81] Since then, it has grown to be an effective measurement instrument for surface examination. AFM enables precise and non-destructive measurements of a sample surface's topographical, electrical, magnetic, chemical, optical, mechanical, etc. properties with extremely high resolution[82] in air, liquids, or ultrahigh vacuum.

The fundamental working principle of a conventional AFM system with optical feedback is the raster-pattern scanning of an AFM probe with a sharp AFM tip over a sample surface.[83] Near the free end of a flexible AFM cantilever, the silicon or silicon nitride AFM tip is integrated. The lateral and vertical positions of the AFM probe with respect to the surface are managed by a piezoelectric ceramic scanner. The deflection of the AFM cantilever varies when the AFM tip passes over objects of various heights. A laser beam is reflected from the rear of the AFM cantilever and directed into a position-sensitive photodetector in order to measure this deflection. The AFM cantilever deflection and, consequently, the contact force,

are nearly constant thanks to a feedback loop that regulates the scanner's vertical extension. A three-dimensional topographic image of the surface is created by combining the coordinates that the AFM tip tracks throughout the scan. The schematic process and typical image of AFM instrument is shown in *Figure 1.6* and *Figure 1.*7.

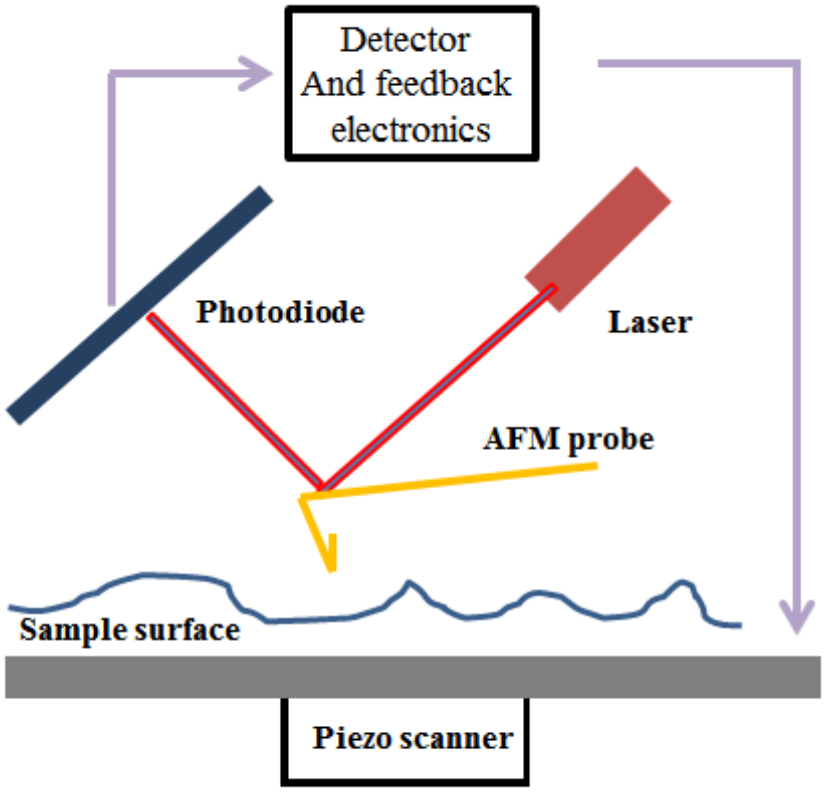

Figure 1.6. Schematic of AFM

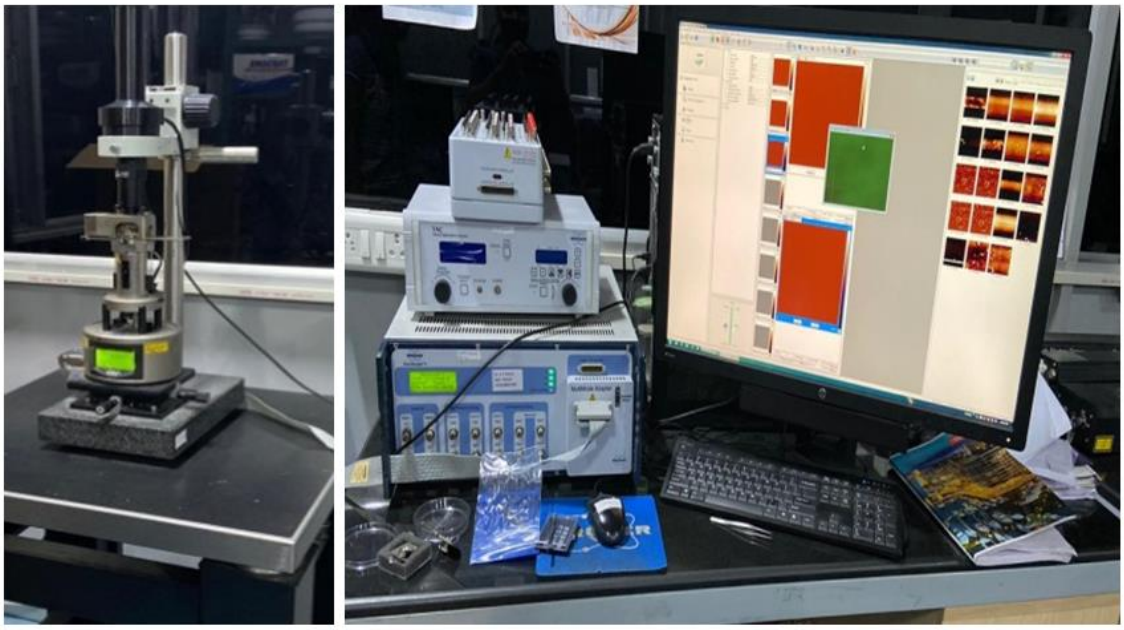

Figure 1.7. The typical AFM setup.

1.14.7. Surface area analysis

Brunauer Emmett Teller theory was coined by Stephen Brunauer, Paul Hugh Emmett and Edward Teller in 1938. The theory explains the extension of monolayer adsorption in Langmuir theory to multilayer adsorption. BET instrument is the prime technique to analyse surface area, pore radius, pore volume, surface irregularities and structure of pores of powders, granules and solids. During sorption analysis the surface of solid sample makes contact with gas phase and a part of it gets adsorbed on external part of surface. When the relative pressure $\left(\frac{P}{P_0}\right)$ is increased more molecules get adsorbed onto surface and gradually the monolayer is formed and soon the multilayer and the multilayer is recorded from adsorbed volume. Liquid nitrogen is most used gaseous adsorbate employed, because of the nitrogen usage the standard BET instrument is operated at 77 K that is the boiling point of N_2. Other adsorbates like argon, CO_2 and water are employed to probe the specific surface area of materials. Generally, the multilayer adsorption of the gas molecules is analyzed which are chemically inactive to the surface of the material. As per BET theory the number of molecules adsorbed or desorbed with the change in temperature and pressure in comparison to $\left(\frac{P}{P_0}\right)$ can be known and rest of the work is done by the software. The BET

software programmed with an appropriate mathematical model to calculate the surface area. The BET equation explains the interactions between solid sample materials and gases by the following equation.

$$\frac{1}{X[(P_0/P)-1]} = \frac{1}{X_M C} + \frac{C-1}{X_M C}\left(\frac{P}{P_0}\right) \qquad 1.31$$

Where, X_M is number of molecules/atoms of a gas that form a monolayer and the BET equation (Equation 1.17) describes the relationship between the number of gas molecules adsorbed (X) at a given relative pressure $\left(\frac{P}{P_0}\right)$, where C is a second parameter related to the heat of adsorption. The BET equation strictly describes a linear plot of $\frac{1}{X[(P_0/P)-1]}$ vs $\frac{P}{P_0}$ in case of most of solid wherein liquid nitrogen is utilized as an adsorbate. The typical image of BET surface analyzer instrument is shown in *Figure 1.8*.

Figure 1.8. A typical view of BET surface area analyser

1.14.8. Raman spectroscopy

Raman spectroscopy is an analytical technique that uses scattered light to measure a sample's vibrational energy modes. It is named after Indian scientist C. V. Raman, who first observed Raman scattering in 1928 along with his research partner K. S. Krishnan.[84] Raman spectroscopy is the non-destructive characterization technique to get the structural information of materials. Organic, inorganic and biological samples with solid, liquid or gas can be characterized through this technique. The scattering process and typical image of Raman instrument is shown in *Figure 1.9* and *Figure 1.10*.

When light is scattered by molecule, some of the energy of photon transferred to the molecule and the leave the molecule in higher energy state due to induce polarization by oscillating electromagnetic field of a photon. It is a very short-time process. The photon is re-emitted almost instantly as scattered light. When there is an elastic collision, there is no change in the energy of the molecule and the incent photon energy is equal to the scattered photon. This is called Rayleigh scattering. In an inelastic collision there is some change in the energy of incident and scattered light due to transfer of energy between molecule and scattered photon. If the molecule gains and loses energy to the scattered photon it leads to stokes and anti-stokes Raman scattering.

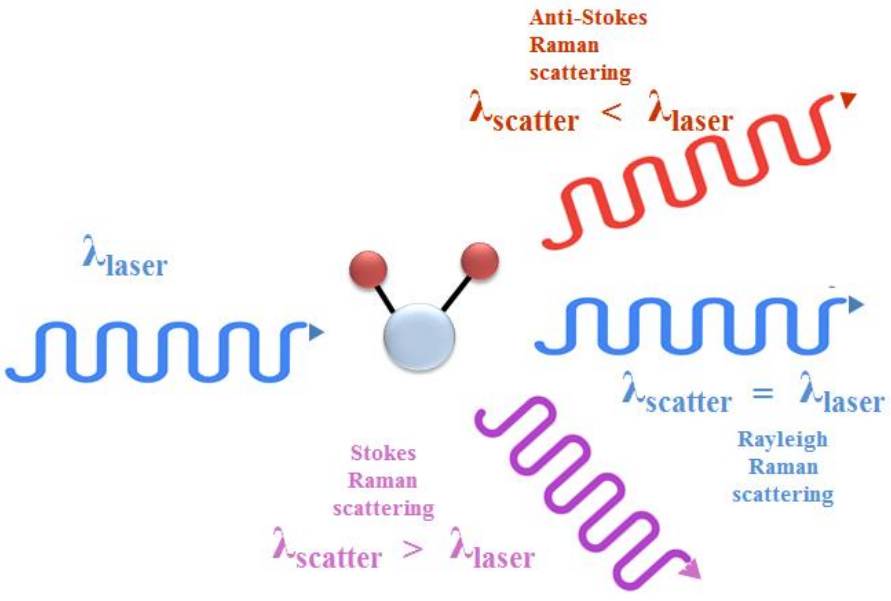

Figure 1.9. Scattering processes when light interacts with a molecule

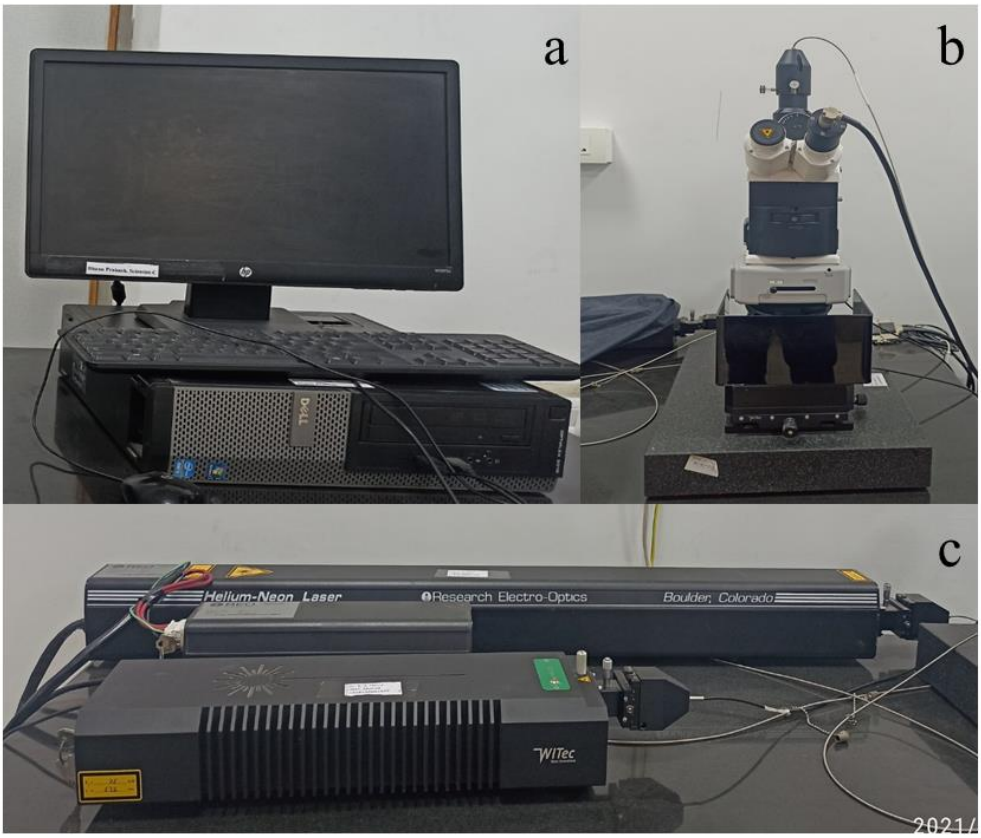

Figure 1.10. (a) Computer of Raman setup (b) Spectrometer.(c) Laser source

1.14.9. Inductively coupled plasma mass spectrometry

Everything around us is constructed from various elemental mixtures. Inductively coupled plasma mass spectrometry (ICP-MS) is a method that is frequently used by analysts to determine what elements something is made of. ICP-MS is an elemental analysis technique, which means it measures elements rather than molecules and compounds like LC/MS and GC/MS. ICP-MS transforms the sample into ions using an argon (Ar) plasma, which are then examined using a mass spectrometer. Similar to inductively coupled plasma optical emission spectroscopy (ICP-OES), ICP-MS examines the elements (ions) directly as compared to ICP-OES, which uses an optical spectrometer to measure the light emitted from elements as they travel through the plasma. Both methods quickly analyses a variety of elements in a sample, however ICP-MS has far lower detection limits than ICP-OES, making it a superior option for analyzing trace elements.[85] The typical image of ICP-MS instrument is shown in *Figure 1.11*.

ICP-MS is frequently used to examine samples that are liquids (like water) or that can dissolve or produce a liquid after being acid digested. ICP-MS, however, is incredibly adaptable and may quickly measure organic solvents, find incredibly minute (nano) particles, or be coupled to accessories that enable direct investigation of solid materials or gases.

The main components of ICP-MS are:

- System for introducing samples that produces a thin aerosol mist from liquid samples
- Ionization of the elements in the sample aerosol using plasma (ICP)
- Interface to extract the ions into the vacuum system
- Ion lens to focus the ions and distinguish them from background signals
- Collision/reaction cell (CRC) to resolve the analyte ions from interfering ions
- Mass spectrometer (MS) to filter the analyte ions by mass
- The electron multiplier detector
- Data processing

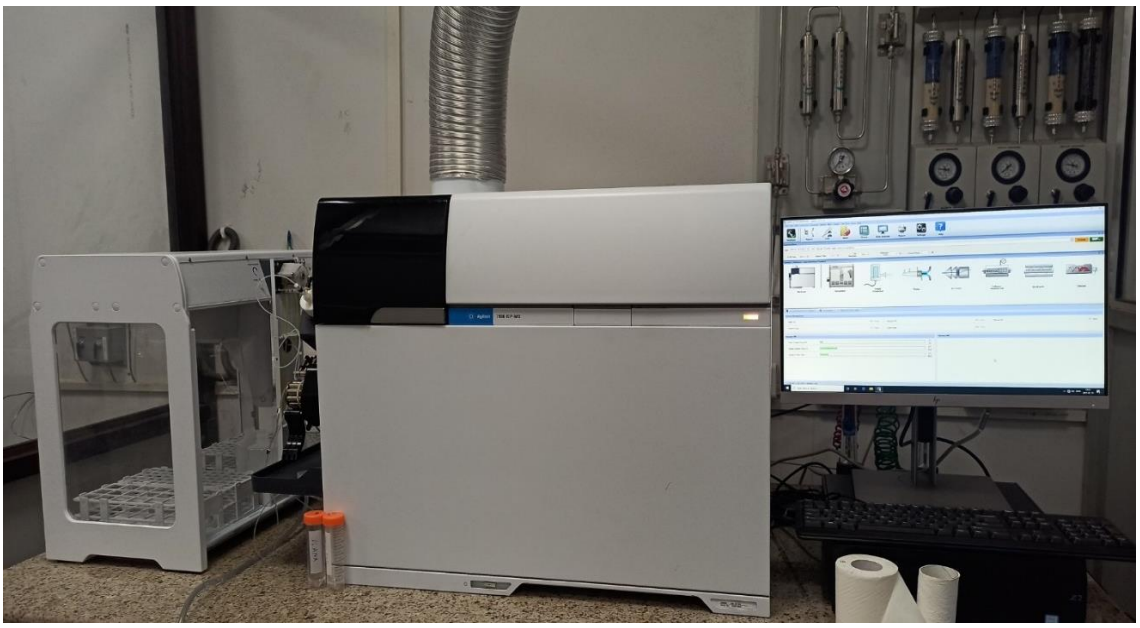

Figure 1.11. Typical view of inductively coupled plasma- mass spectroscopy

1.14.10. X-ray photoelectron spectroscopy

X-ray photoelectron spectroscopy (XPS) is a quantitative technique and is useful for measuring valence state, surface composition and detects all elements within the material except hydrogen and helium because they don't emit inner core electron. It involves surface analysis of a sample

by irradiating a sample with monochromatic soft x-rays and analyzing the energy of detected electron. The kinetic energy analysis of electrons emitted from the surface yields information about auger peaks, satellite peaks, multiple splitting which is used to identify elemental states of atoms. XPS is equipped with Mg Kα (1253.6 eV) or Al Kα (1486.6 eV). X-ray photoelectron spectroscopy (XPS) is an ultra-high vacuum technique and is capable to give information to a depth of 10 nm. When photon or X-ray interact with atoms in the surface region causing electrons to be ejected from the core-levels of the elements from the sample by photoelectric effect. The kinetic energy (E_k) of the emitted photoelectrons is measured by the following equation:

$$E_B = hv - E_k - \varphi \qquad 1.32$$

Where, E_B = Binding energy of the electron, hv = photon energy, E_k= kinetic energy of the photoelectrons, φ = spectrometer work function

These are the following application of XPS

- XPS identify a wide atomic number range (Z=3 to Z=92) atomic compositions
- It provides information about structure and oxidation state of compounds. Thus also known as ESCA (electron spectroscopy for chemical composition)
- Identification of active sites
- Determination of surface contamination on semiconductors
- Study of oxide layer on metal
- Analysis of dust on the sample

The data of XPS plotted as a function of the number of electron (counts). As binding energy is the key characteristics of elements and therefore it can be used to reveal the chemical and elemental composition of the material. The obtained core peaks is corresponds to the electronic configuration of respective orbitals such as 1s, 2s, 2p, 3s etc. The count of detected electron in each of the characteristic peak reveals the quantity of the elements within the volume irradiated. The typical image of XPS instrument is shown in *Figure 1.12*.

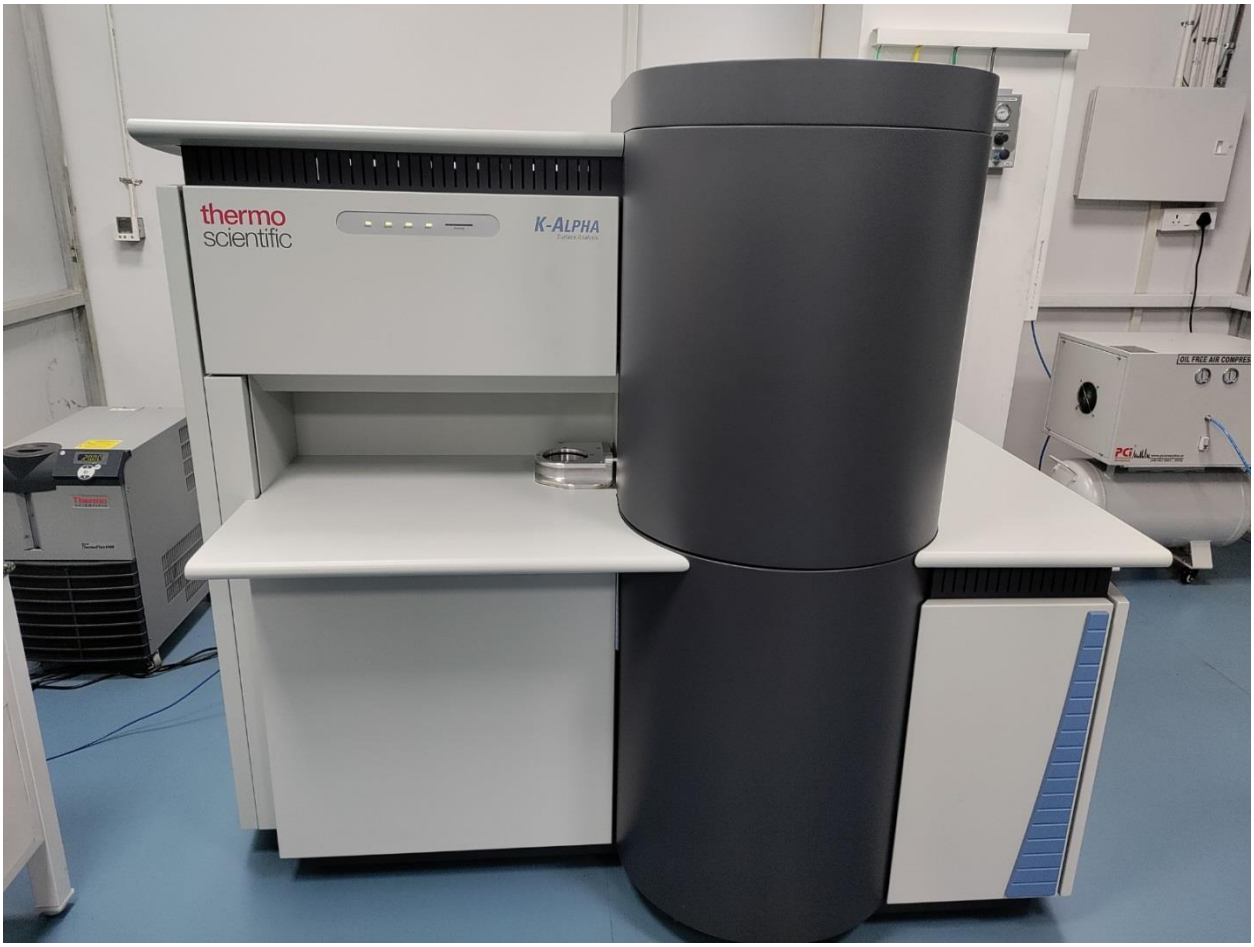

Figure 1.12. A typical view of XPS instrument

1.14.11. Electrochemical methods

The electrochemical activity of the electrocatalysts for the HER is evaluated using different electrochemical parameters as discussed above. To evaluate these parameters few electrochemical techniques are required such as Cyclic Voltammetry, Linear sweep voltammetry, electrochemical impedance spectroscopy and chronoamperometry. These studies have been carried out in three electrode configuration system. The results were further evaluated to obtain different electrochemical parameters which gives information about the electrocatalytic activity of a material.

1.14.11.1. Electrode configuration

The electrochemical measurements were carried out in three electrode system. There are three electrodes in the setup: a working electrode, a reference electrode, and a counter

electrode. The graphite rod and Ag/AgCl (3M KCl) are used as a counter and reference electrode respectively. For working electrode bare graphite sheet is used.as shown in *Figure 1.13*.

1.14.11.2. Cyclic and Linear Sweep Voltammetry

The most widely used techniques to study the redox reactions of organic and inorganic species are cyclic voltammetry (CV) and linear sweep voltammetry (LSV) because of their ability to provide information on the steps involved in the electrochemical processes. During the LSV the potential is swept at a constant rate in a given potential window. If the same scan reverts in the given potential window, the recorded data between current and potential represents the cyclic voltammogram and the technique is termed as cyclic voltammetry. Both these techniques are used to evaluate the activity of catalysts during the HER study by comparing the data recorded in terms of voltammograms. The tafel slope can be calculated from the linear sweep voltammogram obtained at a slow scan rate which helps in describing the mechanism with which the reaction proceeds. The surface properties of the catalyst such as oxide formation, morphology of the catalyst and mass loading can be evaluated using CV through electrode-electrolyte interface, the number of cycles along with scan rate and range of potential respectively. On cycling if there is change in the oxidation state of the material or the structure, it results in a change in the activity of the material.

1.14.11.3. Electrochemical Impedance Spectroscopy

The primary concern of any reaction is to obtain results with the minimum errors and in electrochemical studies the potential required to generate hydrogen depends in the conductivity or the resistance of the material. There are number of resistive factors which affect the process of hydrogen evolution and ohmic loss during such measurements need to be corrected. The factors responsible for such loses could be resistance resulting from the circuit connection or from the electrolyte. Electrochemical Impedance Spectroscopy (EIS) is a powerful, rapid, non-destructive and easily automized tool to investigate the electrode reactions and properties of a variety of materials. Using this technique, the impedance in a circuit is measured in ohms. The main advantage of EIS over other techniques is that it is a steady-state technique and utilize small signal values. A wide range of frequency can be used from less than 1 mHz to more than 1 MHz to probe signal relaxations. In this technique a

sinusoidal voltage is applied and current response is measured. The resulting faradic impedance spectrum is known as the Nyquist plot which contains information about elements like ohmic resistance of electrolyte solution, double layer capacitance, electron transfer resistance and Warburg diffusional impedance. This equivalent electric circuit provides valuable information about the properties and interface of the electrode-electrolyte and represents fingerprint of the sample.

1.14.11.4. Chronoamperometry

The two main parameters that is essential for electrocatalysts selection for their application in the HER is their electrocatalytic effects and their long-term stability. The highly efficient HER catalysts have high electrocatalytic activity, low resistance towards charge transfer and high stability. The stability of the catalyst tells about its robustness and is usually evaluated using the chronoamperometry technique. It involves the variation of current response with respect to time at a fixed potential. In this technique the electrode is stepped from a potential where no electrode reaction occurs to the one corresponding to the mass-transport-limited current and the resulting current-time transient is measured. The change in the current appears in response to rises or falls in the diffuse layers of analyte at the surface of working electrode.

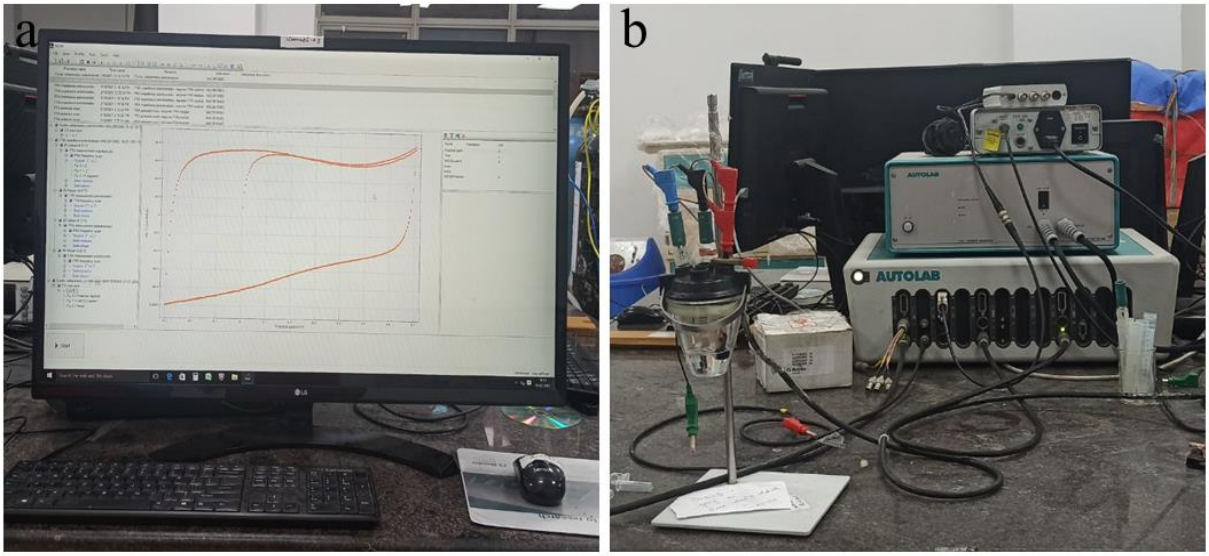

Figure 1.13. (a) Computer setup for electrochemical setup. (b) Conventional 3 electrode setup to Autolab

1.15. Aim of the thesis

Phosphorous based materials have undergone extensive exploration and study in recent years that demonstrate amazing corrosion resistance and remarkable catalytic activity. The transition metals' high level of physical and chemical stability, low cost, and potential for high catalytic activity make them a priority in the field of hydrogen generation technology. The potential for using phosphorous based materials as a catalyst in electrochemical reactions, particularly for the production of hydrogen, has previously been extensively investigated. We know that transition metal phosphates are well known for their OER properties but their investigation towards HER are very less known. Generally most of the phosphates are dissolved in the acidic media but recently. Liu et al synthesized acid stabilized nickel cyclotetraphosphate nanosheets (120 nm) and used as an electrocatalyst towards HER.[86] Cuncai et al also synthesized cobalt cyclotetraphosphate and utilized as an electrocatalyst.[87] These studies show that cycloteraphosphate are stable in acidic media and can be utilized as an electrocatalyst towards HER. So in present thesis we choose metal cyclotetraphopshate for our work and synthesize using chemically assisted solid state route at lower temperature and normal conditions. The synthesized compounds are further investigated towards HER in an acidic media. Further to increase the catalytic activity of metal cyclotetraphosphate we also synthesize bimetallic cyclotetraphosphate and their composite with rGO to increase its electrical conductivity.

On the other hand, we also synthesized and investigated transition metal phosphides towards HER. TMPs are well known for their electrocatalytic properties towards electrochemical energy conversion and energy storage applications. In TMPs due to presence of high electronegative P atoms, they act as a proton acceptor sites and metal atoms with positive charge act as hydride acceptor sites respectively. Together both sites promote HER activity. In here, we choose chemically assisted solid state route for the synthesis of TMP. The as prepared TMP were used for HER in acidic and alkaline medium.

1.16. References

1. Green Technology and Design for the Environment - Samir Billatos - Google Books. Available at: https://books.google.co.in/books?hl=en&lr=&id=uBtHUCWqYngC&oi=fnd&pg=PA3

&dq=Billatos,+S.,+Green+technology+and+design+for+the+environment.+CRC+Press:+1997.&ots=_gjNE-r7j-&sig=0QEl6ejowm-z6r15yY6Cs4aG8Zo&redir_esc=y#v=onepage&q&f=false. (Accessed: 23rd June 2022)

2. Sustainable Fossil Fuels: The Unusual Suspect in the Quest for Clean and Mark Jaccar Google Books Available at: https://books.google.co.in/books?hl=en&lr=&id=3L957CerahoC&oi=fnd&pg=PR10&dq=Jaccard,+M.,+Sustainable+fossil+fuels:+the+unusual+suspect+in+the+quest+for+clean+and+enduring+energy.+Cambridge+University+Press:+2006.&ots=2oNYwwNCzv&sig=lgVHgW-wd7PD92tMZUx-eeSgPvo&redir_esc=y#v=onepage&q=Jaccard%2C M.%2C Sustainable fossil fuels%3A the unusual suspect in the quest for clean and enduring energy. Cambridge University Press%3A 2006.&f=false. (Accessed: 23rd June 2022)
3. Sustainable Solutions: Developing Products and Services for the Future - Google Books. Available at: https://books.google.co.in/books?hl=en&lr=&id=VKo0DwAAQBAJ&oi=fnd&pg=PT26&dq=Sustainable+solutions:+developing+products+and+services+for+the+future.+Routledge:+2017.&ots=zSd9ZdrtCJ&sig=975vTvhmu0yNmsSAauAWkdlbWjE&redir_esc=y#v=onepage&q=Sustainable solutions%3A developing products and services for the future. Routledge%3A 2017.&f=false. (Accessed: 23rd June 2022)
4. Wuebbles, D. J. & Jain, A. K. Concerns about climate change and the role of fossil fuel use. *Fuel Process. Technol.* **71**, 99–119 (2001).
5. Popp, A. *et al.* Additional CO_2 emissions from land use change — Forest conservation as a precondition for sustainable production of second generation bioenergy. *Ecol. Econ.* **74**, 64–70 (2012).
6. reviews, A. O.-R. and sustainable energy & 2008, undefined. Energy, environment and sustainable development. *Elsevier*
7. Economy & Ecology: Towards Sustainable Development - Google Books. Available at:https://books.google.co.in/books?hl=en&lr=&id=wu7qCAAAQBAJ&oi=fnd&pg=PA89&dq=Kneese,+A.,+RU+Ayres.+Economy+%26+Ecology:+Towards+Sustainable+Development+2013,+1,+89.&ots=2EWz7bp5Pm&sig=JOzBNR0eYlMin7ANEQhcc

YN74LI&redir_esc=y#v=onepage&q=Kneese%2C A.%2C RU Ayres. Economy %26 Ecology%3A Towards Sustainable Development 2013%2C 1%2C 89.&f=false. (Accessed: 23rd June 2022)

8. Chen, Z., Policy, G. C.-E. & 2011, undefined. An overview of energy consumption of the globalized world economy. *Elsevier*
9. Moriarty, P., warming, D. H.-M. global & 2019, undefined. Global renewable energy resources and use in 2050. *Elsevier*
10. Kadoshin, S., Nishiyama, T., Energy, T. I.-A. & 2000, undefined. The trend in current and near future energy consumption from a statistical perspective. *Elsevier*
11. Climate and Society: Transforming the Future - Robin Leichenko, Karen O'Brien Google Books. Available at: https://books.google.co.in/books?hl=en&lr=&id=BJ-dDwAAQBAJ&oi=fnd&pg=PT7&dq=Leichenko,+R.%3B+O%27Brien,+K.,+Climate+and+society:+transforming+the+future.+John+Wiley+%26+Sons:+2019.&ots=8StQy6imqt&sig=XG8SPX4r9EilP12dKu_qK0uLTCo&redir_esc=y#v=onepage&q=Leichenko%2C R.%3B O'Brien%2C K.%2C Climate and society%3A transforming the future. John Wiley %26 Sons%3A 2019.&f=false. (Accessed: 25th June 2022)
12. Pachauri, R., Allen, M., Barros, V. & Broome, J. *Climate change 2014: synthesis report. Contribution of Working Groups I, II and III to the fifth assessment report of the Intergovernmental Panel on Climate*. (2014).
13. Owusu, P., Engineering, S. A.S.C. & 2016, undefined. A review of renewable energy sources, sustainability issues and climate change mitigation. *Taylor Fr.* **3**, (2016).
14. Purohit, I., Sundaray, S. & Motiwala, S. Familiarization with energy storage technologies and their relevance for renewable energy (RE) based power generation. *Green Energy Technol.* 273–326 (2018). doi:10.1007/978-981-10-7326-7_14
15. Bockris, J. O. & Potter, E. C. The Mechanism of the Cathodic Hydrogen Evolution Reaction. *J. Electrochem. Soc.* **99**, 169 (1952).
16. Zohuri, B. The Chemical Element Hydrogen. *Hydrog. Energy* 1–35 (2019). doi:10.1007/978-3-319-93461-7_1
17. Zohuri, B. Hydrogen energy: Challenges and solutions for a cleaner future. *Hydrog. Energy Challenges Solut. a Clean. Futur.* 1–283 (2018). doi:10.1007/978-3-319-93461-7

18. Sources, A. D.-E., Economics, P. B., Planning, undefined, and, undefined & 2017, undefined. Future hydrogen economy and policy. *Taylor Fr.* **12**, 172–181 (2017).
19. Abdalla, A. M. *et al.* Hydrogen production, storage, transportation and key challenges with applications: A review. *Energy Convers. Manag.* **165**, 602–627 (2018).
20. Hydrogen: Its Technology and Implication: Production Technology - Volume I - R I Cox - Google Books.
21. Chen, Y. H., Chen, C. Y. & Lee, S. C. Technology forecasting and patent strategy of hydrogen energy and fuel cell technologies. *Int. J. Hydrogen Energy* **36**, 6957–6969 (2011).
22. Ball, M. & Weeda, M. The hydrogen economy – Vision or reality? *Int. J. Hydrogen Energy* **40**, 7903–7919 (2015).
23. Emadi, A.; K. R.I. T on & 2005, undefined. Topological overview of hybrid electric and fuel cell vehicular power system architectures and configurations. *ieeexplore.ieee.org*
24. IEEE, U. B.-P. of the & 2006, undefined. Does a hydrogen economy make sense? *ieeexplore.ieee.org*
25. McDowall, W. Technology roadmaps for transition management: The case of hydrogen energy. *Technol. Forecast. Soc. Change* **79**, 530–542 (2012).
26. Trasatti, S. Water electrolysis: Who first? *J. Electroanal. Chem.* **476**, 90–91 (1999).
27. Diaz-Morales, O. *et al.* Electrochemical water splitting by gold: evidence for an oxide decomposition mechanism. *pubs.rsc.org* doi:10.1039/C3SC50301A
28. Mostafaeipour, A. *et al.* Evaluating the wind energy potential for hydrogen production: A case study. *Int. J. Hydrogen Energy* **41**, 6200–6210 (2016).
29. Staffell, I. *et al.* The role of hydrogen and fuel cells in the global energy system. *Energy and Environmental Science* **12**, 463–491 (2019).
30. Balthasar, W. Hydrogen production and technology: today, tomorrow and beyond. *Int. J. Hydrogen Energy* **9**, 649–668 (1984).
31. Photoelectrochemical Water Splitting: Materials, Processes and Architectures - Google Books. Available at: https://books.google.co.in/books?hl=en&lr=&id=0nMoDwAAQBAJ&oi=fnd&pg=PP1&dq=Parkinson,+B.%3B+Turner,+J.%3B+Peter,+L.%3B+Lewis,+N.%3B+Sivula,+

K.%3B+Domen,+K.%3B+Bard,+A.+J.%3B+Fiechter,+S.%3B+Collazo,+R.%3B+Hannappel,+T.,+Photoelectrochemical+water+splitting:+materials,+processes+and+architectures.+Royal+Society+of+Chemistry:+2013.&ots=gztMOU_2Zf&sig=N3kJmJSLbUz_9ut2pQJUf197d9c&redir_esc=y#v=onepage&q&f=false. (Accessed: 27th June 2022)

32. Tee, S. Y. *et al.* Recent Progress in Energy-Driven Water Splitting. *Adv. Sci.* **4**, 1600337 (2017).
33. Hilliard, S. Water splitting photoelectrocatalysis: the conception and construction of a photoelectrocatalytic water splitting cell. (2016).
34. Godula-Jopek, A. *Hydrogen production: by electrolysis*. (2015).
35. Lasia, A. Mechanism and kinetics of the hydrogen evolution reaction. *Int. J. Hydrogen Energy* **44**, 19484–19518 (2019).
36. energy, A. L. journal of hydrogen & 2019, undefined. Mechanism and kinetics of the hydrogen evolution reaction. *Elsevier*
37. Giordano, L. *et al.* pH dependence of OER activity of oxides: current and future perspectives. *Elsevier*
38. Bhardwaj, M., Hydrogen, R. B.-I. J. of & 2008, undefined. Uncoupled non-linear equations method for determining kinetic parameters in case of hydrogen evolution reaction following Volmer–Heyrovsky–Tafel mechanism and. *Elsevier*
39. Lindström, B. & Pettersson, L. J. A brief history of catalysis. *CATTECH* **7**, 130–138 (2003).
40. Tandon, P. K., Bahadur Singh, S. & Kumar Tandon, P. Catalysis: A brief review on Nano-Catalyst. *J. Energy Chem.* **2**, 106–115 (2014).
41. Catalysts, J. V.- & 2017, undefined. Heterogeneous catalysis on metal oxides. *mdpi.com*
42. Shi, Y. & Zhang, B. Recent advances in transition metal phosphide nanomaterials: Synthesis and applications in hydrogen evolution reaction. *Chemical Society Reviews* **45**, 1529–1541 (2016).
43. Vrubel, H., Moehl, T., Grätzel, M. & Hu, X. Revealing and accelerating slow electron transport in amorphous molybdenum sulphide particles for hydrogen evolution reaction. *Chem. Commun.* **49**, 8985–8987 (2013).

44. Xiao, P. *et al.* Molybdenum phosphide as an efficient electrocatalyst for the hydrogen evolution reaction. *Energy Environ. Sci.* **7**, 2624–2629 (2014).

45. Wu, R., Zhang, J., Shi, Y., Liu, D. & Zhang, B. Metallic WO_2-Carbon Mesoporous Nanowires as Highly Efficient Electrocatalysts for Hydrogen Evolution Reaction. *J. Am. Chem. Soc.* **137**, 6983–6986 (2015).

46. Whittingham, M., Song, Y., Lutta, S., Chemistry, P. Z. of M. & 2005, undefined. Some transition metal (oxy) phosphates and vanadium oxides for lithium batteries. *pubs.rsc.org*

47. Chen, C. *et al.* Transition-metal phosphate colloidal spheres. *Wiley Online Libr.* **121**, 4910–4913 (2009).

48. Zhao, H., Technology, Z. Y.-C. S. & & 2017, undefined. Transition metal–phosphorus-based materials for electrocatalytic energy conversion reactions. *pubs.rsc.org*

49. Murugavel, R., Choudhury, A., Walawalkar, M. G., Pothiraja, R. & Rao, C. N. R. Metal complexes of organophosphate esters and open-framework metal phosphates: Synthesis, structure, transformations, and applications. *Chem. Rev.* **108**, 3549–3655 (2008).

50. Kanan, M. W. & Nocera, D. G. In situ formation of an oxygen-evolving catalyst in neutral water containing phosphate and Co^{2+}. *Science (80-.).* **321**, 1072–1075 (2008).

51. Sharma, L., Baskar, S. & Barpanda, P. Electrocatalytic Oxygen Reduction Reaction Activity of Sodium Metal Phosphate Based Insertion Cathodes. *ECS Trans.* **85**, 1221–1227 (2018).

52. Ren, J. T., Yuan, G. G., Chen, L., Weng, C. C. & Yuan, Z. Y. Rational Dispersion of Co2P2O7 Fine Particles on N,P-Codoped Reduced Graphene Oxide Aerogels Leading to Enhanced Reversible Oxygen Reduction Ability for Zn-Air Batteries. *ACS Sustain. Chem. Eng.* **6**, 9793–9803 (2018).

53. Patil, D. R. *et al.* Cobalt Cyclotetraphosphate ($Co_2P_4O_{12}$): A New High-Performance Electrode Material for Supercapacitors. *ACS Appl. Energy Mater.* **2**, 2972–2981 (2019).

54. Li, X. *et al.* Metal (M= Co, Ni) phosphate based materials for high-performance supercapacitors. *pubs.rsc.org*

55. Li, X., Elshahawy, A. M., Guan, C. & Wang, J. Metal Phosphides and Phosphates-based Electrodes for Electrochemical Supercapacitors. *Small* **13**, (2017).

56. Wang, G., Zhang, L. & Zhang, J. A review of electrode materials for electrochemical supercapacitors. *Chem. Soc. Rev.* **41**, 797–828 (2012).

57. Li, Q., Chemie, V. Y.-A. & 2007, undefined. Redox Luminescence Switch Based on Energy Transfer in CePO4:Tb^{3+} Nanowires. *Wiley Online Libr.* **119**, 3556–3559 (2007).

58. Chen, C. *et al.* Polypyrrole-Modified $NH_4NiPO_4 \cdot H_2O$ Nanoplate Arrays on Ni Foam for Efficient Electrode in Electrochemical Capacitors. *ACS Sustain. Chem. Eng.* **4**, 5578–5584 (2016).

59. Guo, H. X. & Liu, S. X. A novel 3D organic–inorganic hybrid based on sandwich-type cadmium hetereopolymolybdate: $\{[Cd_4(H_2O)_2(2,2'\text{-bpy})_2]Cd[Mo_6O_{12}(OH)_3(PO_4)_2(HPO_4)_2]_2\}[Mo_2O_4(2,2'\text{-bpy})_2]_2 \cdot 3H_2O$. *Inorg. Chem. Commun.* **7**, 1217–1220 (2004).

60. Liu, P. & Rodriguez, J. A. Catalysts for hydrogen evolution from the [NiFe] hydrogenase to the $Ni_2P(001)$ surface: The importance of ensemble effect. *J. Am. Chem. Soc.* **127**, 14871–14878 (2005).

61. Xu, Y. *et al.* Anion-exchange synthesis of nanoporous FeP nanosheets as electrocatalysts for hydrogen evolution reaction. *pubs.rsc.org*

62. Popczun, E. J. *et al.* Nanostructured nickel phosphide as an electrocatalyst for the hydrogen evolution reaction. *J. Am. Chem. Soc.* **135**, 9267–9270 (2013).

63. Liang, Y., Liu, Q., Asiri, A. M., Sun, X. & Luo, Y. Self-supported FeP nanorod arrays: A cost-effective 3D hydrogen evolution cathode with high catalytic activity. *ACS Catal.* **4**, 4065–4069 (2014).

64. Pu, Z., Liu, Q., Asiri, A. M. & Sun, X. Tungsten phosphide nanorod arrays directly grown on carbon cloth: A highly efficient and stable hydrogen evolution cathode at all pH values. *ACS Appl. Mater. Interfaces* **6**, 21874–21879 (2014).

65. Tian, J., Liu, Q., Asiri, A. M. & Sun, X. Self-supported nanoporous cobalt phosphide nanowire arrays: An efficient 3D hydrogen-evolving cathode over the wide range of pH 0-14. *J. Am. Chem. Soc.* **136**, 7587–7590 (2014).

66. Parker, G. Encyclopedia of materials: science and technology. (2001).

67. Warren, B. *X-ray Diffraction*. (1990).
68. Uvarov, V. & Popov, I. Metrological characterization of X-ray diffraction methods for determination of crystallite size in nano-scale materials. *Mater. Charact.* **58**, 883–891 (2007).
69. Holzwarth, U. & Gibson, N. The Scherrer equation versus the 'Debye-Scherrer equation'. *Nat. Nanotechnol. 2011 69* **6**, 534–534 (2011).
70. What is FTIR Spectroscopy? Available at: https://www.sigmaaldrich.com/IN/en/technical-documents/technical-article/analytical-chemistry/photometry-and-reflectometry/ftir-spectroscopy. (Accessed: 27th June 2022)
71. Introduction to Fourier Transform Infrared Spectrometry. (2001).
72. FTIR Spectroscopy - Theory and Fundamentals | JASCO. Available at: https://jascoinc.com/learning-center/theory/spectroscopy/fundamentals-ftir-spectroscopy/. (Accessed: 27th June 2022)
73. TEM. Available at: https://www.nottingham.ac.uk/isac/facilities/tem.aspx. (Accessed: 27th June 2022)
74. Scanning Electron Microscopy (SEM). Available at: https://serc.carleton.edu/research_education/geochemsheets/techniques/SEM.html. (Accessed: 26th June 2022)
75. Review, K. V.-P.-I.-V. & 2000, undefined. Scanning electron microscopy: an introduction. *Elsevier*
76. Egerton, R. F., Li, P. & Malac, M. Radiation damage in the TEM and SEM. *Micron* **35**, 399–409 (2004).
77. MacDonald, N. C. & Waldrop, J. R. Auger electron spectroscopy in the scanning electron microscope: Auger electron images. *Appl. Phys. Lett.* **19**, 315–318 (1971).
78. Scanning Electron Microscopy - Nanoscience Instruments. Available at: https://www.nanoscience.com/techniques/scanning-electron-microscopy/. (Accessed: 26th June 2022)
79. Postek, M. The scanning electron microscope. (1997).
80. Khursheed, A. Scanning electron microscope optics and spectrometers. *Scanning Electron Microsc. Opt. Spectrometers* 1–403 (2010). doi:10.1142/7094

81. Binnig, G., Quate, C. F. & Gerber, C. Atomic force microscope. *Phys. Rev. Lett.* **56**, 930–933 (1986).
82. Marti, O., Drake, B. & Hansma, P. K. Atomic force microscopy of liquid-covered surfaces: Atomic resolution images. *Appl. Phys. Lett.* **51**, 484–486 (1987).
83. micro/nanotribology, O. M.-H. of & 1999, undefined. AFM instrumentation and tips. *books.google.com*
84. Raman, C., Nature, K. K. & 1928, undefined. A new type of secondary radiation. *nature.com*
85. A Beginner's Guide to ICP-MS, Mass Spectrometry basics | Agilent. Available at: https://www.agilent.com/en/support/atomic-spectroscopy/inductively-coupled-plasma-mass-spectrometry-icp-ms/icp-ms-instruments/what-is-icp-ms-icp-ms-faqs. (Accessed: 27th June 2022)
86. Liu, X. *et al.* A porous nickel cyclotetraphosphate nanosheet as a new acid-stable electrocatalyst for efficient hydrogen evolution. *Nanoscale* **10**, 9856–9861 (2018).
87. Lv, C., Xu, S., Yang, Q., Huang, Z. & Zhang, C. Promoting electrocatalytic activity of cobalt cyclotetraphosphate in full water splitting by titanium-oxide-accelerated surface reconstruction. *J. Mater. Chem. A* **7**, 12457–12467 (2019).

Chapter 2

Excellent hydrogen generation from ultrathin nanosheets of cobalt cyclotetraphosphate

2.1. Introduction

The requirement of energy demand is rising day-by-day because of the high rate of industrialization, economic growth and high-quality lifestyle of people. The non-renewable sources such as coal, coke, petroleum oil are being used currently to meet the gap of energy demands. However, high consumption of fossil fuels is limited by their less abundance as well as environmental pollution. The requirement of clean energy can be addressed via utilizing environment-friendly resources like fuel cells, supercapacitors and atomic energy. The generation of hydrogen through water splitting gains much researcher's attention due to no generation of carbon footprint. Hydrogen as a fuel is one of the best renewable sources due to its high energy density (142 MJ/Kg) value and water as byproduct.[1–3] For this purpose, electrolysis of water is considered as the superior and green forthcoming technique to produce hydrogen.[4,5] During electrolysis of water, hydrogen is evolved at the negative electrode (cathode) via evolution reaction (HER) process while oxygen is evolved at the positive electrode (anode) via oxygen evolution reaction (OER) process potential of 0 V and 1.23 V against RHE respectively. To facilitate the HER kinetics, potential should be towards 0 V against RHE and at the same time the amount of evolved hydrogen should be high. For this reason, an electrocatalyst is utilized, which can decrease energy consumption and increase hydrogen production.[6–9] Noble materials such as platinum, palladium based electrocatalyst are the state-of-art materials for the production of hydrogen during electrolysis of water. The implementation of these electrocatalyst are restricted due to their limited abundance and high cost.[10–12] Nowadays, a lot of research is going on to design non-noble electrocatalysts which have superior electrocatalytic properties as well as economical for hydrogen production. In recent years, various non-noble metal electrocatalysts like metal chalcogenides[13–15], phosphides[16–18], nitrides[19–21] and carbides [22–24], as well as their hetero-structure, have been reported for the production of hydrogen.[10,25,26] Among these, metal phosphates are active electrocatalyst towards OER in basic medium but their electrocatalytic activity towards HER are very less known.[27] Recently, a new class of metal cyclotetraphosphate has been synthesized and used as an electrocatalyst for the production of hydrogen.[28] The electrocatalytic study of metal cyclotetraphosphate reveals that the higher activity of catalyst due to its polymeric structure and the development of inductive effect of $P_4O_{12}^{2-}$ cyclic ring.[28] Earlier, *Cuncai et. al.* have synthesized cobalt cyclotetraphosphate

microparticles (~ 1 ± 0.4 µm) via annealing method and utilized these particles as a catalyst for HER and shows 238 mV overpotential at -20 mA/cm^2 current density with 152 mV/dec Tafel slope value.[29] Further, TiO_2 has been incorporated in $Co_2P_4O_{12}$ by the same group and 81 mV overpotential to achieve -20 mA/cm^2 currnet density with Tafel slope value of 87 mV/dec.[29] Among various synthesis process, micellar route is a versatile nanomaterial synthesis process, which facilitates to control the particle properties such as size, geometry,morphology, homogeneity and surface area.[30] It has been reported that various types of dielectric, magnetic, and optical material along with nanorods of a variety of transition metal (Cu, Ni, Mn, Zn, Co and Fe) oxalates has been synthesized through this process.[31–34] In view of the above facts, we have designed a new process for stabilization of ultrafine cobalt cyclotetraphospahte nanosheets using cobalt oxalate rods at ambient pressure and low temperature. The synthesis of cobalt oxalate rods has been done using the micellar route at room temperature and then phosphorization has been done in the presence of P_2O_5. The as-obtained cobalt cyclotetraphosphate shows excellent H_2 evolution properties. Cobalt cyclotetraphosphate nanosheets show an overpotential of 118 mV to reach the current density of -20 mV/cm^2 and Tafel slope of 97 mVdec^{-1} that outperform earlier reports of cobalt cyclotetraphosphate.

2.2. Materials and methods

Cobalt nitrate hexahydrate [Co $(NO_3)_2.6H_2O$, 98 %, Merck], di-ammonium oxalate [$(NH_4)_2C_2O_4$, 99 %, Merck], di-phosphorus pentoxide (P_2O_5, 95 %, CDH), Cetyl tri-methyl ammonium bromide (CTAB, 99 %, CDH), Pt/C **(**20 wt% of platinum on carbon, Sigma Aldrich**)** and methanol (CH_3OH, 99 % CDH) have been used as starting material. All the chemicals were used without any further purification.

The cobalt cyclotetraphosphate ($Co_2P_4O_{12}$) was synthesized using cobalt oxalate and P_2O_5 as precursors via the solid-state method. The synthesis of cobalt oxalate precursor was done by micelle route using CTAB as a capping agent. For the synthesis of cobalt oxalate, aqueous solution of, Co $(NO)_3.6H_2O$ (0.1 M) and $(NH_4)_2C_2O_4$ (0.1 M) were prepared. Further, 1 % of CTAB was added to both the solution and stirred till complete dissolution. The above solutions were mixed and stirred overnight which results in the formation of a pink colour precipitate. The resulting precipitate was collected after centrifugation and washed with a mixture of methanol and chloroform (1:1 v/v) and dried in a hot air oven. The as-obtained cobalt oxalate

precursor was further used as the precursor for the synthesis of cobalt cyclotetraphosphate. To synthesize cobalt cyclotetraphosphate, first cobalt oxalate and P_2O_5 were taken in 1:1 w/w ratio in mortar-pestle and grinded to get a homogeneous mixture. The prepared mixture was calcined at 350 ^oC for 12 h in air. A violet colored sample was obtained.

2.3. Characterization

Powder x-ray diffraction pattern of all the samples was carried out with Cu-Kα (λ= 1.54Å) radiation using Bruker D8 advance diffractometer. The morphological studies were examined by scanning electron microscope (SEM, JEOL JSM-IT30) and transmission electron microscope (TEM, JEOL JEM-2100) coupled with energy-dispersive X-ray spectroscopy (EDS) analyzer. Atomic force microscope (AFM, Bruker multimode 8) was used to find out the thickness of nanosheets. Zeta potential measurements were done using Malvern Zetasizer NanoZSP (Malvern Instrument, Malvern, UK) by dispersing all the samples in ultrapure water. Fourier transform infrared spectroscopy (FTIR) studies were carried out by Bruker, vertex 70 and surface area was carried out using Quantachrome autosorb iQ_2, BET surface area analyzed under the liquid nitrogen atmosphere. The sample was degassed at 150 °C for 6 h before analysis. To check the wettability properties DSA25-KRUSS GmbH was used to determine the contact angle by the sessile drop method. Electrochemical measurements were performed on Metrohm PGSTAT-30 Autolab workstation.

2.3.1. Preparation of electrodes

Working electrodes were prepared by coating of cobalt cyclotetraphosphate ink on a graphite substrate. To prepare cobalt cyclotetraphosphate ink, 10 mg of $Co_2P_4O_{12}$ sample was dispersed in 300 µl of ethanol and 100 µl of ethylene glycol solution and sonicated for 1 h. Further, 20 µl of Nafion was added to the above dispersion and sonicated for another 15 minutes. The as-prepared dispersion (60 µl) was drop casted on graphite substrate followed by curing in a hot air oven at 60 ºC for 2 h.

2.3.2. Preparation of Platinum/ Carbon (Pt/C) electrode:

A 5 mg of catalyst (20 wt% of platinum on carbon from Sigma Aldrich) was dispersed in a 200 µl of ethanol and sonicated for 45 minutes. Further, 5 µl of Nafion was added and sonicated for 15 minutes. The as-prepared solution (5 µl) was drop cast on glassy carbon and dried under vacuum for 4 h.

2.3.3. Electrochemical activity measurements

All electrochemical measurements were carried out in 0.5 M H_2SO_4 electrolyte using Metrohm PGSTAT-30 Autolab workstation consists of a conventional three-electrode system. A $Co_2P_4O_{12}$/graphite, graphite rod and 3 M Ag/AgCl was used as a working electrode, counter electrode and reference electrode respectively. Linear Sweep Voltammetry (LSV) of the working electrode was performed at 10 mV/sec in the potential window of 0 V to - 0.6 V vs RHE (reversible hydrogen electrode). The Tafel slope was calculated using equation $\eta = b \log j + x$, where η is the over-potential, b is the Tafel slope, j is the current density and x is the intercept corresponding to the exchange current density.[35] Electrochemical impedance spectroscopy (EIS) measurements were performed at -0.4 V vs Ag/AgCl in the frequency range 0.01 Hz to 100 kHz with amplitude of 10. All potentials measured in Ag/AgCl and converted to reversible hydrogen electrode (RHE) using the Nernst equation ($E_{RHE} = E_{Ag/AgCl} + 0.21\ V + 0.059\ pH$) [35]. To compare our electrocatalytic behavior of CoP_4O_{12} above electrochemical measurements were also carried with Pt/C as working electrode.

2.4. Result and discussion

Powder X-ray diffraction pattern of the as-obtained sample confirms the formation of pure cobalt oxalate dihydrate which belongs to the orthorhombic phase (JCPDS no. 00-025-250) having Cccm space group (*Figure 2.1a*).

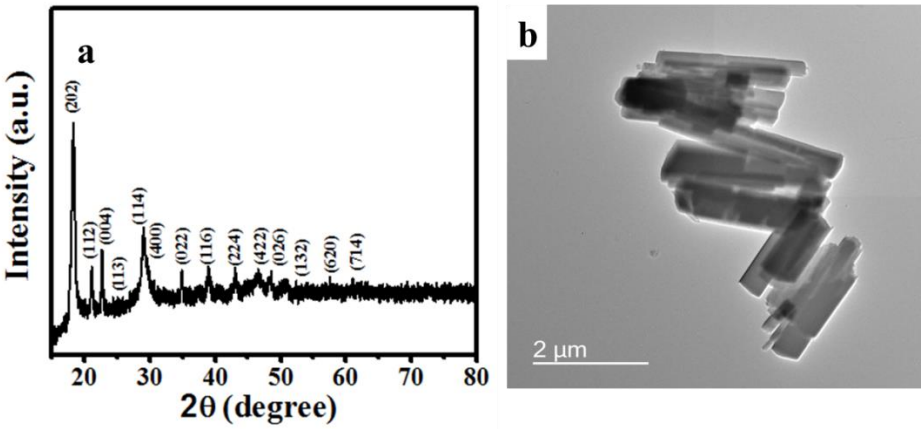

Figure 2.1. (a) Powder X-ray diffraction pattern of cobalt oxalate (b) TEM image of cobalt oxalate

The 2 theta value at 18.65, 21.29, 22.71, 24.85, 29.16, 30.07, 34.98, 39.08, 43.34, 46.81, 48.43, 52.52, 57.67 and 62.98 corresponds to (202), (112), (004), (113), (114), (400), (022),

(116), (224), (422), (026), (132), (620) and (714) plane respectively. Further, TEM studies of dehydrated cobalt oxalate shows the formation of rod-like morphology (diameter ~ 0.5 µm, length ~2.2 *; AR: 4.4) (*Figure 2.1b*). The proposed mechanism for the growth of rod-like morphology of cobalt oxalate has been explained as follows: It is noted that for the synthesis of cobalt oxalate, an aqueous solution of cobalt nitrate and ammonium oxalate were mixed separately with CTAB. The zeta potential study of Co^{2+} micelle and $C_2O_4^{2-}$ were + 11.2 mV and + 8.95 mV respectively. Further, CTAB forms a bilayer and the cobalt ion and oxalate ion were trapped in bilayer were combined together to form cobalt oxalate rod like structure.

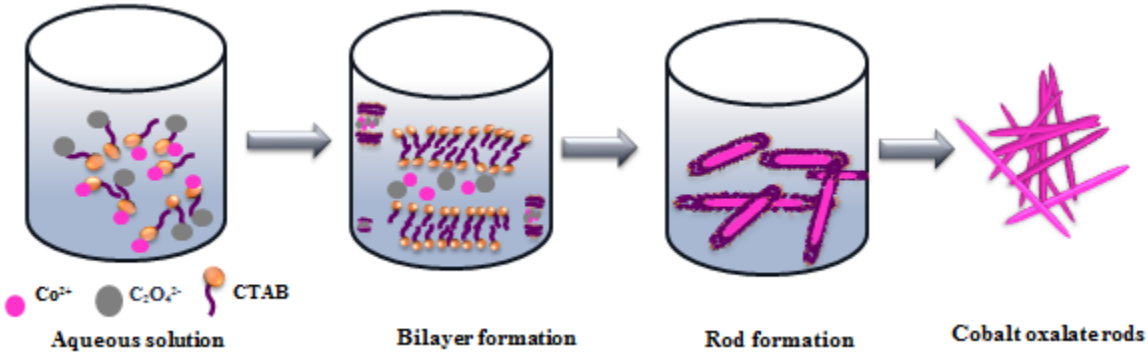

Figure 2.2. Mechanistic representation of formation of cobalt oxalate rods

The zeta potential of cobalt oxalate particles was -38.5 mV. CTAB is a cationic surfactant and cobalt oxalate is negatively surface charge. Therefore, it has been proposed that CTAB molecules arrange themselves on the linear arrangement of the metal and the ligand formed, due to templating effect of cationic CTAB molecules as shown schematically in *Figure 2.2*.[36] The as-obtained cobalt oxalate rods were further utilized for cobalt cyclotertraphosphate synthesis. To optimize the temperature of phosphorization, high-temperature XRD has been carried out at 35 ºC, 100 ºC, 200 ºC, 300 ºC, 350 ºC and 400 ºC temperature. It was found that the cobalt cyclotertraphosphate peaks start to arise from 300 ºC to 400 ºC (*Figure 2.3*). Therefore, the phosphorization process of cobalt oxalate was carried out at 350 ºC for 12 h at ambient pressure in the presence of air.

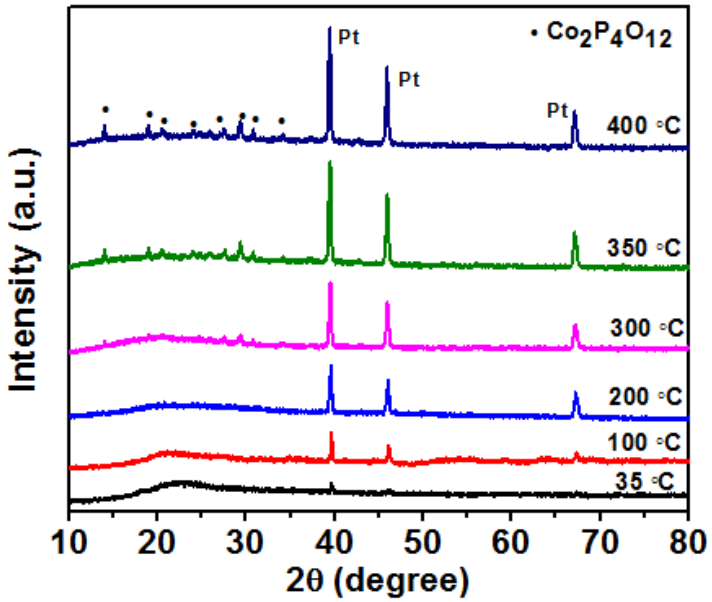

Figure 2.3. High temperature PXRD studies of mixture of cobalt oxalate and di-phosphorous pentaoxide

The XRD pattern of the sample obtained after heating at 350 ºC confirms the formation of pure monoclinic $Co_2P_4O_{12}$ having C2/c space group of JCPDS no. 01-084-2208) (*Figure 2.4a*). The 2 theta value at 13.66, 14.36, 19.37, 20.88, 23.74, 26.30, 27.97, 29.73, 31.12, 34.61, 37.60, 41.08, 43.05, 46.30, 52.02, 53.83, 57.08 and 60.70 corresponds to (110), (-202), (-112), (021), (-312), (112), (022), (-313), (400), (113), (420), (-133), (331), (-425), (422), (-206) and (531) plane respectively.

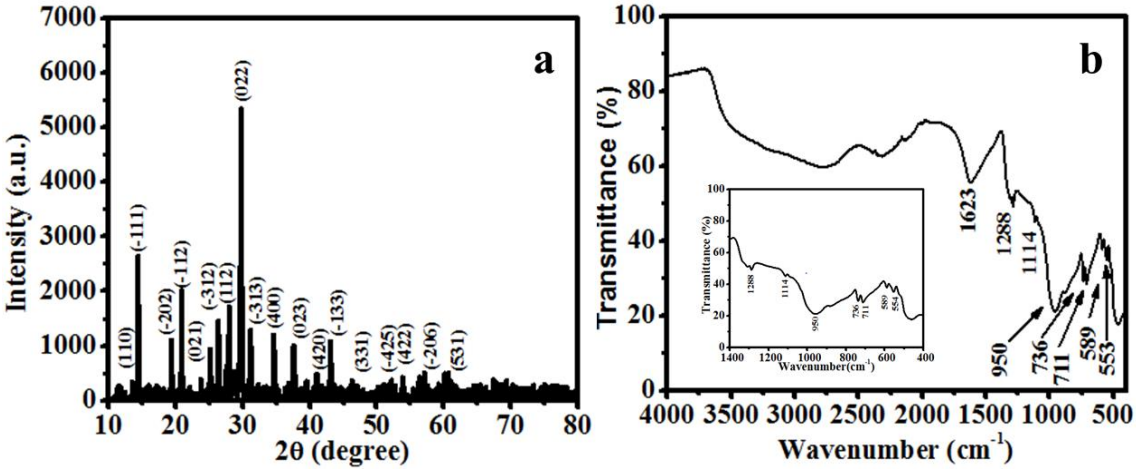

Figure 2.4. a) Powder X-ray diffraction pattern and b) FTIR analysis of $Co_2P_4O_{12}$

Further, an insight into the structure of cobalt cyclotetraphosphate has been explored using FTIR studies. The FTIR spectrum of cobalt cyclotetraphosphate showed the formation of $P_4O_{12}^{4-}$ cyclic ring. FTIR spectra showed a doublet (736 cm^{-1} and 711 cm^{-1}) due to the symmetrical vibrational mode of P-O-P bands that confirms the formation of cyclotetraphosphate ring of $(P_4O_{12})^{4-}$ (*Figure 2.4b*). The cyclic ring of $P_4O_{12}^{4-}$ contains two types of bonds P-O-P and PO_2^{2-}. PO_2^{2-} radical show an asymmetric and symmetric stretching frequency around 1288 cm^{-1}, 950 cm^{-1} and 600-400 cm^{-1} respectively. The asymmetric and symmetric stretching frequencies of P-O-P bridge were observed around 950 cm^{-1} and 800-700 cm^{-1} respectively [37]. The proposed balanced chemical **e**quation for the synthesis of $Co_2P_4O_{12}$ at 350 °C is

$$2CoC_2O_4.2H_2O + 2P_2O_5 + O_2 \rightarrow Co_2P_4O_{12} + 4CO_2 + 4H_2O$$

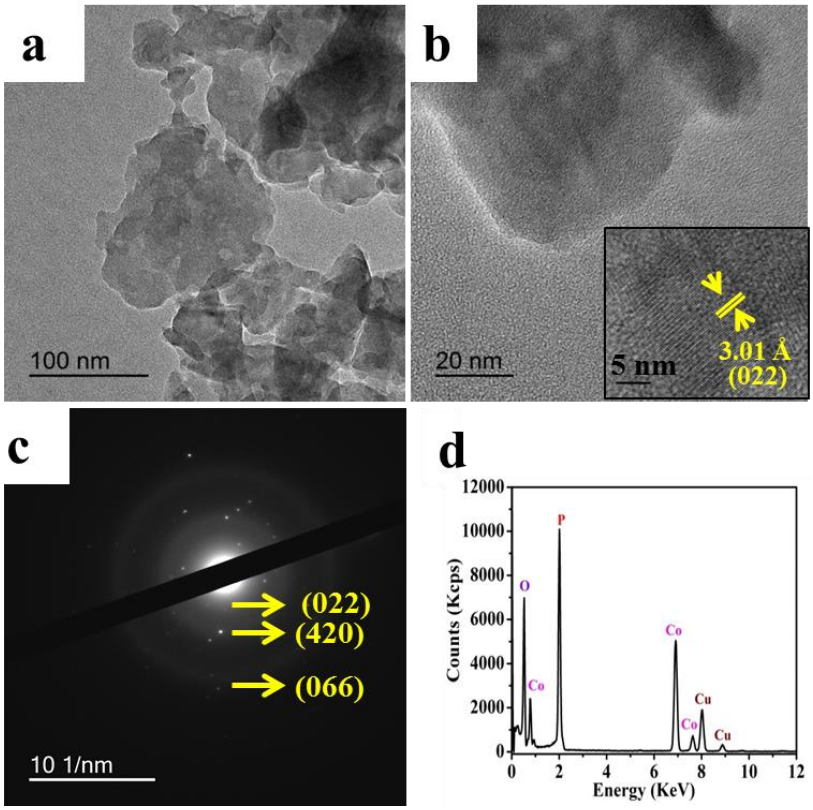

Figure 2.5. a)TEM, b) HRTEM Image c) SAED pattern and d) the corresponding EDAX of $Co_2P_4O_{12}$

Transmission electron microscopic study of cobalt cyclotetraphosphate indicated the formation of sheet-like morphology of size ~ 120-150 nm (*Figure 2.5a*). High resolution

(HR) TEM revealed distinct lattice fringes of the interplanar distance of 3.01 nm, which corresponds to (022) of cobalt cyclotetraphosphate (*Figure 2.5b*). The selected area electron diffraction (SAED) pattern of the CoP_4O_{12} sheets shows diffraction pattern which are well indexed to (022), (420), and (066) plane of $Co_2P_4O_{12}$ which are in good agreement with XRD results (*Figure 2.5c*).For elemental composition of CoP_4O_{12} energy dispersive X-ray spectroscopy has been done and shows presence of Co, O and P (*Figure 2.5d*).

Further, atomic force microscopic (AFM) studies have been done to measure the thickness of CoP_4O_{12} sheets. The AFM studies showed the ultrathin sheet (thickness ~ 1-2 nm) of cobalt cyclotetraphosphate (*Figure 2.6*). *Figure 2.6b-c*, showed the thickness of cobalt cyclotetraphosphate of position 1 and 2 as indicated in *Figure 2.6a*.

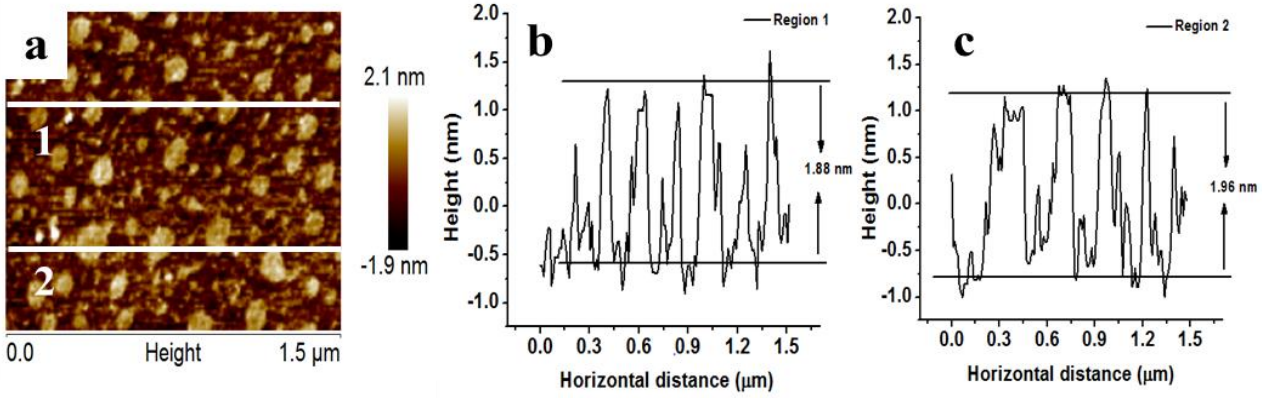

Figure 2.6. a) AFM image b) and c) the corresponding height profiles along the white line of region 1, 2 of $Co_2P_4O_{12}$

The surface area and pore size play an important role in the electrocatalytic activity. The surface area and pore radii were determined from Brauner-Emmett-Teller (BET) and Barrett-Joyner-Halenda (BJH) method by using nitrogen adsorption/desorption isotherms. The surface area of $Co_2P_4O_{12}$ is 6.1 m^2/g (*Figure 2.7a*). The pore radii of as obtained $Co_2P_4O_{12}$ was 8.7 nm (*Figure 2.7b*) and earlier report $Co_2P_4O_{12}$ has pore diameter was 5.8 nm and surface area was 23.91 m^2/g[29]. The electrochemical surface area of the catalyst were also calculated using C_{dl} method. For this CV scans were obtained with different scan rates in non-faradaic region as shown in *Figure 2.8*. The C_{dl} and ECSA value of $Co_2P_4O_{12}$ is 5 mF/cm^2 and 125 respectively.

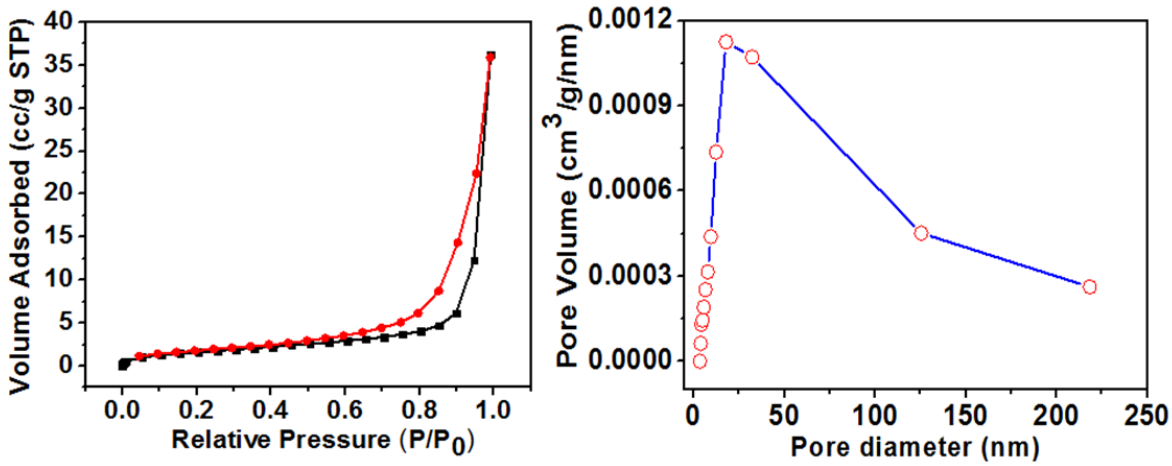

Figure 2.7. a) BET adsorption-desorption isotherm and b) BJH pore-size distribution analysis of $Co_2P_4O_{12}$

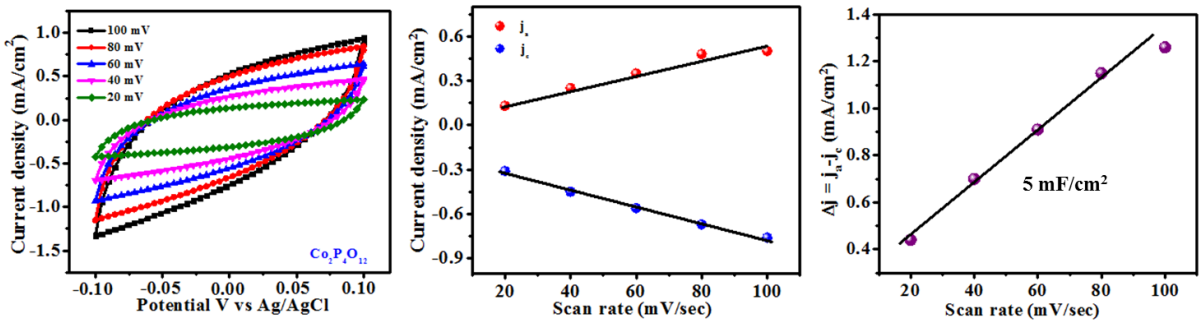

Figure 2.8. (a) CV curves for C_{dl} measurement at different scan rates (b-c) capacitive current at 0.00 V

The wettability property of the prepared catalysts was evaluated by using drop shape analyzer by using the sessile drop contact angle method. To evaluate the surface nature (hydrophilic/hydrophobic) of cobalt cyclotetraphospshate, 3 µL of the water droplet was drop casted on the surface of $Co_2P_4O_{12}$/graphite as shown in *Figure 2.9.* Interestingly, as soon as the imposed droplet falls on the catalyst surface, the droplet gets adsorbed instantly showing 0° contact angle (*Figure 2.9b*). These results confirm the super hydrophilic nature of the $Co_2P_4O_{12}$. This phenomenon leads to the faster penetration of the electrolyte which will support the easy release of the gas bubbles during catalysis.[38–41] The same measurements have been done for the bare graphite substrate and the contact angle at the graphite surface was found to be 83.3°. These results indicate the hydrophobic nature of the surface compare to the prepared catalyst (*Figure 2.9a*). During catalysis process, evolution of plenty of gas bubbles from the surface of electrodes takes place. However, if the adhesion of these bubbles is high on the surface of electrodes then it will lead to an increase in ohmic resistance

between the surface and the electrode. This leads to the blockage of the electrocatalytic active sites and further diffusion of the electrolyte becomes difficult through the active sites. The surface phenomenon plays vital role during gas evolution catalysis.

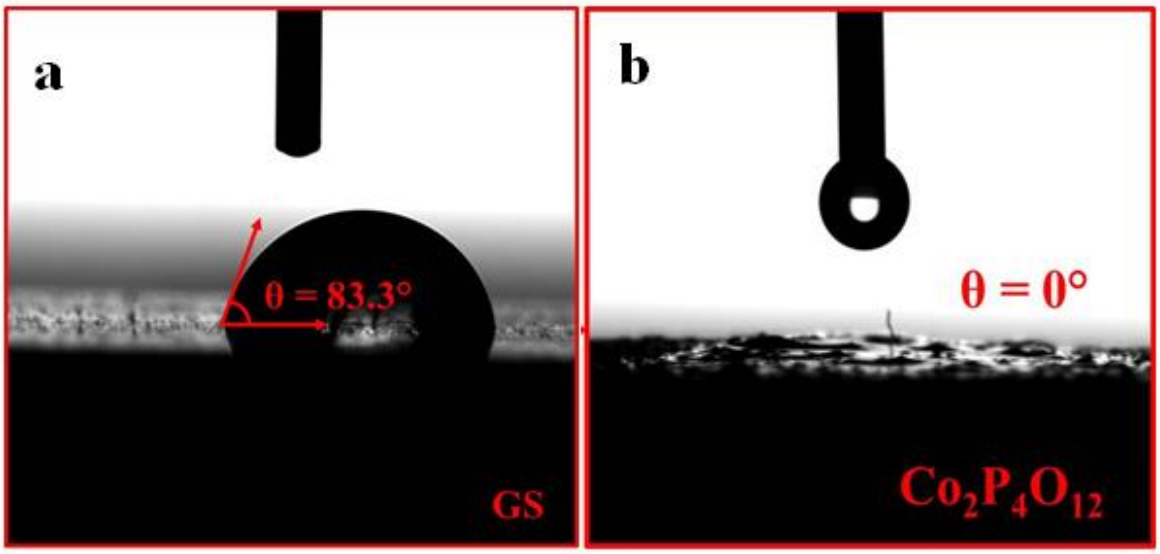

Figure 2.9. Contact angle studies of a) Bare graphite and b) $Co_2P_4O_{12}$

2.4.1. Electrochemical properties of cobalt cyclotetraphosphate

Figure 2.10a shows the competitive LSV curve of bare graphite, Pt/C and $Co_2P_4O_{12}$ coated graphite substrate. The LSV study reveals that the $Co_2P_4O_{12}$ nanosheets and Pt/C show a low overpotential (η_{20} = 118 mV) and (η_{20} = 54 mV) respectively. Here, it worth to mention that the onset potential is almost near to 0 V for both the cases. It is well known that the overpotential for an electrocatalyst is the difference between the zero potential and the onset potential to initiate hydrogen evolution process of the corresponding catalyst. Thus, such low overpotential suggests that $Co_2P_4O_{12}$ has high electrocatalystic performance towards hydrogen evolution reaction. To study the kinetics and the catalytic activity of as-prepared electrode materials, Tafel slope was calculated by fitting linear regions of Tafel plots into by equation $\eta = b \log j + x$. the tafel slope of bare graphite, Pt/C and $Co_2P_4O_{12}$ shows a Tafel slope of 343, 38 and 97 mV/dec respectively (*Figure 2.10b*). The low Tafel slope refers to that $Co_2P_4O_{12}$ has a high charge transfer kinetics which makes $Co_2P_4O_{12}$ a highly efficient electrocatalyst towards To investigate the effect of graphite surface on catalytic efficiency,

the linear sweep voltammetry (LSV) and Tafel slope of graphite under the same condition was measured.

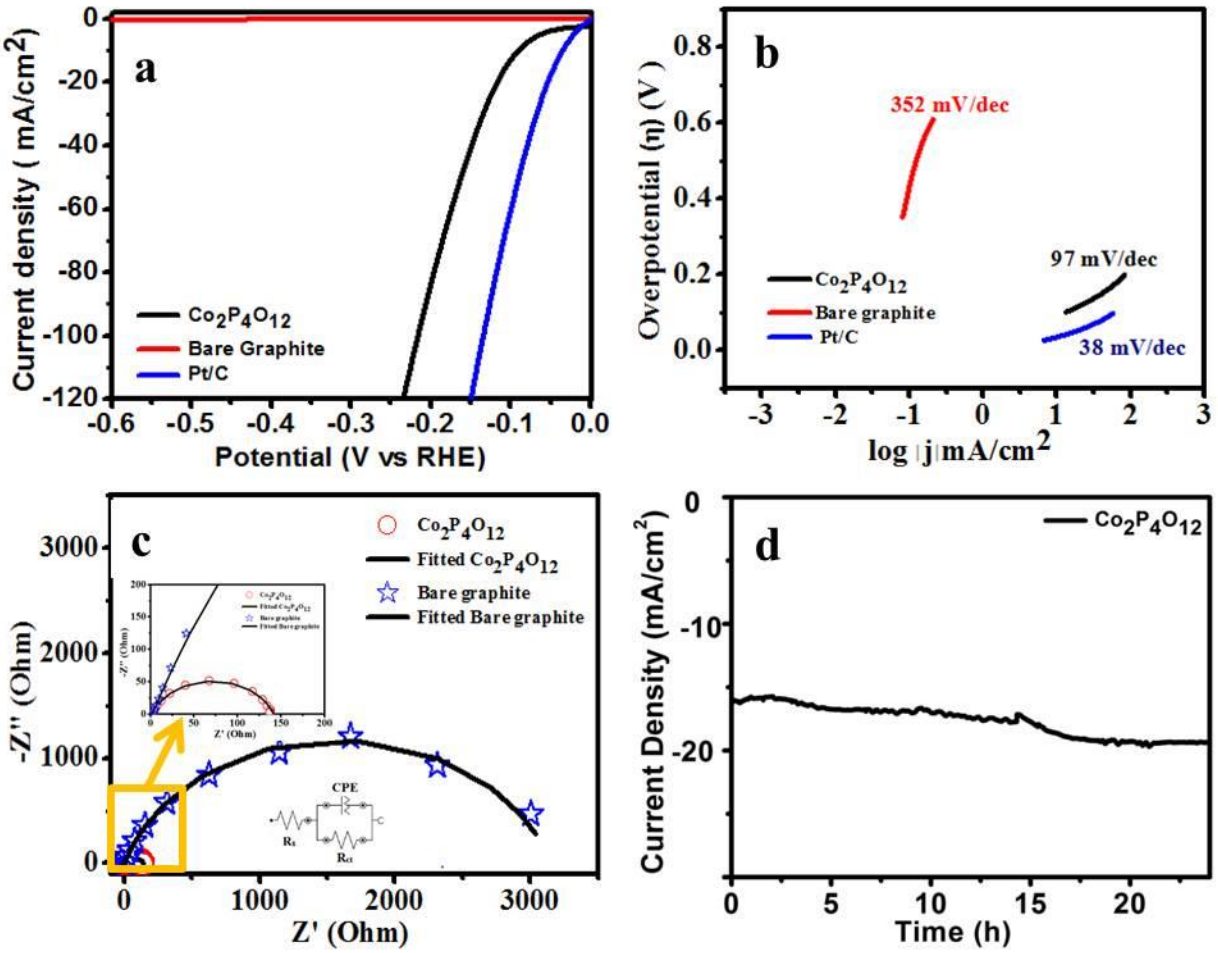

Figure 2.10. a) LSV curves, b) Tafel slope, c) EIS studies of $Co_2P_4O_{12}$ and bare graphite respectively and d) Chronoamperometric studies of $Co_2P_4O_{12}$

Graphite substrate does not achieve the benchmark current density and Tafel slope was found to be very high (323 mV/dec) which indicates negligible contribute of graphite substrate for hydrogen evolution reaction. To the best of our knowledge, there is only one report on cobalt cyclotertaphosphate coated on carbon fiber paper (CFP) which has been utilized for hydrogen generation [29]. In the earlier synthesis of $Co_2P_4O_{12}$ required complex steps including inert conditions for the formation of particles. However, in the present study, mild heating conditions have been used throughout the reaction which leads to the formation of ultrathin sheets having thickness 1.5 – 2 nm. Due to the reduction in the size of $Co_2P_4O_{12}$, the considerable decrease in overpotential (118 mV) and Tafel slope (97 mV/dec) has been

observed compared to the minimum reported overpotential (238 mV) and Tafel slope (152 mV/dec) for $Co_2P_4O_{12}$.[29] The comparison for hydrogen production performances with other electrocatalyst has given in *Table 2.1*. Moreover, due to the inductive effect of phosphate anions, the Mn atoms in the reported $Mn_3(PO_4)_2 \cdot 3H_2O$ catalyst have more nucleophilic character than those in MnO.[42] Therefore, it can also be concluded that the more nucleophilic character of Co atoms in $Co_2P_4O_{12}$ activates more catalytic sites and enhances its HER activity.[42]

Table 2.1. Comparison of the hydrogen production performances with other electrocatalyst

S.no.	Material	Electrolyte	Current density (j) (mV)	Overpotential (η) (mV)	Tafel slope (mV/dec)	References
1	CoP/CoMoP/NF HNAs	0.5 M H_2SO_4	10	125	61.1	[43]
2	CoPi/CoP	0.5 M H_2SO_4	10	112	99.8	[44]
3	CoP Film	1 M KOH	10	94	120	[45]
4	CoP/WS_2 Composite	0.5 M H_2SO_4	78	300	64.63	[46]
5	Cobalt phosphide/phosphate thin film	1 M KOH	30	430		[47]
		0.5 M H_2SO_4	30	175	53	
6	$TiO_2/Co_2P_4O_{12}$	1 M KOH	20	81	87	[29]
		0.5 M H_2SO_4	20	198	113	
7	Nickel @ Nitrogen doped carbon @ MoS_2 nanosheets	0.5 M H_2SO_4	10	82	47.5	[48]
8	$Ni_2P_4O_{12}$ nanosheets	0.5 M H_2SO_4	10	131	47.8	[28]
9	$NiCo_xP_y$/CC	0.5 M H_2SO_4	10	70	61	[49]

		1 M KOH	10	42	66	
10	Ni_5P_4 film	1 M KOH	10	150	59	[50]
		0.5 M H_2SO_4	10	140	40	
11	FeP/CN	0.5 M H_2SO_4	10	104	63.5	[51]
12	Mo_2C/C nanosheet	1 M KOH	10	125	72	[52]
		0.5 M H_2SO_4	10	180	71	
13	MoO_3@rRuO_2	0.5 M H_2SO_4	10	110	62	[53]
14	$Co_2P_4O_{12}$ nanosheets	0.5 M H_2SO_4	20	118	97	This work

To understand the insight of the reaction fundamental electrochemical activity of $Co_2P_4O_{12}$, electrochemical impedance spectroscopy (EIS) was done at – 40 mV vs RHE. *Figure 2.10c* shows the Nyquist plot of $Co_2P_4O_{12}$ in comparison with bare graphite. The obtained EIS curve was fitted with Nova 1.1 software, which was inbuilt with Metrohm. The EIS data were fitted with a constant phase element (CPE) and charge transfer resistance (Rct), which was in parallel to each other. The combination of CPE and Rct are in series combination with the solution resistance (R_s). $Co_2P_4O_{12}$ showed a low charge transfer resistance (R_{ct}) of 139 Ω as compared to graphite (R_{ct} of 800 Ω). The low value of Rct indicates the quick charge transfer process for HER activity. For a good catalyst and practical application, stability is a very important parameter. To check the stability of the catalyst chronoamperometric studies were performed at -0.1 V vs RHE in 0.5 M H_2SO_4 (*Figure 2.10d*). Current density vs time plot indicates that the current density remains almost constant up to 15 h and then there was hump near to 15 h arises might be due to broken bubbles formed on the surface and after that, there was little increase in current was observed. Therefore, based on above electrochemical studies, it can be concluded that a low overpotential, lower Tafel slope, high stability (24 h) of $Co_2P_4O_{12}$ makes it one of the efficient electrocatalyst for HER in highly acidic medium (0.5 M H_2SO_4). Post electrochemical study of the material has also been carried out by PXRD and shown in *Figure 2.11*. From the powder diffraction pattern it was found that after chronoamperometry study for 24 h, there is no change in the diffraction pattern and phase of $Co_2P_4O_{12}$ observed. The diffraction pattern is well matched with JCPDS no. 01-084-2208.

Hence, based on the above discussion, $Co_2P_4O_{12}$ nanosheets are one of the non-noble electrocatalysts for hydrogen evolution reaction.

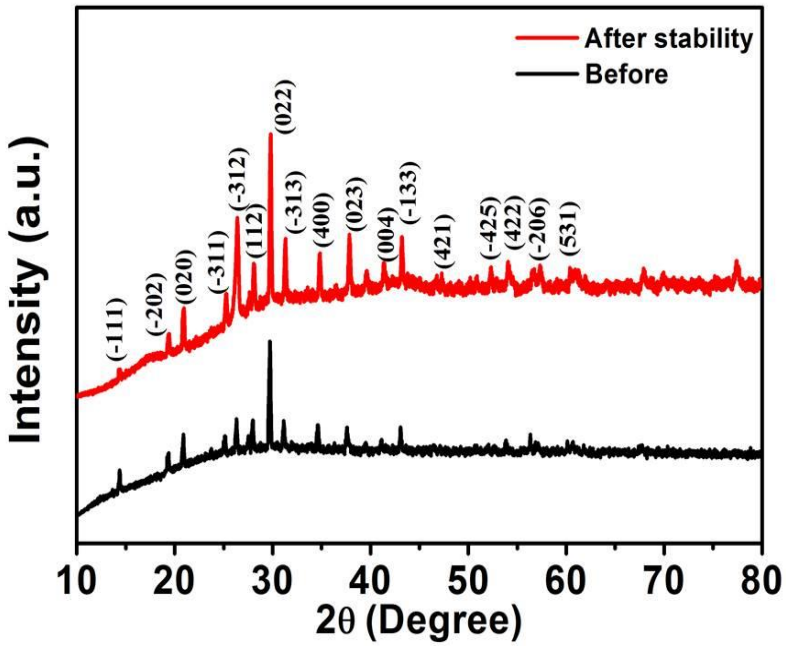

Figure 2. 11. Post stability Powder X-ray diffraction pattern of $Co_2P_4O_{12}$

2.5. Conclusions

In this present chapter, we have shown an energy-efficient process for the production of hydrogen through hydrogen evolution reaction (HER) using water splitting of ultrafine cobalt cyclotetraphosphate nanosheets in an acidic media. The synthesis of cobalt cyclotetraphosphate nanosheets (1.5 – 2 nm) was done at low temperature (350 ºC) and ambient pressure using phosphatization of cobalt oxalate rods. The synthesis of cobalt oxalate was carried out using micellar process at room temperature. Cobalt cyclotetraphosphate nanosheets exhibit a remarkable HER activity that shows a small overpotential of 118 mV to reach current density -20 mA/cm^2 in 0.5 H_2SO_4. It is worth to mention that the onset potential is almost 0 in the present study. It is believe that this work can offer a novel strategy to design high-performance electrocatalysts to replace the expensive noble metal catalysts for energy conversion applications.

2.6. References

1. Turner, J. A. Sustainable hydrogen production. *Science* **305**, 972–974 (2004).
2. Armstrong, R. C. *et al.* The frontiers of energy. *Nat. Energy* **1**, 1–8 (2016).

3. Bossel, U., Eliasson, B. & Taylor, G. The Future of the Hydrogen Economy: Bright or Bleak? *Cogeneration and Competitive Power Journal* **18**, 29–70 (2003).
4. Lewis, N. S. & Nocera, D. G. Powering the planet: Chemical challenges in solar energy utilization. *Proceedings of the National Academy of Sciences of the United States of America* **103**, 15729–15735 (2006).
5. Gray, H. B. Powering the planet with solar fuel. *Nature Chemistry* **1**, 7 (2009).
6. Amiinu, I. S. *et al.* Multifunctional Mo-N/C@MoS_2 Electrocatalysts for HER, OER, ORR, and Zn-Air Batteries. *Adv. Funct. Mater.* **27**, 1702300 (2017).
7. Kim, D., Whang, D. R. & Park, S. Y. Self-Healing of Molecular Catalyst and Photosensitizer on Metal-Organic Framework: Robust Molecular System for Photocatalytic H2 Evolution from Water. *J. Am. Chem. Soc.* **138**, 8698–8701 (2016).
8. Zhu, J., Hu, L., Zhao, P., Lee, L. Y. S. & Wong, K. Y. Recent Advances in Electrocatalytic Hydrogen Evolution Using Nanoparticles. *Chemical Reviews* **120**, 851–918 (2020).
9. Lu, J., Yin, S. & Shen, P. K. Carbon-Encapsulated Electrocatalysts for the Hydrogen Evolution Reaction. *Electrochem. Energy Rev.* **2**, 105–127 (2019).
10. Yuan, S. *et al.* A universal synthesis strategy for single atom dispersed cobalt/metal clusters heterostructure boosting hydrogen evolution catalysis at all pH values. *Nano Energy* **59**, 472–480 (2019).
11. Pu, Z., Amiinu, I. S., Kou, Z., Li, W. & Mu, S. RuP_2 -Based Catalysts with Platinum-like Activity and Higher Durability for the Hydrogen Evolution Reaction at All pH Values. *Angew. Chemie Int. Ed.* **56**, 11559–11564 (2017).
12. Pu, Z. *et al.* A universal synthesis strategy for P-rich noble metal diphosphide-based electrocatalysts for the hydrogen evolution reaction. *Energy Environ. Sci.* **12**, 952–957 (2019).
13. Tiwari, A. P., Kim, D., Kim, Y., Prakash, O. & Lee, H. Highly active and stable layered ternary transition metal chalcogenide for hydrogen evolution reaction. *Nano Energy* **28**, 366–372 (2016).
14. McAllister, J. *et al.* Tuning and mechanistic insights of metal chalcogenide molecular catalysts for the hydrogen-evolution reaction. *Nat. Commun.* **10**, 1–10 (2019).
15. Tan, S. M., Mayorga-Martinez, C. C., Sofer, Z. & Pumera, M. Bipolar

Electrochemistry Exfoliation of Layered Metal Chalcogenides Sb_2S_3 and Bi_2S_3 and their Hydrogen Evolution Applications. *Chem. – A Eur. J.* chem.201904767 (2020). doi:10.1002/chem.201904767

16. Xu, Y., Wu, R., Zhang, J., Shi, Y. & Zhang, B. Anion-exchange synthesis of nanoporous FeP nanosheets as electrocatalysts for hydrogen evolution reaction. *Chem. Commun.* **49**, 6656–6658 (2013).
17. Du, H., Kong, R. M., Guo, X., Qu, F. & Li, J. Recent progress in transition metal phosphides with enhanced electrocatalysis for hydrogen evolution. *Nanoscale* **10**, 21617–21624 (2018).
18. Ganesan, V., Kim, J. & Radhakrishnan, S. CoP Embedded in Hierarchical N-Doped Carbon Nanotube Frameworks as Efficient Catalysts for the Hydrogen Evolution Reaction. *ChemElectroChem* **5**, 1644–1651 (2018).
19. Yu, L. *et al.* A universal synthesis strategy to make metal nitride electrocatalysts for hydrogen evolution reaction. *J. Mater. Chem. A* **7**, 19728–19732 (2019).
20. Gong, S. *et al.* Noble-metal-free heterostructure for efficient hydrogen evolution in visible region: Molybdenum nitride/ultrathin graphitic carbon nitride. *Appl. Catal. B Environ.* **238**, 318–327 (2018).
21. Gangadharan, P. K., Unni, S. M., Kumar, N., Ghosh, P. & Kurungot, S. Nitrogen-Doped Graphene with a Three-Dimensional Architecture Assisted by Carbon Nitride Tetrapods as an Efficient Metal-Free Electrocatalyst for Hydrogen Evolution. *ChemElectroChem* **4**, 2643–2652 (2017).
22. Handoko, A. D. *et al.* Tuning the Basal Plane Functionalization of Two-Dimensional Metal Carbides (MXenes) to Control Hydrogen Evolution Activity. *ACS Appl. Energy Mater.* **1**, 173–180 (2018).
23. Kim, S. K., Qiu, Y., Zhang, Y. J., Hurt, R. & Peterson, A. Nanocomposites of transition-metal carbides on reduced graphite oxide as catalysts for the hydrogen evolution reaction. *Appl. Catal. B Environ.* **235**, 36–44 (2018).
24. Gao, Q., Zhang, W., Shi, Z., Yang, L. & Tang, Y. Noble-Metal-Free Electrocatalysts: Structural Design and Electronic Modulation of Transition-Metal-Carbide Electrocatalysts toward Efficient Hydrogen Evolution (Adv. Mater. 2/2019). *Adv. Mater.* **31**, 1970009 (2019).

25. Zeng, M. & Li, Y. Recent advances in heterogeneous electrocatalysts for the hydrogen evolution reaction. *Journal of Materials Chemistry A* **3**, 14942–14962 (2015).
26. Wang, Q. *et al.* MOF-Derived Copper Nitride/Phosphide Heterostructure Coated by Multi-Doped Carbon as Electrocatalyst for Efficient Water Splitting and Neutral-pH Hydrogen Evolution Reaction. *ChemElectroChem* **7**, 289–298 (2020).
27. Kanan, M. W. & Nocera, D. G. In situ formation of an oxygen-evolving catalyst in neutral water containing phosphate and Co^{2+}. *Science (80-.).* **321**, 1072–1075 (2008).
28. Liu, X. *et al.* A porous nickel cyclotetraphosphate nanosheet as a new acid-stable electrocatalyst for efficient hydrogen evolution. *Nanoscale* **10**, 9856–9861 (2018).
29. Lv, C., Xu, S., Yang, Q., Huang, Z. & Zhang, C. Promoting electrocatalytic activity of cobalt cyclotetraphosphate in full water splitting by titanium-oxide-accelerated surface reconstruction. *J. Mater. Chem. A* **7**, 12457–12467 (2019).
30. Malik, M. A., Wani, M. Y. & Hashim, M. A. Microemulsion method: A novel route to synthesize organic and inorganic nanomaterials. 1st Nano Update. *Arabian Journal of Chemistry* **5**, 397–417 (2012).
31. Ganguli, A. K., Ganguly, A. & Vaidya, S. Microemulsion-based synthesis of nanocrystalline materials. *Chem. Soc. Rev.* **39**, 474–485 (2010).
32. Ahmad, T., Ganguly, A., Ahmed, J., Ganguli, A. K. & Alhartomy, O. A. A. Nanorods of transition metal oxalates: A versatile route to the oxide nanoparticles. *Arabian Journal of Chemistry* **4**, 125–134 (2011).
33. Vaidya, S., Ahmed, J. & Ganguli, A. K. Controlled synthesis of nanomaterials using reverse micelles. *Def. Sci. J.* **58**, 531–544 (2008).
34. Ahmad, T. *et al.* Chemistry of reverse micelles: A versatile route to the synthesis of nanorods and nanoparticles. in *Materials Research Society Symposium Proceedings* **1142**, 75–88 (2009).
35. Yadav, K. K. *et al.* Synthesis of zirconium diboride and its application in the protection of stainless steel surface in harsh environment. *J. Solid State Electrochem.* (2019). doi:10.1007/s10008-019-04408-0
36. Roy, M., Ghosh, S. & Naskar, M. K. Ligand-assisted soft-chemical synthesis of self-assembled different shaped mesoporous Co3O4: Efficient visible light photocatalysts. *Phys. Chem. Chem. Phys.* **17**, 10160–10169 (2015).

37. Boonchom, B. & Vittayakorn, N. A rapid synthesis of cobalt cyclotetraphosphate Co_2P 4O12 at low temperature. in *Ceramics International* **39**, (2013).
38. Xu, W., Lu, Z., Sun, X., Jiang, L. & Duan, X. Superwetting Electrodes for Gas-Involving Electrocatalysis. *Acc. Chem. Res.* **51**, 1590–1598 (2018).
39. Ghadge, S. D. *et al.* Experimental and Theoretical Validation of High Efficiency and Robust Electrocatalytic Response of One-Dimensional (1D) $(Mn,Ir)O_2$:10F Nanorods for the Oxygen Evolution Reaction in PEM-Based Water Electrolysis. *ACS Catal.* **9**, 2134–2157 (2019).
40. Wenzel, R. N. Resistance of solid surfaces to wetting by water. *Ind. Eng. Chem.* **28**, 988–994 (1936).
41. Zhang, P., Wang, S., Wang, S. & Jiang, L. Superwetting surfaces under different media: Effects of surface topography on wettability. *Small* **11**, 1939–1946 (2015).
42. Jin, K. *et al.* Hydrated manganese(II) phosphate $(Mn_3(PO_4)_2{\cdot}3H_2O)$ as a water oxidation catalyst. *J. Am. Chem. Soc.* **136**, 7435–7443 (2014).
43. Jiang, D. *et al.* CoP3/CoMoP Heterogeneous Nanosheet Arrays as Robust Electrocatalyst for pH-Universal Hydrogen Evolution Reaction. *ACS Sustain. Chem. Eng.* **7**, 9309–9317 (2019).
44. Chen, Z. *et al.* Room-temperature preparation of cobalt-based electrocatalysts through simple solution treatment for selectively high-efficiency hydrogen evolution reaction in alkaline or acidic medium. *J. Nanomater.* **2018**, (2018).
45. Jiang, N., You, B., Sheng, M. & Sun, Y. Electrodeposited Cobalt-Phosphorous-Derived Films as Competent Bifunctional Catalysts for Overall Water Splitting. *Angew. Chemie - Int. Ed.* **54**, 6251–6254 (2015).
46. Jin, J. *et al.* CoP nanoparticles combined with WS2 nanosheets as efficient electrocatalytic hydrogen evolution reaction catalyst. *Int. J. Hydrogen Energy* **42**, 3947–3954 (2017).
47. Yang, Y., Fei, H., Ruan, G. & Tour, J. M. Porous cobalt-based thin film as a bifunctional catalyst for hydrogen generation and oxygen generation. *Adv. Mater.* **27**, 3175–3180 (2015).
48. Shah, S. A. *et al.* Nickel@Nitrogen-Doped Carbon@MoS_2 Nanosheets: An Efficient Electrocatalyst for Hydrogen Evolution Reaction. *Small* **15**, 1804545 (2019).

49. Song, S. *et al.* Plasma-assisted synthesis of hierarchical NiCoxPy nanosheets as robust and stable electrocatalyst for hydrogen evolution reaction in both acidic and alkaline media. *Electrochim. Acta* **331**, 135431 (2020).
50. Ledendecker, M. *et al.* The Synthesis of Nanostructured Ni_5P_4 Films and their Use as a Non-Noble Bifunctional Electrocatalyst for Full Water Splitting. *Angew. Chemie - Int. Ed.* **54**, 12361–12365 (2015).
51. Suliman, M. H., Adam, A., Siddiqui, M. N., Yamani, Z. H. & Qamar, M. Facile synthesis of ultrathin interconnected carbon nanosheets as a robust support for small and uniformly-dispersed iron phosphide for the hydrogen evolution reaction. *Carbon N. Y.* **144**, 764–771 (2019).
52. Wu, C. & Li, J. Unique Hierarchical Mo_2C/C Nanosheet Hybrids as Active Electrocatalyst for Hydrogen Evolution Reaction. *ACS Appl. Mater. Interfaces* **9**, 41314–41322 (2017).
53. Sadhanala, H. K., Harika, V. K., Penki, T. R., Aurbach, D. & Gedanken, A. Ultrafine Ruthenium Oxide Nanoparticles Supported on Molybdenum Oxide Nanosheets as Highly Efficient Electrocatalyst for Hydrogen Evolution in Acidic Medium. *ChemCatChem* **11**, 1495–1502 (2019).

Chapter 3

Surface phosphorization of nickel oxalate nanosheets to stabilize ultrathin nickel cyclotetraphosphate nanosheets for efficient hydrogen generation

3.1. Introduction

Due to changes in climate conditions, environmental issues and increasing demand for energy, researcher's attention is derived towards alternative sources of exhaustive renewable energy which are viable and eco-friendly.[1] Among all the alternatives of non-renewable sources fuel cells, water electrolysis and supercapacitors are considered the promising renewable process for energy application. Hydrogen (H_2) has the highest gravimetric energy density among all the energy sources[2] and it is known that H_2 is the only fuel which generates water as the combustion byproduct. Therefore, H_2 is considered as the best potential candidate for energy carrier in future which is clean energy source.[3–6] Currently, lots of effort is going towards the search of an eco-friendly as well as efficient methodology for the production of hydrogen. At present, steam methane reforming is one of the best methods for large scale production of hydrogen. However, the steam methane reforming process consumes fossil fuel, and it releases toxic gases such as CO_2.[7] Hydrogen production from the electrolysis of water is one of the superior techniques because it produces high purity hydrogen at large scale without emission of greenhouse gases.[8] It is well known that the electrolysis of water is carried out in two half-reactions, which are hydrogen evolution reaction (HER) and oxygen evolution reaction (OER). The well-known equation for half-cell reaction of HER is $2H^+ (aq) + 2\ e^- \rightarrow H_2\ (g)$.[9] To carry out this half-cell reaction, materials based on platinum are considered as the best electrocatalyst. However, the cost of platinum and its abundancy make them obstructed to be used in large scale production of H_2.[10] To overcome this problem, highly efficient low-cost electrocatalyst such as transition metal chalcogenides[11,12], carbides[13], nitrides [14,15], phosphides [16–20] and phosphates [21,22] are explored and used as alternative electrocatalyst due to their high abundance in nature. Transition metal phosphate has shown promising results to replace Pt-based materials because of the presence of active catalytic sites as well as increase the intrinsic conductivity of transition metal phosphate. To the best of our knowledge, only two reports have been published for metal cyclotetraphosphates, which act as an efficient electrocatalyst for HER in acidic medium. Lv et. al. synthesized cobalt cyclotetraphosphate via phosphorization of $Co_2(OH)_3Cl$ by NaH_2PO_2 in an N_2 atmosphere at 500 ºC.[21] Recently acid-stable nickel cycloteraphosphate nanosheets of 120 nm thick have been synthesized by Liu et. al. via low-temperature phosphorylation of nickel oxide in an inert atmosphere at 320 ºC which shows remarkable

hydrogen evolution reaction (overpotential 131.8 mV and stability of 80000 s in acidic media).[22] The stability and catalytic behavior of $Ni_2P_4O_{12}$ in the acidic medium are attributed to the inductive effect of $P_4O_{12}^{2-}$ ring.[23] In the present study, we have developed a low-temperature process to synthesize ultrathin $Ni_2P_4O_{12}$ nanosheets. The synthesis of $Ni_2P_4O_{12}$ nanosheets has been done by phosphorization of nickel oxalate sheets using di-phosphorous pentaoxide for the first time in the air. The electrocatalytic properties (HER) of sample S4 shows an onset potential of 37 mV and an overpotential (η_{10}) of 105 mV and stability up to 17 h in 0.5 M H_2SO_4.

3.2. Experimental

3.2.1. Materials and Methods

Nickel nitrate hexahydrate ($Ni(NO_3)_2.6H_2O$, 98 %, Merck, India), di-ammonium oxalate ($(NH_4)_2C_2O_4$, 99 %, Merck, India), di-phosphorus pentaoxide (P_2O_5, 95 %, CDH, India), Platinum/carbon (20 wt % of Pt/C, Sigma Aldrich, India), Cetyl tri-methyl ammonium bromide (CTAB, 99 %, CDH, India) and methanol (CH_3OH, 98 %, CDH, India) have been used as starting material. All the chemicals were used without any purification.

The synthesis of $Ni_2P_4O_{12}$ was carried out via thermal phosphorization of nickel oxalate precursor. First, nickel oxalate precursor was synthesized by micelle route at room temperature using CTAB as capping agent. An aqueous solution of 0.1 M Ni $(NO)_3.6H_2O$ (100 ml) and 0.1 M $(NH_4)_2C_2O_4$ (100 ml) were prepared individually by continuous stirring at room temperature. Further, 1 g CTAB had been added to both the solution in stirring condition till its complete dissolution. The as-prepared solutions were mixed and stirred for 0 h, 4 h, 8 h and 12 h at 1000 rpm. Green-colored precipitates were collected by centrifugation and washed with methanol and dried in the oven at 60 ºC. The as-obtained samples were nickel oxalate, which were further used as the precursors for the synthesis of nickel cyclotetraphosphate. Nickel oxalate precursor obtained at 0 h, 4 h, 8 h and 12 h and P_2O_5 were taken in 1:1 w/w ratio and grinded in mortar and pestle to get four homogeneous mixtures. The homogeneous mixtures were transferred in recrystallized alumina boat and heated at 350 ^oC at the rate of 150 ºC per hour for 12 h in air. The black color samples were obtained and represented as S1, S2, S3 and S4 using nickel oxalate at 0 h, 4 h, 8 h and 12 h respectively.

3.2.2 Preparation of working electrodes

Working electrodes were prepared by drop-casting dispersions of sample S1, S2, S3 and S4 on graphite substrate for electrochemical studies. The dispersions of samples were prepared by taking 5 mg of sample in 300 µl of ethanol and 100 µl of ethylene glycol solution and sonicated for 1 h. Further, 20 µl of Nafion was added to the above solutions and sonicated for another 15 min. The as-prepared dispersions (20 µl) were drop casted on graphite strip and dried in the oven at 60 ºC in air.

3.2.3. Preparation of Platinum/ Carbon (Pt/C) electrode:

A 5 mg of catalyst (20 wt% of platinum on carbon from sigma Aldrich) was dispersed in a 200 µl of ethanol and sonicated for 45 minutes. Further, 5 µl of nafion was added and sonicated for 15 min. The as prepared solution (5 µl) was drop casted on glassy carbon and dried under vacuum for 4 h.

3.2.4. Electrochemical measurements

All electrochemical measurements were performed using Metrohm PGSTAT-30 Autolab workstation with graphite rod as counter electrode and 3 M Ag/AgCl as reference electrode. All the electrochemical studies were conducted at room temperature in 0.5 M H_2SO_4 electrolyte. Linear Sweep Voltammetry (LSV) was done in the potential range (0 V to - 0.8 V) vs RHE at a scan rate 10 mV/sec. The Tafel slope was calculated using equation $\eta = b \log j + x$, where η is the over-potential, j is the current density, b is the Tafel slope, and x is the intercept corresponding to the exchange current density. Electrochemical impedance spectroscopy (EIS) measurements were performed at – 0.4 V vs Ag/AgCl in the frequency range 0.01 Hz to 100 kHz with amplitude of 10 mV. All potentials were measured with respect to Ag/AgCl and converted to reversible hydrogen electrode (RHE) using the Nernst equation; $E_{RHE} = E_{Ag/AgCl} + 0.21\ V + 0.059\ pH$.[24]

3.2.5. Calculation of Electrochemically active surface area (ECSA):

For calculating electrochemically active surface area (ECSA) of sample S4 ($Ni_2P_4O_{10}$ nanosheets), C_{dl} (double layer capacitance) was calculated from the CV curves in a potential range of - 0.15 – 0.05 V vs. RHE at different scan rate from 20 to 80 mV/s in the non-faradic region (Fig. S6a). There are two different ways to measure ECSA value, first is by

calculating double-layer charge currents from the CV data at different scan rate and second is by using electrochemical impedance spectroscopy (EIS) by measuring frequency-dependent impedance. Here we are using the first method for calculating double-layer charge current (C_{dl}) from cyclic voltammetry curves (CV). At a potential of - 0.05 V vs. RHE, the graph is plotted between current density (mA/cm^2) and scan rate (Fig. S6b). There is a linear relation in both the parameters in x and y-axis and from where the value of slope was calculated. The value of the slope gives us the C_{dl} value for $Ni_2P_4O_{12}$ nanosheets of sample S4 [25] .

$$C_{dl} = \frac{I_c}{v}$$

Where C_{dl} is the double-layer capacitance (mF/cm^2), I_c is current density (mA/cm^2) and ν is the scan rate (mV/s).

3.3. Result and discussion

In the present study, we have attempted to design a process for the stabilization of nickel cyclotetraphosphate nanosheets using nickel oxalate nanosheets and di-phosphorus pentaoxide at low temperature (350 ºC) for the first time. To achieve the low-temperature stabilization of $Ni_2P_4O_{12}$ nanosheets, nickel oxalate nanosheets have been synthesized at room temperature using the micellar route. As discussed in the experimental section, the synthesis of nickel oxalate was done using an aqueous CTAB capped nickel nitrate and ammonium oxalate solution. PXRD pattern of the as-synthesized sample indicates the formation of pure nickel oxalate having orthorhombic phase with Cccm space group (JCPDS no. 00-014-742) (*Figure 3.1a*).Further, SEM studies have been carried out for the morphological study of nickel oxalate, which reveals the formation of sheets like structures of size ~3.85 µm (*Figure 3.1b*). The more detailed microstructural and compositional analysis have been done by TEM and EDAX at an accelerating voltage of 200 kV. TEM image confirms the formation of nickel oxalate sheets (*Figure 3.2a*). EDAX of nickel oxalate sheets indicates the presence of nickel, carbon and oxygen (*Figure 3.2b*). Further, the thickness of nickel oxalate sheet has been investigated *via* AFM studies. AFM studies of the nickel oxalate sheet indicates that the thickness of sheet was ~ 5- 6 nm. (*Figure 3.1c-f).* It is well known that metal oxalate synthesis using cationic surfactant leads to the formation of cubes or rod-like morphology.[26] However, earlier synthesis of nickel oxalate sheets has been

done using soft chemistry where SDS-CTAB mixture was used as a linker. Here, for the first time formation of nickel oxalate sheets have been shown in the presence of cationic surfactant without using any complex reaction.

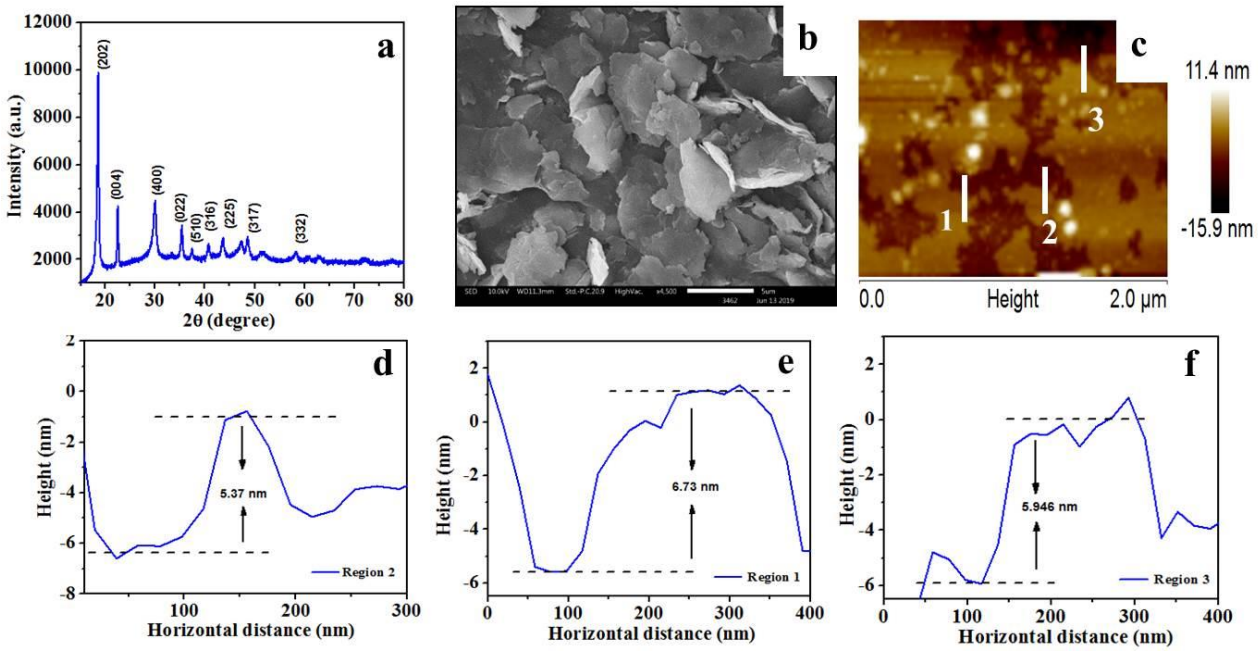

Figure 3.1. a) PXRD, b) SEM image, c) AFM image of $NiC_2O_4.2H_2O$, (d-f) corresponding height profiles along the white line of region 1, 2, 3

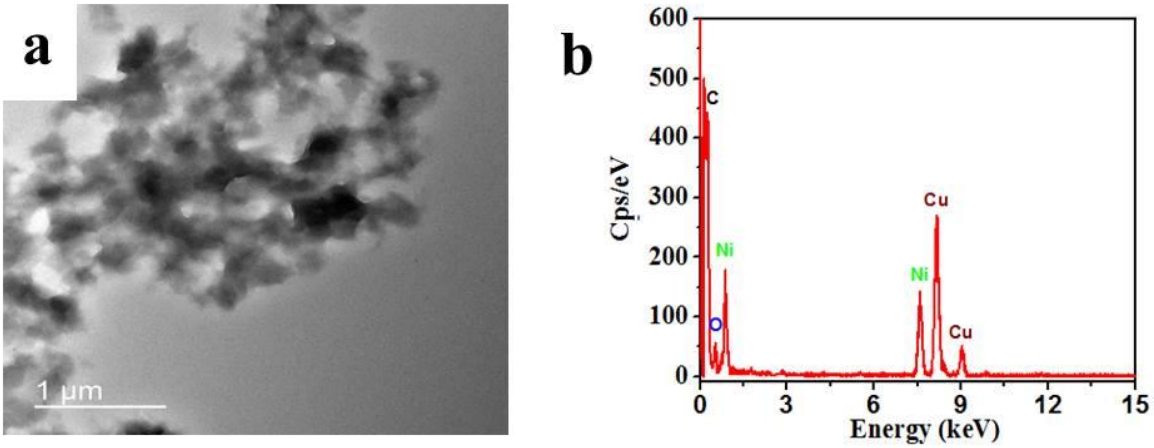

Figure 3.2. a) TEM image, b) EDAX of $NiC_2O_4.2H_2O$

The mechanism of synthesis of nickel oxalate nanosheets has been investigated using zeta potential measurement and time-dependent microscopic study. For the synthesis of nickel oxalate, as discussed in the experimental section aqueous solution of nickel nitrate and

ammonium oxalate were mixed separately with CTAB to form their micelle having zeta potential 19.3 mV and 3.2 mV respectively. Further, CTAB capped micelles of nickel nitrate and ammonium oxalate were mixed to obtain nickel oxalate. During the mixing process, the nickel ion and oxalate ion micelles were diffused to form nickel oxalate particles. These nickel oxalate particles were capped with a cationic surfactant as confirmed from zeta potential studies (-8.88 mV). CTAB is a cationic surfactant having positively charged head groups and nickel oxalate is negatively charged. The negatively charged nickel oxalate capped with CTAB forms an assembly around positive head groups of CTAB, and hence the growth of nickel oxalate takes place along the cationic chain of CTAB. This growth of nickel oxalate along the cationic chain leads to elongation of diameter for the formation of nickel oxalate sheets.[27]

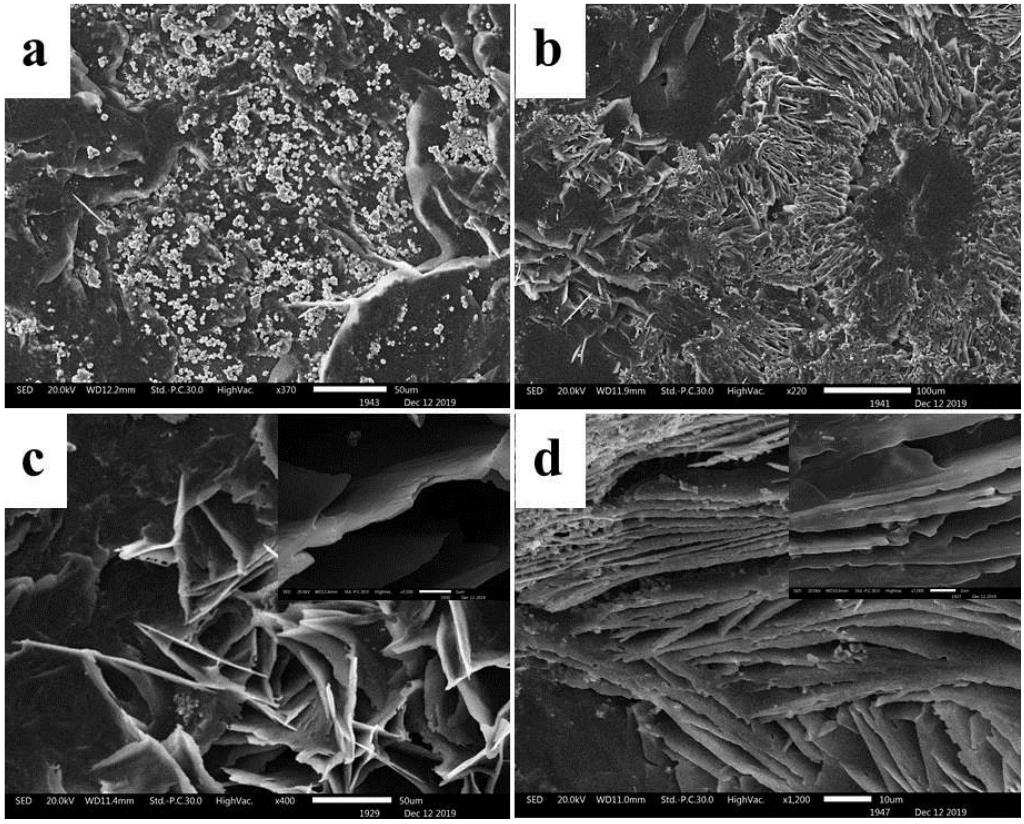

Figure 3.3. SEM micrographs of NiC_2O_4 at a) 0 h, b) 4 h, c) 8 h and d) 12 h

To study the growth of the nickel oxalate sheets, morphological studies were carried out by quenching the reaction at 0 h, 4 h, 8 h and 12 h respectively. When the reaction was

quenched immediately, SEM micrographs of nickel oxalate indicate that the particles of nickel oxalate (3.4 µm) were formed. As the reaction progress to 4 h nickel oxalate particles has started to agglomerate in sheet-like structures (49 µm) and after 8 h, formation of uniform nickel oxalate sheets (64 µm) takes place. Further ageing of reaction up to 12 h the sheets were fully grown as shown in (*Figure 3.3a-d).*

The as-obtained nickel oxalate sheets after 0 h, 4 h, 8 h and 12 h were further utilized for the synthesis of nickel cyclotertraphosphate by doing phosphorization using P_2O_5 as discussed in the experimental section. The phosphorization temperature was determined by the thermogravimetric analysis (TGA). First, thermal stability and phase transformation of $NiC_2O_4.2H_2O$ has been investigated via TGA/DTA study. *Figure 3.4a* indicates that, initially up to ~283 ºC, there is negligible change in weight; however, there is a sharp decrease in weight that starts from 300 ºC and ends at 429 ºC in two steps. The first step deals with the removal of water molecules from the nickel oxalate dihydrate, which corresponds to 33% weight loss in the temperature range 300 - 350 ºC. In the second step, in the temperature range of 350 - 430 ºC nickel oxalate (NiC_2O_4) decomposed into NiO (s) and CO_2 (g) [28]. It may be noted that P_2O_5 starts melting at 340 ºC while nickel oxalate is almost stable in argon atmosphere up to 300 ºC. The TGA curve of P_2O_5 (*Figure 3.4a*) clearly indicates that P_2O_5 is stable upto 500 ºC when heated alone.

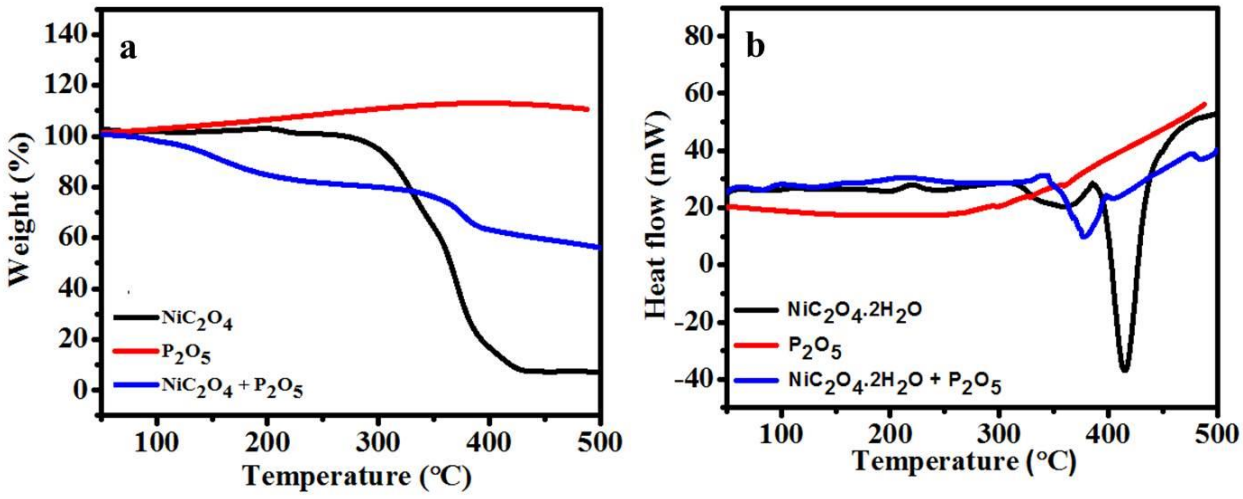

Figure 3.4. a) TGA and b) DTA curves of $NiC_2O_4.2H_2O$, P_2O_5 and $NiC_2O_4.2H_2O$ + P_2O_5

Further, P_2O_5 and $NiC_2O_4.2H_2O$ have been mixed in equal amount and TGA study has been done. Initial weight loss up to 285 ºC corresponds to the removal of adsorbed water. The

weight loss in the TGA curve of precursors started as the temperature increases, which might be due to the removal of water from a mixture of nickel oxalate and P_2O_5. Further, an increase in temperature leads to removal of CO_2 (~16% weight loss) as well as the formation of NiO. The as-obtained nickel oxide was further reacted with molten P_2O_5 to form $Ni_2P_4O_{12}$. All the weight loss further confirmed with the DTA signals. Hence, based on the above observation of TGA/DTA study, phosphorization process of nickel oxalate was carried out at 350 ºC for 12 h in ambient pressure in the air.

The PXRD pattern of the as-synthesized samples S1, S2, S3 and S4 obtained after thermal phosphorization matched with JCPDS no. 01-076-1557, which confirms the formation of pure monoclinic $Ni_2P_4O_{12}$ with C2/c space group (*Figure 3.5* and *Figure 3.7a*).

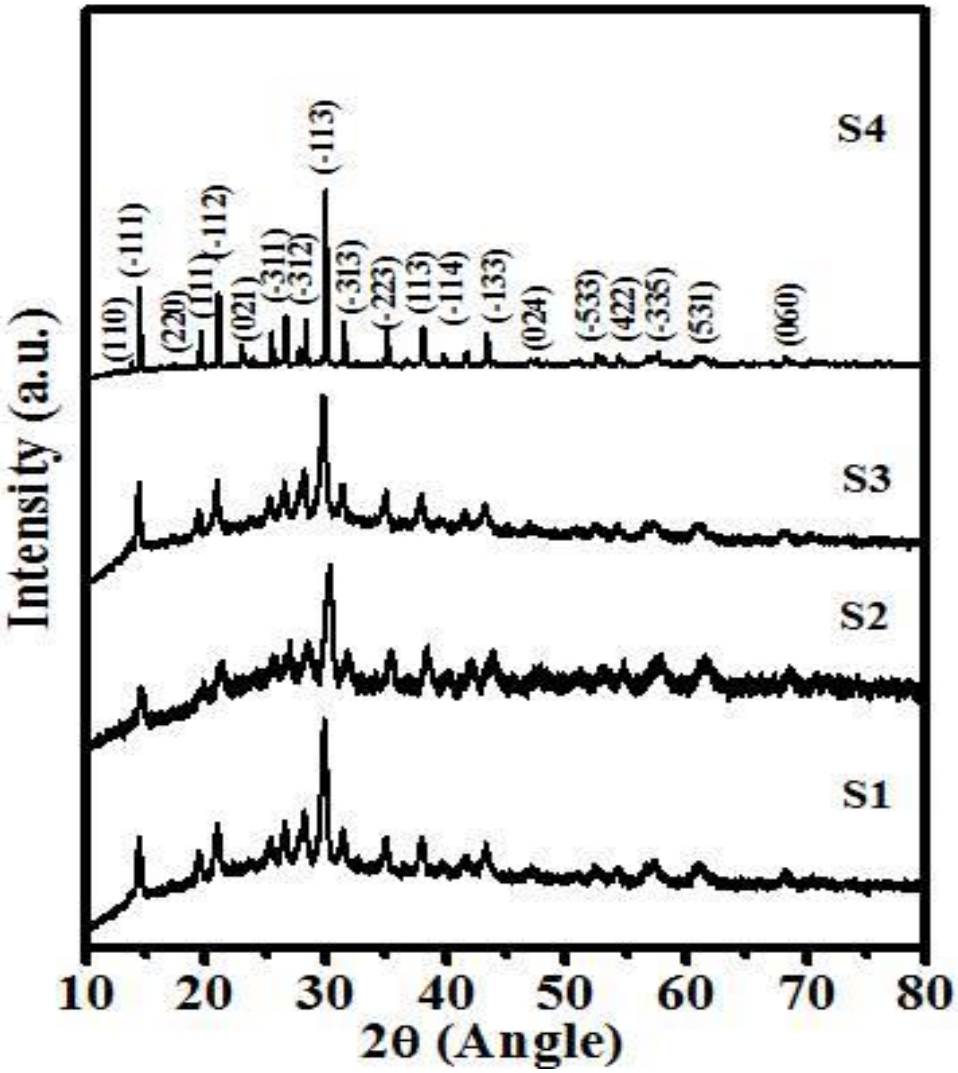

Figure 3.5. PXRD pattern of samples S1, S2, S3 and S4

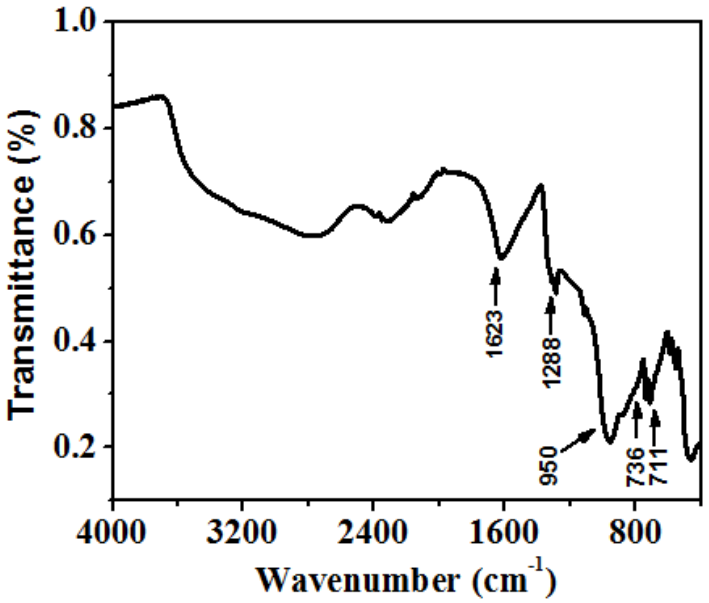

Figure 3.6. FTIR studies of sample S4

Further, the formation of $Ni_2P_4O_{12}$ was confirmed by the FTIR, which shows the formation of $P_4O_{12}^{4-}$ cyclic ring. FTIR spectra show a doublet around 730 cm^{-1} due to the formation of cyclophosphate ring of $(P_4O_{12})^{4-}$ (*Figure 3.6*). The cyclic ring of $P_4O_{12}^{4-}$ contains two types of bonds P-O-P and PO_2^{2-}. PO_2^{2-} radical shows an asymmetric and symmetric stretching frequency around 1340-1260 cm^{-1} and 1160-1060 cm^{-1}, respectively. The asymmetric and symmetric stretching frequencies of P-O-P bridge observe around 1020-870 cm^{-1} and 800-700 cm^{-1} respectively.[23] Morphological and compositional studies for $Ni_2P_4O_{12}$ have been done using SEM, TEM, STEM and EDAX studies. SEM image of sample S4 in *Figure 3.7b* shows the sheet like structure. Further, TEM studies have been done to get better insight about the size of the sheets of sample S4. *Figure 3.7c* shows the formation of $Ni_2P_4O_{12}$ nanosheets of diameter of 200-300 nm. The composition of the sheets has been analyzed by the EDAX studies, which indicates the presence of Ni, P and O (*Figure 3.7d*). High resolution Transmission electron microscopy (HRTEM) reveals distinct lattice fringes of the interplanar distance of 2.98 Å, which corresponds to (-113) plane of nickel cyclotetraphosphate (sample S4) (*Figure 3.7e-f*). Further, the elemental distribution in the $Ni_2P_4O_{12}$ nanosheets have been investigated by STEM-BF (bright field) energy-dispersive X-ray (EDAX) at 4 different points (*Figure 3.7g*). STEM-BF EDAX spectra (*Figure 3.7h*) indicates the presence of Ni, P and O at all the points in sample S4.

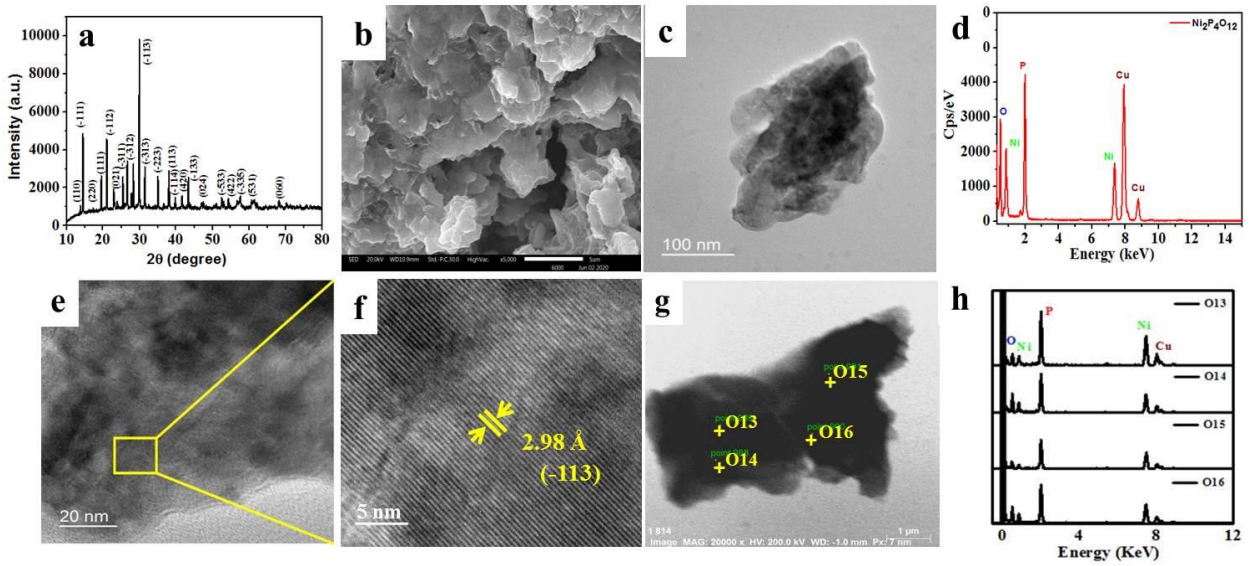

Figure 3.7. (a) PXRD, (b) SEM image, (c) TEM image, (d) EDAX spectra, (e-f) HRTEM image, (g) STEM-BF image and (h) EDAX multipoint spectra of sample S4

Similarly, the STEM-BF EDAX spectrum shows the presence of Ni, P and O at all the collected positions in samples S1, S2 and S3 (*Figure 3.8*).

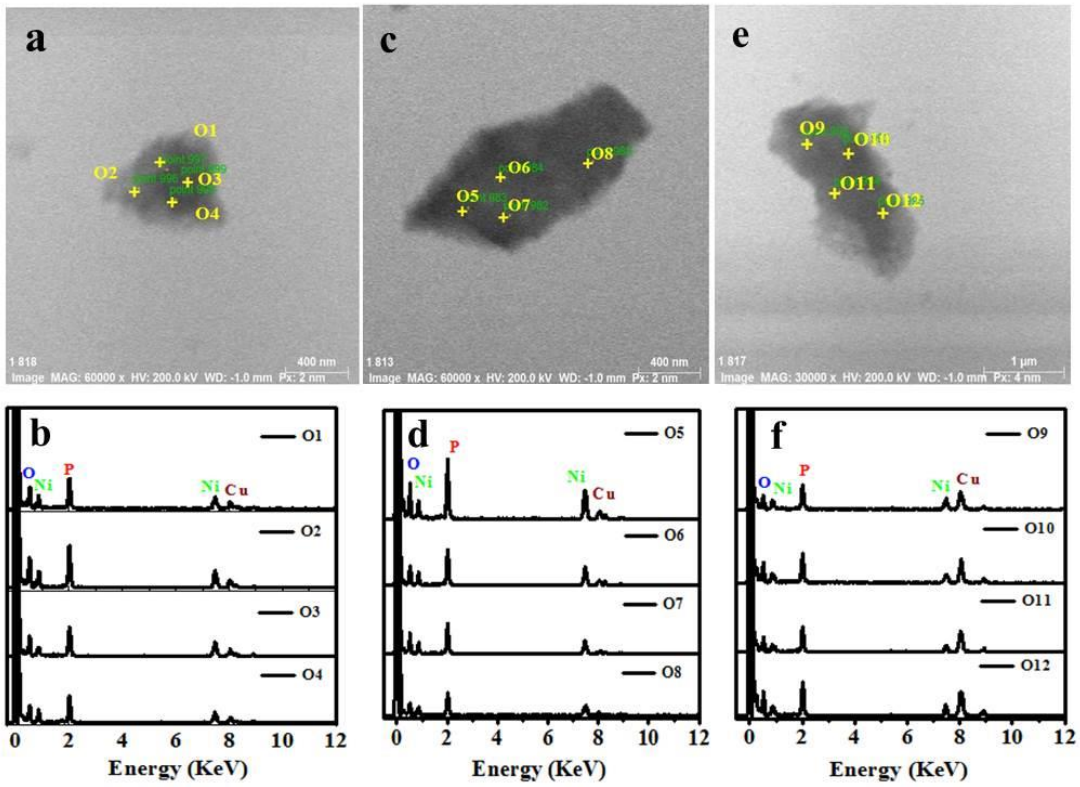

Figure 3.8. STEM image and their corresponding EDAX of sample (a-b) S1, (c-d) S2 and (e-f) S3

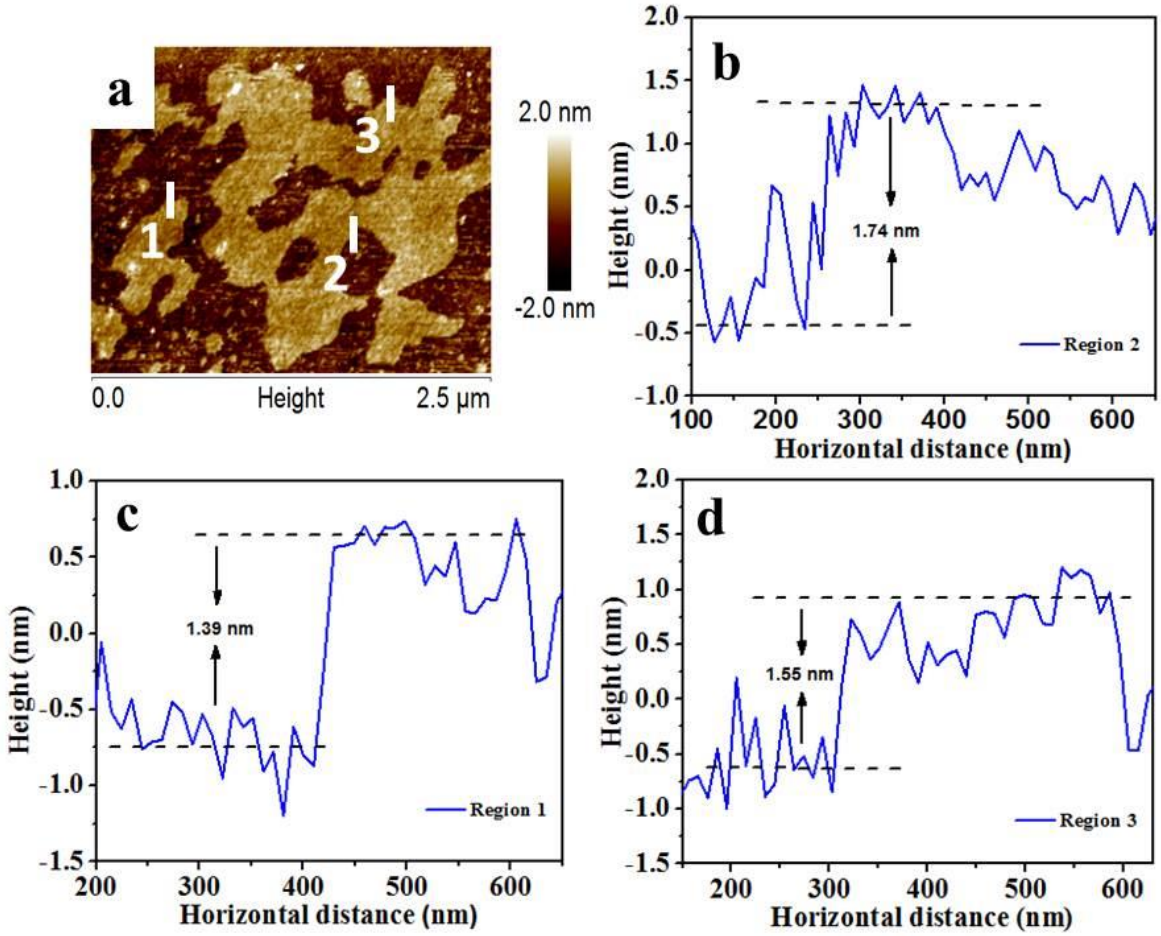

Figure 3.9. (a) AFM image of sample S4 and (b, c, d) the corresponding height profiles along the white line of region 1, 2, 3

To determine the thickness of nanosheets in sample S4 AFM studies has been carried out. The AFM study indicates that the average thickness of nanosheets is ~ 1.5 nm (*Figure 3.9a-d*).

3.3.1. Electrochemical characterization

The electrocatalytic properties of bare graphite, nickel oxalate and samples S1, S2, S3 and S4 were carried out in a three-electrode set up using linear sweep voltammetry (LSV), electrochemical impedance spectrometry (EIS) and chronoamperometry. LSV measurements for all the samples were done in the potential window of 0 to - 0.8 V vs RHE at a scan rate 10 mV/s.

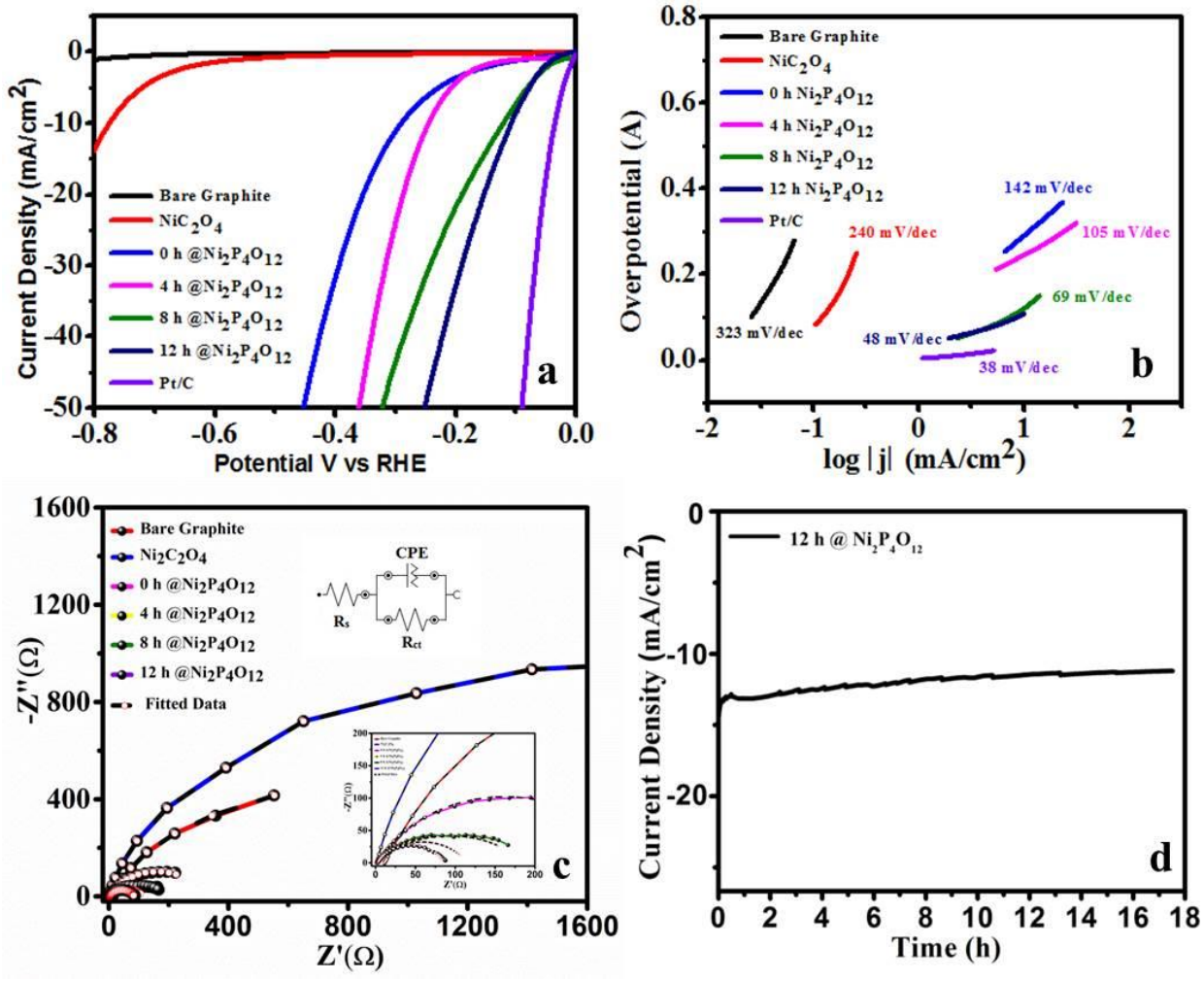

Figure 3.10. (a) Polaraization curves (b) Tafel slope (c) EIS studies of bare graphite, NiC_2O_4, samples S1, S2, S3, S4 and Pt/C (d) chronoamperometric studies of sample S4

Figure 3.10a shows the competitive LSV curves of Pt/C, bare graphite, NiC_2O_4, S1, S2, S3 and S4. The LSV study reveals that the onset potential of sample S4 is 37 mV and Pt/C shows almost zero onset potential for HER. The onset potential is defined as the potential to achieve the current density of 1 mA/cm^2. To evaluate the activity of the electrocatalysts towards HER a quantitative comparison of the overpotential to achieve a current density of 10 mA/cm^2 was done. The overpotential (η_{10}) required to achieve the current density of 10 mA/cm^2 for NiC_2O_4, S1, S2, S3, S4 and Pt/C are 774, 290, 244, 122, 105 and 36 mV respectively. It may be noted that graphite never reaches overpotential, thus shows negligible HER activity. Based on the overpotential values the catalytic activity towards HER follows the order S4>S3>S2>S1>NiC_2O_4. The low overpotential for S4 suggests the high efficiency

of prepared HER electrocatalyst. To compare our electrocatalyst with other Ni based electrocatalysts, a comparison table has been given as *Table 3.1*.

Table 3.1. Comparison table of nickel based electrocatalyst for hydrogen generation

S.No.	Electrocatalyst	Electrolyte	Overpotential (mV) η_{10}	Tafel slope ($mVdec^{-1}$)	References
1	$Ni_{12}P_5$/Ti	0.5 M H_2SO_4	107	63	[29]
2	Ni_5P_4 on Ni foil	0.5 M H_2SO_4	140	40	[30]
		1 M KOH	150	53	
3	Ni_5P_4 NC_s	0.5 M H_2SO_4	118	42	[31]
4	NiS/Ni foam	1 M KOH	125	83	[32]
5	NiSe-RGO-PI/ CNT film	0.5 M H_2SO_4	270	61	[33]
6	Ni_3P PHNs	0.5 M H_2SO_4	150	53	[34]
		1 M KOH	85	50	
7	Ni doped graphene	0.5 M H_2SO_4	180	45	[35]
8	Ni_3N/NF	0.5 M H_2SO_4	145	94	[36]
9	$Ni_2P_4O_{12}$ nanosheets	0.5 M H_2SO_4	131		[22]
10	$Ni_2P_4O_{12}$ Ultrathin nanosheets	0.5 M H_2SO_4	105	48	This work

To study the kinetics and the catalytic activity of as-prepared electrode material, Tafel slope was determined by fitting linear regions of Tafel plots into by equation $\eta = b \log j + x$. The tafel slope values of bare graphite, NiC_2O_4, S1, S2, S3, S4 and Pt/C are 323, 240, 142, 105, 69, 48 and 38 mV/dec respectively (*Figure 3.10b*). The tafel slope values follows the order NiC_2O_4>S1>S2>S3>S4. The small Tafel slope value for S4 suggests that sample S4 shows a high charge transfer kinetics which makes it a highly efficient electrocatalyst towards HER as compare to other synthesized electrocatalysts. Apart from this, bare graphite show very

high Tafel slope of 323 mV/ dec which confirms that there is no significant role of graphite in the electrocatalytic activity of $Ni_2P_4O_{12}$. To the best of our knowledge, there is only one report on nickel cyclotertaphosphate coated on carbon cloth. The synthesis of $Ni_2P_4O_{12}$ in the earlier report required complex steps including high-pressure reactor utilization which leads to the formation of thick sheets. However, in the present study, ambient pressure, as well as low temperature, have been used throughout the reaction which leads to the formation of ultrathin nanosheets having thickness ~1.5 nm which is nearly 60 times thinner than the previously reported $Ni_2P_4O_{12}$ nanosheets.[22] Due to the reduction in thickness of $Ni_2P_4O_{12}$ sheets, the considerable decreases in overpotential (105 mV) of sample S4 have been observed. The observed low over-potential are in good agreement with the earlier report of $Ni_2P_4O_{12}$ where Liu et al synthesized $Ni_2P_4O_{12}$ nanosheets of 120 nm which show an overpotential of 131.8 mV (η_{10}) with a Tafel slope of 47.8 mV/dec in 0.5 M H_2SO_4.[22] In the present study, the enhancement of the catalytic activity towards HER in acidic media can be explained as $Ni_2P_4O_{12}$ has the more nucleophilic character of Ni atoms which activates more catalytic sites and ultra-fine nanosheets (~1.5 nm) of $Ni_2P_4O_{12}$ promotes the catalytic activity towards HER in 0.5 M H_2SO_4.[22] Metal phosphate layered structure promotes conductivity and redox reaction of metals. To better understand the fundamental reaction kinetics of the electrocatalysts electrochemical impedance spectroscopy (EIS) was done at - 0.4 V vs Ag/AgCl in 0.5 M H_2 SO_4 solution. *Figure 3.10c* shows the Nyquist plot of all the prepared samples. The obtained EIS curve was fitted with Nova 1.1 software, which was inbuilt with Metrohm. The EIS data were fitted with a constant phase element (CPE) circuit model where CPE and charge transfer resistance (R_{ct}) are parallel to each other. The combination of CPE and Rct are in series combination with the solution resistance (R_s). All of these electrodes show small Rs values in range 3-9 Ω, suggesting the effective electrical interaction between the surface of electro-catalyst and electrolyte. From the *Figure 3.10c*, it was observed that the charge transfer resistance (Rct) of bare graphite, NiC_2O_4, S1, S2, S3 and S4 are 550, 1414, 222, 114, 98 and 87 Ω respectively. The low value of Rct indicates that in sample S4 there is faster electron transfer during the electrochemical reaction which is noticeably enhancing the HER activity in acidic solution. Thus, sample S4 shows very promising electrochemical properties (low overpotential and Tafel slope, small Rct), making it a potential alternative to non-noble-metal based HER catalyst in acid media. For a good catalyst, stability is a very

important parameter for practical application. Chronoamperometric studies of sample S4 were done at -0.4 V vs Ag/AgCl in 0.5M H_2SO_4 (*Figure 3.10d*). Current density vs time plot indicates that the current density remains constant up to 17 h. Therefore, based on above electrochemical studies, it can be concluded that a low overpotential, lower Tafel slope, high stability (17 h) of sample S4 makes it one of the efficient electrocatalyst for HER in highly acidic medium (0.5 M H_2SO_4). To calculate the active surface area, commonly electrochemical double-layer capacitance (C_{dl}) is used. The value of C_{dl} of $Ni_2P_4O_{12}$ was 3 mF/cm^2 (*Figure 3.11*).

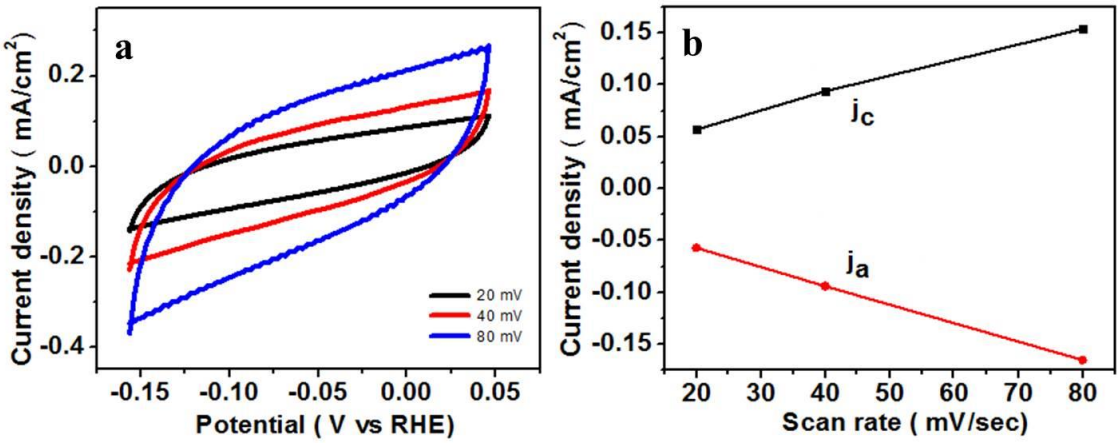

Figure 3.11. a) Cyclic voltammetry curve for C_{dl} measurement of sample S4; b) capacitive current at -0.05 V vs RHE at different scan rate for sample S4

To further, get insight into the high catalytic activity of sample S4, contact angle (CA) was done to describe the wettability properties of bare graphite and $Ni_2P_4O_{12}$ nanosheets (S4) coated on graphite. The contact angle of bare graphite and $Ni_2P_4O_{12}$ (S4) nanosheets were 92º and 67.3º respectively (*Figure 3.12.*). The low CA of $Ni_2P_4O_{12}$ nanosheets suggests more hydrophilic and aerophobic surface as compared to bare graphite which facilitates diffusion of electrolyte rapidly through the catalytic surface. Commonly, the activity of electrocatalyst is decreased due to the gas (H_2) produced on the surface which blocks the reaction solution and reduces the number of active sites by the repulsion of gas bubbles. The $Ni_2P_4O_{12}$ wettability properties make it more aerophobic and hydrophilic in nature that reduces the blocked area by repelling gas bubbles and helps in better interfacial charge transfer respectively.

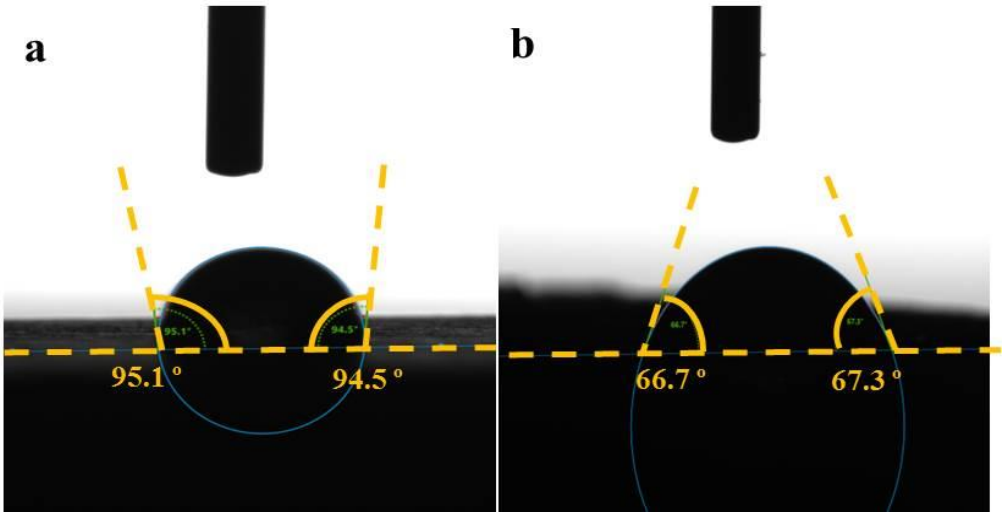

Figure 3.12. Contact angle studies of a) Bare graphite b) Sample S4

Post electrochemical study of the sample S4 has also been carried out by PXRD and shown in *Figure 3.13.* From PXRD pattern it is found that after chronoamperometry studies for 17 h, the phase of $Ni_2P_4O_{12}$ remains the same. Hence, based on the above discussion, it has been shown that $Ni_2P_4O_{12}$ nanosheets are one of the good electrocatalysts for hydrogen evolution reaction.

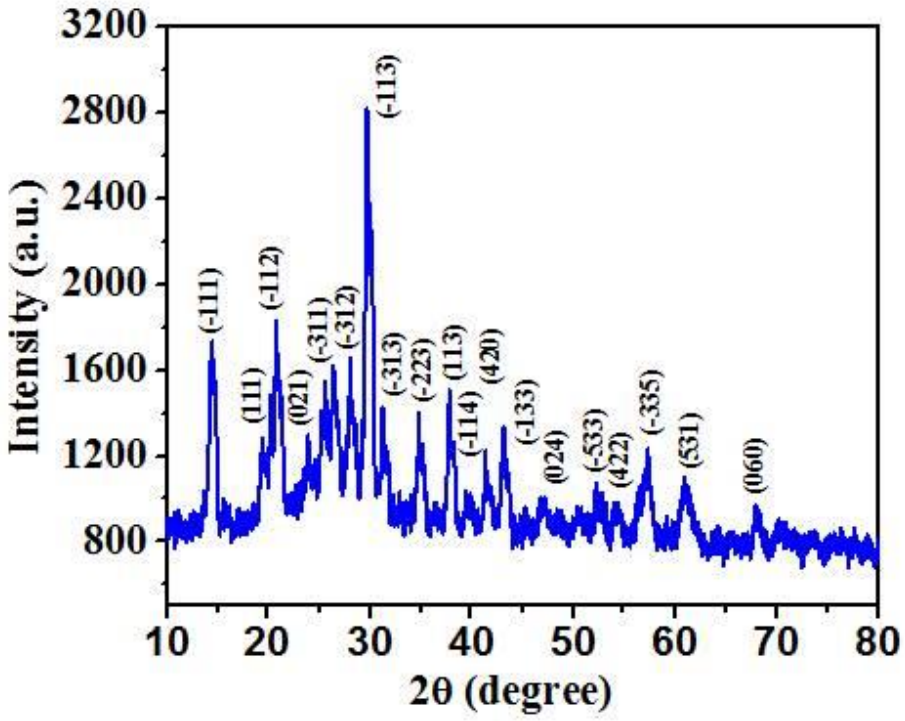

Figure 3.13. PXRD pattern after stability studies of sample S4

3.4. Conclusions

In the present chapter, we have successfully synthesized nickel cyclotetraphosphate ($Ni_2P_4O_{12}$) ultrathin nanosheets (~1.5 nm) using nickel oxalate sheets. The nickel cyclotetraphosphate nanosheets (sample S4) shows a very low overpotential of 105 mV to reach a current density of 10 mA/cm^2, having lower Tafel slope of 48 mV/dec and stability up to 17 h in an acidic media as compared to sample S1, S2 and S3 which makes it superior and efficient electrocatalyst towards HER. We believe that the above work would be of interest to the material scientists, chemists and environmentalist working in the field of energy-related application.

3.5. References

1. van Ruijven, B. J., De Cian, E. & Sue Wing, I. Amplification of future energy demand growth due to climate change. *Nat. Commun.* **10**, (2019).
2. Edwards, P. P., Kuznetsov, V. L., David, W. I. F. & Brandon, N. P. Hydrogen and fuel cells: Towards a sustainable energy future. *Energy Policy* **36**, 4356–4362 (2008).
3. Hanley, E. S., Deane, J. P. & Gallachóir, B. P. Ó. The role of hydrogen in low carbon energy futures–A review of existing perspectives. *Renewable and Sustainable Energy Reviews* **82**, 3027–3045 (2018).
4. Staffell, I. *et al.* The role of hydrogen and fuel cells in the global energy system. *Energy and Environmental Science* **12**, 463–491 (2019).
5. Rosen, M. A. & Koohi-Fayegh, S. The prospects for hydrogen as an energy carrier: an overview of hydrogen energy and hydrogen energy systems. *Energy, Ecology and Environment* **1**, 10–29 (2016).
6. Callejas, J. F. *et al.* Electrocatalytic and photocatalytic hydrogen production from acidic and neutral-pH aqueous solutions using iron phosphide nanoparticles. *ACS Nano* **8**, 11101–11107 (2014).
7. Suliman, M. H., Adam, A., Siddiqui, M. N., Yamani, Z. H. & Qamar, M. Facile synthesis of ultrathin interconnected carbon nanosheets as a robust support for small and uniformly-dispersed iron phosphide for the hydrogen evolution reaction. *Carbon N. Y.* **144**, 764–771 (2019).
8. Perera, F. Pollution from fossil-fuel combustion is the leading environmental threat to global pediatric health and equity: Solutions exist. *International Journal of*

Environmental Research and Public Health **15**, (2018).

9. De Levie, R. The electrolysis of water. *J. Electroanal. Chem.* **476**, 92–93 (1999).
10. Ding, T. *et al.* A highly active and durable CuPdPt/C electrocatalyst for an efficient hydrogen evolution reaction. *J. Mater. Chem. A* **4**, 15309–15315 (2016).
11. Zhang, J. *et al.* Facile one-step synthesis of phosphorus-doped CoS_2 as efficient electrocatalyst for hydrogen evolution reaction. *Electrochim. Acta* **259**, 955–961 (2018).
12. Zhang, J., Liu, S., Liang, H., Dong, R. & Feng, X. Hierarchical Transition-Metal Dichalcogenide Nanosheets for Enhanced Electrocatalytic Hydrogen Evolution. *Adv. Mater.* **27**, 7426–7431 (2015).
13. Esposito, D. V., Hunt, S. T., Kimmel, Y. C. & Chen, J. G. A new class of electrocatalysts for hydrogen production from water electrolysis: Metal monolayers supported on low-cost transition metal carbides. *J. Am. Chem. Soc.* **134**, 3025–3033 (2012).
14. Xing, Z., Li, Q., Wang, D., Yang, X. & Sun, X. Self-supported nickel nitride as an efficient high-performance three-dimensional cathode for the alkaline hydrogen evolution reaction. *Electrochim. Acta* **191**, 841–845 (2016).
15. Xiang, Q., Li, F., Zhang, D., Liao, Y. & Zhou, H. Plasma-based surface modification of g-C_3N_4 nanosheets for highly efficient photocatalytic hydrogen evolution. *Appl. Surf. Sci.* **495**, 143520 (2019).
16. Wu, C., Yang, Y., Dong, D., Zhang, Y. & Li, J. In Situ Coupling of CoP Polyhedrons and Carbon Nanotubes as Highly Efficient Hydrogen Evolution Reaction Electrocatalyst. *Small* **13**, (2017).
17. Wu, Z. *et al.* Highly efficient and stable MoP-RGO nanoparticles as electrocatalysts for hydrogen evolution. *Electrochim. Acta* **232**, 254–261 (2017).
18. Li, Y. *et al.* Controllable fabrication of uniform ruthenium phosphide nanocrystals for the hydrogen evolution reaction. *Chem. Commun.* **55**, 7828–7831 (2019).
19. Callejas, J. F., Read, C. G., Roske, C. W., Lewis, N. S. & Schaak, R. E. Synthesis, Characterization, and Properties of Metal Phosphide Catalysts for the Hydrogen-Evolution Reaction. *Chem. Mater.* **28**, 6017–6044 (2016).
20. Kucernak, A. R. J. & Naranammalpuram Sundaram, V. N. Nickel phosphide: The

effect of phosphorus content on hydrogen evolution activity and corrosion resistance in acidic medium. *J. Mater. Chem. A* **2**, 17435–17445 (2014).

21. Lv, C., Xu, S., Yang, Q., Huang, Z. & Zhang, C. Promoting electrocatalytic activity of cobalt cyclotetraphosphate in full water splitting by titanium-oxide-accelerated surface reconstruction. *J. Mater. Chem. A* **7**, 12457–12467 (2019).
22. Liu, X. *et al.* A porous nickel cyclotetraphosphate nanosheet as a new acid-stable electrocatalyst for efficient hydrogen evolution. *Nanoscale* **10**, 9856–9861 (2018).
23. Boonchom, B. & Vittayakorn, N. A rapid synthesis of cobalt cyclotetraphosphate Co2P 4O12 at low temperature. in *Ceramics International* **39**, (2013).
24. Yadav, K. K. *et al.* Synthesis of zirconium diboride and its application in the protection of stainless steel surface in harsh environment. *J. Solid State Electrochem.* **23**, 3243-3253 (2019).
25. McCrory, C. C. L. *et al.* Benchmarking Hydrogen Evolving Reaction and Oxygen Evolving Reaction Electrocatalysts for Solar Water Splitting Devices. *J. Am. Chem. Soc.* **137**, 4347–4357 (2015).
26. Rakshit, S. *et al.* Morphology control of nickel oxalate by soft chemistry and conversion to nickel oxide for application in photocatalysis. *RSC Adv.* **3**, 6106–6116 (2013).
27. Vaidya, S. *et al.* Nanospheres, nanocubes, and nanorods of nickel oxalate: Control of shape and size by surfactant and solvent. *J. Phys. Chem. C* **112**, 12610–12615 (2008).
28. Małecka, B. *et al.* Some aspects of thermal decomposition of $NiC_2O_4 \cdot 2H_2O$. *Thermochim. Acta* **466**, 57–62 (2007).
29. Huang, Z. *et al.* $Ni_{12}P_5$ nanoparticles as an efficient catalyst for hydrogen generation via electrolysis and photoelectrolysis. *ACS Nano* **8**, 8121–8129 (2014).
30. Ledendecker, M. *et al.* The Synthesis of Nanostructured Ni_5P_4 Films and their Use as a Non-Noble Bifunctional Electrocatalyst for Full Water Splitting. *Angew. Chemie - Int. Ed.* **54**, 12361–12365 (2015).
31. Pan, Y. *et al.* Monodispersed nickel phosphide nanocrystals with different phases: Synthesis, characterization and electrocatalytic properties for hydrogen evolution. *J. Mater. Chem. A* **3**, 1656–1665 (2015).
32. Zhu, W. *et al.* Nickel sulfide microsphere film on Ni foam as an efficient bifunctional

electrocatalyst for overall water splitting. *Chem. Commun.* **52**, 1486–1489 (2016).

33. Wang, T. *et al.* Reduced graphene oxide-polyimide/carbon nanotube film decorated with NiSe nanoparticles for electrocatalytic hydrogen evolution reactions. *Electrochim. Acta* **243**, 291–298 (2017).
34. Jin, L. *et al.* Phase separation synthesis of trinickel monophosphide porous hollow nanospheres for efficient hydrogen evolution. *J. Mater. Chem. A* **4**, 10925–10932 (2016).
35. Qiu, H.J. *et al.* Nanoporous Graphene with Single-Atom Nickel Dopants: An Efficient and Stable Catalyst for Electrochemical Hydrogen Production. *Angew. Chemie* **127**, 14237–14241 (2015).
36. Xing, Z., Wang, D., Li, Q., Asiri, A. M. & Sun, X. Self-standing Ni-WN heterostructure nanowires array: A highly efficient catalytic cathode for hydrogen evolution reaction in alkaline solution. *Electrochim. Acta* **210**, 729–733 (2016).

Chapter 4

Promoting the catalytic activity of metal cyclotetraphosphate towards electrochemical hydrogen generation

4.1. Introduction

The adverse change in climate and increasing global demand of energy has led scientists all over the world to find a green, economical, sustainable and carbon-neutral source of energy.[1] The depletion of non-renewable resources of energy and increased emission of green-house gases has further forced the scientist to pursue an alternative source of energy.[2] Electrochemical hydrogen production from water electrolysis has been regarded as one of the clean and effective method to replace conventional fossil fuels. The high gravimetric energy density of hydrogen makes it a potent energy carrier to meet the future energy demands.[1] However, to achieve reasonable electricity-fuel conversion efficiency and high current density at low overpotential electrocatalysts are required during the hydrogen evolution reaction (HER). Till date, noble metal based electrocatalyst such as platinum has been regarded as the best electrocatalyst for HER, but their practical application is limited because of their high cost and scarcity. Thus, in order to boost the hydrogen economy highly efficient non-noble metal-based catalyst with comparable activity to the precious metal-based catalyst has been the focus of research in the recent years. Transition metal-based catalysts such as chalcogenides[3,4], nitrides, phosphides and selenides[5] with varied structures shows good catalytic activity for HER. Among these catalysts, transition metal-based phosphides having metalloid characteristic have been widely used as electrocatalysts in acidic media. The activity of these materials has further been increased by the introduction of oxygen which enhanced the intrinsic conductivity and also activated the catalytic sites as a result of elongation of M-P bond.[6] As a result of their enhanced catalytic activity and special structure, extensive attention has been drawn towards transition metal phosphates (TMPs). Transition metal phosphates are a promising material to be used as electrocatalyst due to their non-toxicity, good conductivity, cost-effectiveness, stability and high conductivity as a result of their open framework structure.[7] The phosphate group not only favors the water oxidation and adsorption facility due to induction of distorted local metal geometry but also act as proton acceptors as a result facilitating the oxidation of metal atoms.[8,9] The phosphates are chemically very stable due to the presence of strong covalent bond between P and O atoms.[10] The contact between the electrolyte and electrocatalyst surface is very high in TMPs due to their excellent surface wettability properties.[6] Due to their superior electrochemical properties, TMPs have been widely utilized in various applications such as water oxidation,

supercapacitors etc. Recently, metaphosphates having the aforementioned characteristics of the phosphate group have been utilized for the water splitting application, mainly oxygen evolution reaction (OER). Xiong et al. has reported $Ni_2P_4O_{12}$ as an efficient catalyst for the OER in basic medium.[9] Our group has earlier synthesized $Co_2P_4O_{12}$ and $Ni_2P_4O_{12}$ by simple phosphorization of their respective oxalates and utilized them as an efficient electrocatalyst for the HER.[11,12] Efforts have also been made to further improve the catalytic activity of the monometallic phosphates by the synthesis of bimetallic phosphates. Xu and coworkers have synthesized CoNi-ZIF composite as a robust catalyst for OER.[13] The combinations of metals not only offer better efficiency than their monometallic phosphates but are also cost-effective. The richer redox activity of both nickel and cobalt as a result of combined effect can result in the better electrochemical activity.[14]

There are several reports on the enhancement of catalytic activity of cyclotetraphosphates after tagging them with other metal oxides and heteroatoms or employing strategies such as surface engineering, morphology change or introducing defects.[8] If the nanostructures are efficiently tailored and structured then their activity can be enhanced. To this end, if we use materials having large surface area, high conductivity, high porosity, fast ionic and charge transport and high number of active sites then the activity of the electrocatalysts can be greatly enhanced.[1] Graphene is one such sparkling carbonaceous material which has received enormous attention due to its higher chemical and physical merits such as high stability, high conductivity and large surface area.[14,15] Due to structural stability and porosity of graphene it is a desirable conductive substrate to be incorporated with cobalt nickel cyclotetraphosphate nanoparticles to enhance their catalytic performance for the HER. Though bimetallic metaphosphates with the MOFs have been explored as the OER catalyst but there is no report for the utilization of $CoNiP_4O_{12}$/rGO as an electrocatalyst for HER application.

In the present work, cobalt nickel cyclotetraphosphate ($CoNiP_4O_{12}$) has been synthesized by the phosphorization of the cobalt nickel oxalate cubic particles using P_2O_5 as the phosphorous source. The cobalt nickel oxalate nanoparticles have been synthesized via the micellar route at room temperature. The composite of cobalt nickel cyclotetraphosphate/ reduced graphene oxide ($CoNiP_4O_{12}$/rGO) has been synthesized by adding graphene along with P_2O_5 and grinding the mixture before calcining it at 350 ℃ for 6 h. The resulting

composite show excellent catalytic activity towards HER with an overpotential of 41 mV at 10 mA/cm^2 current density.

4.2. Experimental

4.2.1. Material and methods

Nickel nitrate hexahydrate ($Ni(NO_3)_2.6H_2O$, 98 %, Merck, India), di-ammonium oxalate ($(NH_4)_2C_2O_4$, 99 %, Merck, India), di-phosphorus pentaoxide (P_2O_5, 95 %, CDH, India), Platinum/carbon (20 wt % of Pt/C, Sigma Aldrich, India), Cetyl tri-methyl ammonium bromide (CTAB, 99 %, CDH, India) and methanol (CH_3OH, 98 %, CDH, India) have been used as starting material. All the chemicals were used without any purification.

Synthesis of Cobalt nickel oxalate

To synthesize Cobalt nickel oxalate ($CoNiC_2O_4$), first we have prepared 0.1 M solution of cobalt nitrate and nickel nitrate. After that 1 wt % of CTAB was added in the solution and stirred for 1 h. 0.1 M solution of ammonium oxalate was also prepared with 1 wt % of CTAB in the solution and stirred till complete dissolution of CTAB. Then both the solutions were mixed together and stirred for 12 h. Precipitates were separated from the solution and thoroughly washed with the mixture of methanol and chloroform (1:1). Precipitates were dried in oven at 65 ºC.

Synthesis of $CoNiP_4O_{12}$ and $CoNiP_4O_{12}$/rGO

For the synthesis of $CoNiP_4O_{12}$, $CoNiC_2O_4$ and P_2O_5 were taken in same weight ratio in a mortar pestle and grinded together to form a homogenous mixture. This homogeneous mixture was further transferred into the crystalline alumina crucible and calcined at 350 ºC for 6 h with heating rate of 2 ºC/min. Similarly, synthesis of $CoNiP_4O_{12}$/rGO was done. The precursors $CoNiC_2O_4$ and P_2O_5 were taken in same weight ratio; with that 10 mg of graphene oxide was also added in a mortar pestle and grinded together to form a homogenous mixture. This mixture was calcined at 350 ºC for 6 h.

4.2.2. Characterization

Powder X-ray diffraction of all the samples was carried out using Bruker D8 advance diffractometer with Cu-Kα (λ= 1.54Å) radiation. Morphological studies were examined by Scanning electron microscope (SEM, JEOL, JSM-IT30) and Transmission electron

microscope (TEM, JEOL JEM-2100) coupled with energy-dispersive X-ray spectroscopy (EDS) analyzer. FTIR studies were carried out on Bruker, vertex 70. Electrochemical measurements were performed on Metrohm PGSTAT-30 Autolab workstation. Drop shape analyser DSA25-KRUSS GmbH was used to determine the contact angle by sessile drop method.

4.2.3. Preparation of working electrodes

First the dispersion of $CoNiP_4O_{12}$/rGO was prepared by taking 5 mg of sample in 100 µl of ethylene glycol and 300 µl of ethanol and sonicated for 60 minutes. Further, 20 µl of Nafion (binder) was added to the above solution and sonicated for another 15 min. The as-prepared dispersion (60 µl) was drop cast on a graphite substrate and dried in the oven at 60 ºC in air. Similarly, the working electrodes had been prepared for all the materials. To compare our result with state of art material Pt/C (5% Pt on carbon) electrode was also prepared.

4.2.4. Electrochemical measurements

All electrochemical measurements were performed using Metrohm PGSTAT-30 Autolab workstation with a graphite rod, $CoNiP_4O_{12}$/graphite substrate and 3 M Ag/AgCl were used as a counter, working and reference electrode, respectively. All the electrochemical studies were conducted at room temperature in 0.5 M H_2SO_4 electrolyte. Linear Sweep Voltammetry (LSV) was done in the potential range (0 V to - 0.8 V) vs RHE at a scan rate of 10 mV/sec. The Tafel slope was calculated using equation $\eta = b \log j + x$, where η is the over-potential, j is the current density, b is the Tafel slope, and x is the intercept corresponding to the exchange current density. Electrochemical impedance spectroscopy (EIS) measurements were performed at – 0.05 mV vs RHE in the frequency range 0.01 Hz to 100 kHz with amplitude of 10 mV. All potentials measured in Ag/AgCl and converted to reversible hydrogen electrode (RHE) using the Nernst equation.

4.3. Result and discussion

In the present chapter, we have synthesized bimetallic cyclotetraphosphate ($CoNiP_4O_{12}$) and its composite with that of reduced graphene oxide ($CoNiP_4O_{12}$/rGO) to increase the catalytic activity of bimetallic cyclotetraphopshate towards HER. To synthesize cobalt nickel cyclotetraphopshate, first cobalt nickel oxalate was synthesized using micellar route as

discussed in experimental section. To confirm the formation of $CoNiC_2O_4$ PXRD of the as-synthesized sample has been carried out, which shows the presence of both CoC_2O_4 (JCPDS no. 00-025-250) and NiC_2O_4 (JCPDS no. 00-014-742) of orthorhombic phase with space group Cccm as depicted in *Figure 4.1a*. Further the morphology of the $CoNiC_2O_4$ has been investigated by scanning electron microscope (SEM). The SEM micrograph shows the formation of cubical shape particles of size ~3-4 µm as shown in the *Figure 4.1b*. The as prepared $CoNiC_2O_4$ was further used for the synthesis of $CoNiP_4O_{12}$ and $CoNiP_4O_{12}$/rGO.

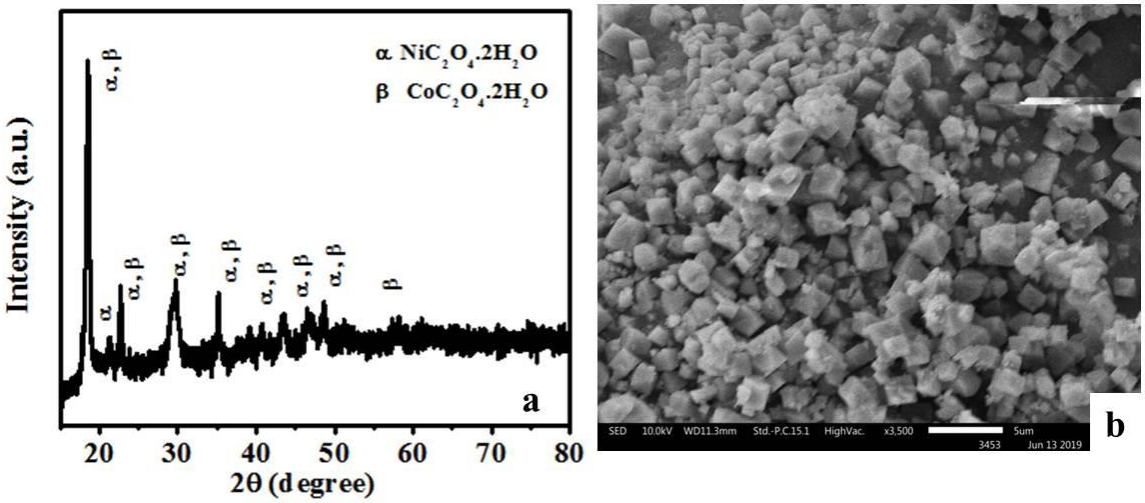

Figure 4.1. a) PXRD diffraction pattern and SEM image of $CoNiC_2O_4$

To synthesize $CoNiP_4O_{12}$ and $CoNiP_4O_{12}$/rGO, the phosphorization of $CoNiC_2O_4$ was done at 350 ºC. PXRD analysis was carried out for the as-synthesized $CoNiP_4O_{12}$ sample which shows the formation of monoclinic phase of $CoNiP_4O_{12}$. The 2θ value at 13.7, 14.4, 19.4, 20.9, 25.2, 26.4, 28.1, 29.8, 31.3, 34.8, 37.8, 39.6, 43.2, 47.3, 52.2, 57.3, 61.3 and 67.9 corresponds to 110, -111, 111, -112, -311, -312, 310, 022, -313, 400, -422, -114, -113, -315, -531, -111, 531 and 135 planes respectively as depicted in *Figure 4.2a*. FTIR analysis was carried out to confirm the formation of monoclinic phase of $CoNiP_4O_{12}$ and the presence of cyclic ring $P_4O_{12}^{4-}$ ring as shown in *Figure 4.2b*. FTIR peaks around 1340-1260 and 1160-1060 cm^{-1} arises due to the symmetric and asymmetric stretching of PO_2^{2-} radical. The P-O-P bond show stretching frequencies around 1020-870 cm^{-1} and 800-700 cm^{-1} but the main characteristic peak of $P_4O_{12}^{4-}$ ring is obtained at around 730 cm^{-1} which confirms the formation of cyclic ring in $CoNiP_4O_{12}$.[16] Further the morphological, compositional and chemical state of elements was analysed using TEM and XPS. TEM micrograph shows the

formation of particles of size ~ 10 nm and TEM -EDX confirms the presence of all the elements in the sample as shown in *Figure 4.2c* and *Figure 4.2d*. Further the confirmation of all elements and their chemical state was analyzed by XPS. The peaks at 782.6 and 798.6 eV in high-resolution Co 2p spectra (*Figure 4.3a*) correspond to the Co^{2+} species $2p_{3/2}$ and $2p_{1/2}$ in $CoNiP_4O_{12}$, while the peaks at 786.2 and 803.8 eV are satellite peaks. The peaks in the high-resolution spectra (*Figure 4.3b*) of Ni 2p appear at eV values of 854.1, 857.1, 860, 874.8, and 882.4. Peaks at 757.1 and 874.8 eV correspond to Ni $2p_{3/2}$ and Ni $2p_{1/2}$ Ni^{2+} binding energies, respectively. The peaks at 860.9 and 881.4 eV are $CoNiP_4O_{12}$ satellite peaks. In P 2p high resolution spectra (*Figure 4.3c*), the peak at 134.5 eV corresponds to metal phosphate species. The O 1s spectra (*Figure 4.3d*) shows two peaks at 534.6 and 533.2 eV attribute to M-P-O species and adsorbed water respectively.

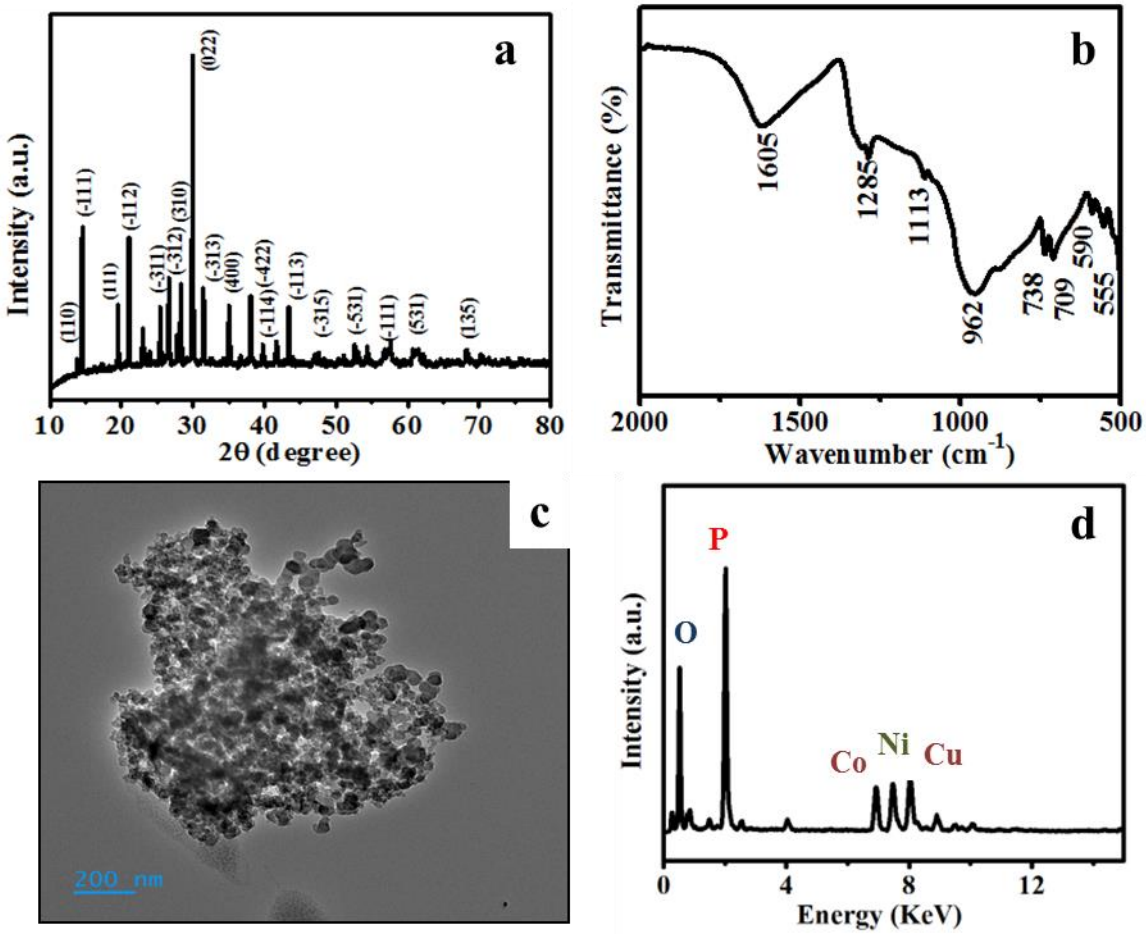

Figure 4.2. a) X-ray diffraction pattern b) FTIR spectra c) TEM image and d) TEM-EDAX of $CoNiP_4O_{12}$

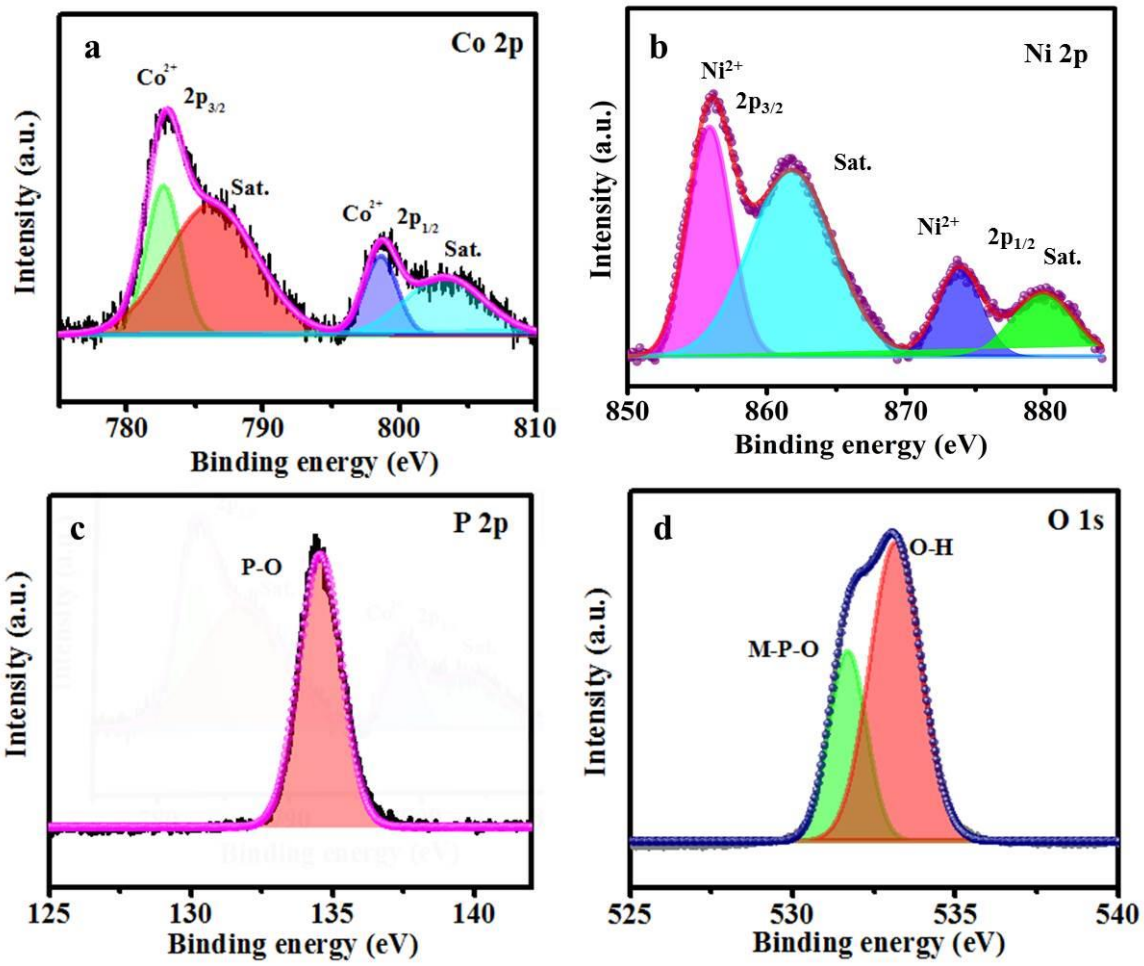

Figure 4. 3. High resolution spectra of $CoNiP_4O_{12}$ a) Co 2p b) Ni 2p c) P 2p and d) O 1s

Similarly, $CoNiP_4O_{12}$/rGO was synthesized by the phosphorization of $CoNiC_2O_4$ along with the addition of rGO. PXRD analysis shows the formation of monoclinic phase of $CoNiP_4O_{12}$ with the corresponding planes as shown in *Figure 4.4a*. To confirm the formation of cylotetraphosphate in the composite, FTIR analyses was carried out on as-synthesized sample as shown in *Figure 4.4b*. The FTIR spectrum shows the symmetric and asymmetric stretching of Po_2^{2-} radical at around 1340-1260 and 1160-1060 cm^{-1} respectively. The characteristic peak of the $P_4O_{12}^{4-}$ ring at 730 cm^{-1} confirms the presence of the cyclic ring in the composite. To confirm the presence of reduced graphene oxide in the composite Raman spectroscopy of the synthesized samples has been carried out. The Raman spectrum of $CoNiP_4O_{12}$ shows no characteristic peak. The Raman spectrum of $CoNiP_4O_{12}$/rGO (*Figure 4.4c*) shows two peaks around 1343 and 1583 cm^{-1} which corresponds to D and G band of carbon [17]. After the successful synthesis of the composite, the morphological studies of

$CoNiP_4O_{12}$/rGO were carried out using transmission electron microscope (TEM). The TEM micrograph shows the formation of nanoparticles of size ~6 nm which are uniformly distributed over rGO (*Figure 4.5a-b*). Further to check the elemental composition TEM-EDAX has been carried out that shows the presence of Co, Ni, P and O the elements in the sample in *Figure 4.5c*. FESEM was performed for elemental mapping to check the uniform distribution of Co, Ni, P, C and O in the material as depicted in *Figure 4.6.*

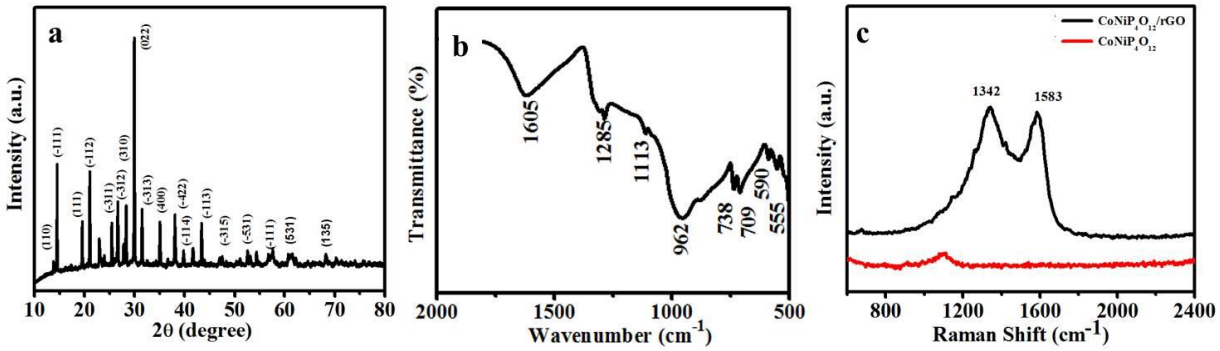

Figure 4.4. a) X-ray diffraction pattern b) FTIR spectra and c) Raman spectra of $CoNiP_4O_{12}$/rGO

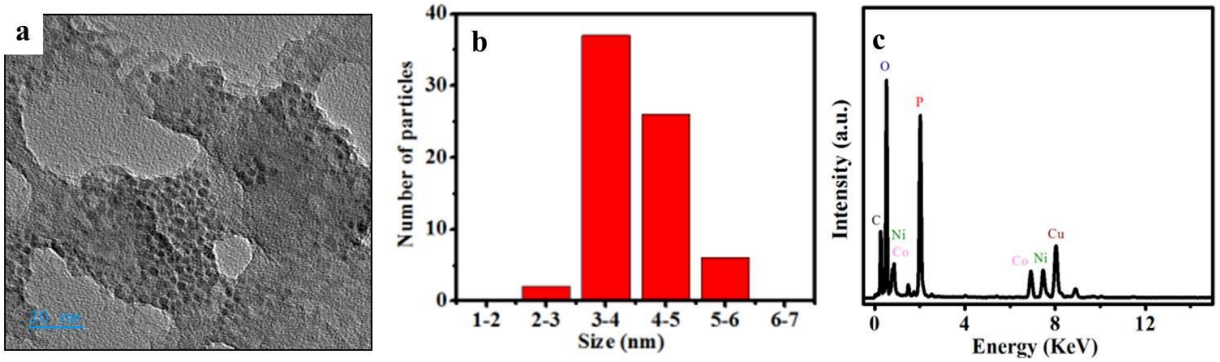

Figure 4.5. a) TEM image b) size distribution of nanoparticles and c) elemental composition of $CoNiP_4O_{12}$/rGO

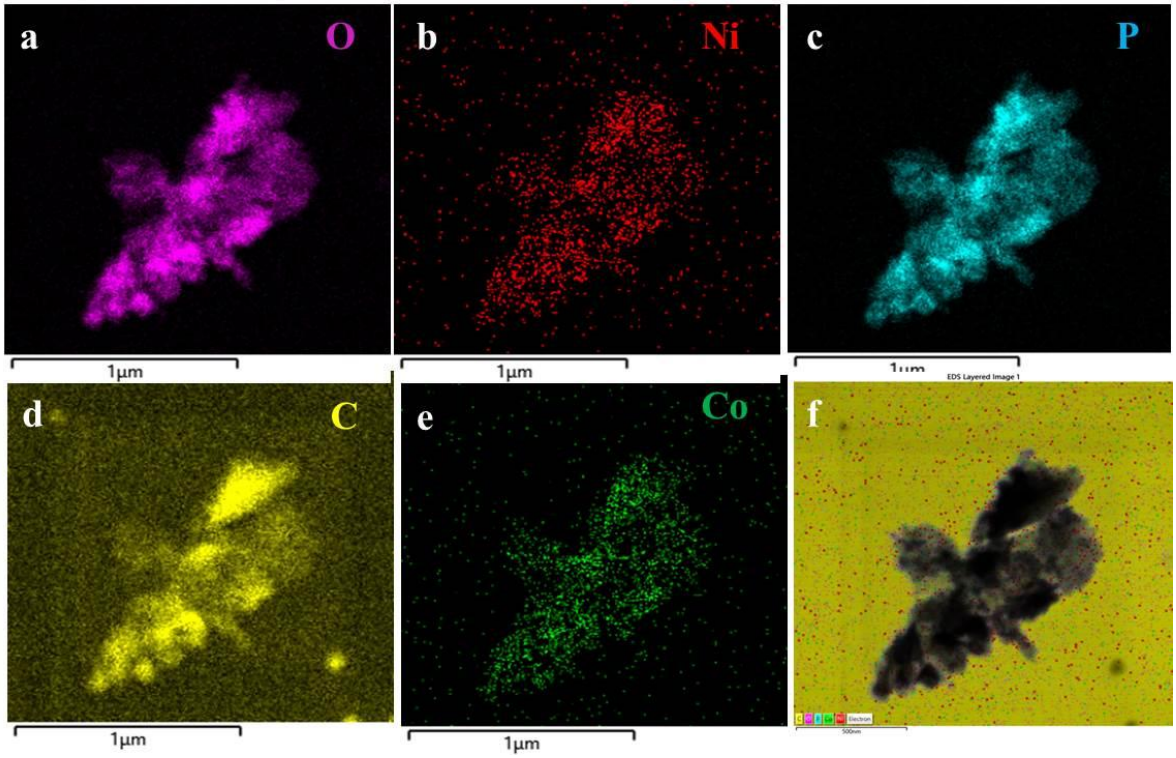

Figure 4.6. FESEM elemental mapping of $CoNiP_4O_{12}$/rGO

Further, X-ray photoelectron spectroscopy (XPS) was used to analyse the chemical state and composition of the as-synthesized materials. The XPS survey scan shown in *Figure 4.7a* confirms the presence of Ni, Co, P and O elements in the material. Further high-resolution XPS studies were done. In high-resolution Co 2p spectra, the peak at 782.6, 798.6 eV corresponds to $2p_{3/2}$ and $2p_{1/2}$ of Co^{2+} species in $CoNiP_4O_{12}$/rGO whereas the peaks at 786.2 and 803.8 eV are the satellite peaks (*Figure. 4.7b*). In Ni 2p high resolution spectra, the peaks arise at 854.1, 857.1, 860, 874.8 and 882.4 eV. The peaks at 757.1 and 874.8 eV attributes to Ni $2p_{3/2}$ and Ni $2p_{1/2}$ of Ni^{2+} binding energies (*Figure. 4.7c*). The peaks at 860.9 and 881.4 eV attributes to the satellite peaks for $CoNiP_4O_{12}$/rGO. There is some positive shift in 2p peaks of Co and Ni in $CoNiP_4O_{12}$/rGO. This positive shift is due to the inductive effect of phosphate anion. The cyclic anion deform the crystal structure and intensely polarize O_2^{2-} due to presence of strong P-O bonds which produce more positive shift of Co 2p and Ni 2p peaks. [8,10] In P 2p high resolution spectra, the peak at 134.5 eV corresponds to metal phosphate species (*Figure 4.7d*). In C 1s spectrum the peaks at 284.8, 286.2 and 288.1 eV which corresponds to C-C, C-O and C=O respectively (*Figure 4.7e*). The O 1s spectra shows

two peaks at 53.6 and 533.2 eV attribute to M-P-O species and adsorbed water respectively (*Figure 4.7f*).

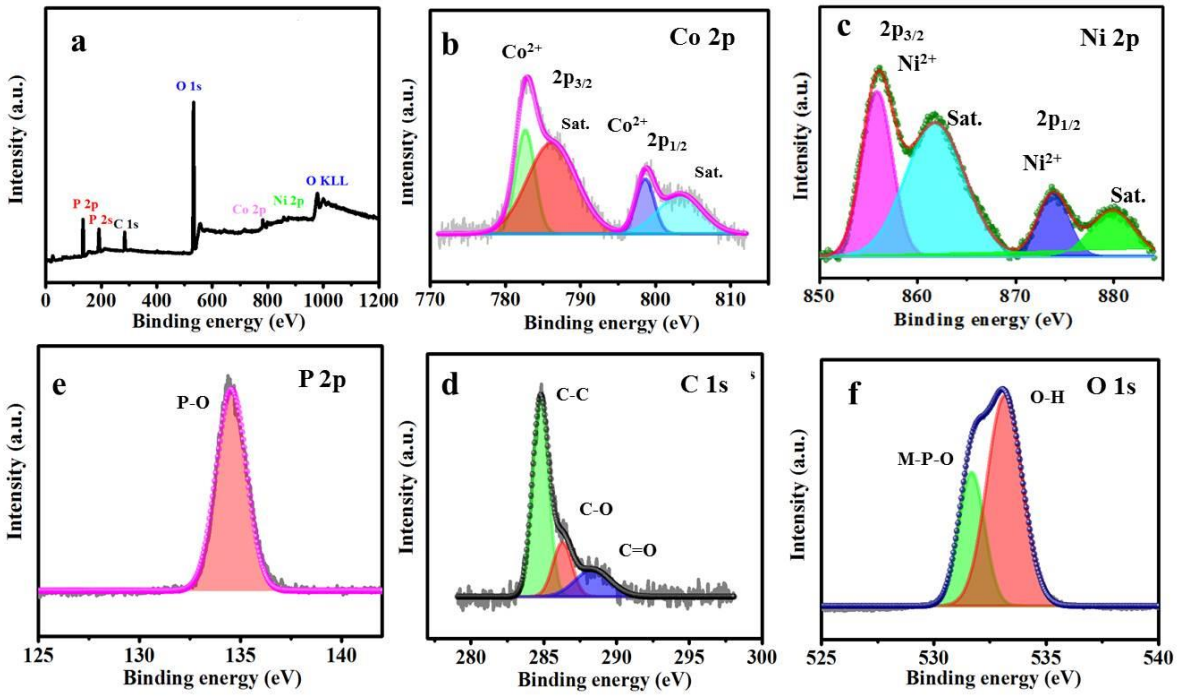

Figure 4.7. a) XPS survey spectra and high resolution spectra of $CoNiP_4O_{12}$ /rGO b) Co 2p c) Ni 2p d) P 2p e) C 1s and f) O 1s

4.3.1. Electrochemical studies

To investigate catalytic activity of all the materials at first linear sweep voltammetry was performed in 0.5 M H_2SO_4 as shown in *Figure 4.8a*. The LSV curve of the bare graphite which has been used as a substrate to prepare the working electrode shows very less activity and does not even reach 1 mA/cm^2 of current density thus indicating no contribution towards the activity for HER. The bimetallic cyclotetraphosphate $CoNiP_4O_{12}$ shows lower overpotential of 74 mV to reach the current density of 10 mA/cm^2 as compared to monometallic cyclotetraphopshate ($Co_2P_4O_{12}$ and $Ni_2P_4O_{12}$) which requires an overpotential of 92 mV and 105 mV in case of $Co_2P_4O_{12}$ and $Ni_2P_4O_{12}$ respectively. The bimetallic cyclotetraphosphate $CoNiP_4O_{12}$ requires less potential as compared to their single metal cyclotetraphopshate ($Co_2P_4O_{12}$ and $Ni_2P_4O_{12}$) due to the synergistic effect of both metals which promotes intrinsic electron transfer during the HER process. Further to enhance the activity of bimetallic cyclotetraphosphate ($CoNiP_4O_{12}$) its composite with that of reduced

graphene oxide has been synthesized. The $CoNiP_4O_{12}$/rGO requires an overpotential of 41 mV to reach benchmark of 10 mA/cm^2 current density. The $CoNiP_4O_{12}$/rGO shows lower overpotential than that of bimetallic cyclotetraphosphate ($CoNiP_4O_{12}$). The low overpotential of $CoNiP_4O_{12}$/rGO is attributed due to their high surface areas which helps in more diffusion of electrolyte and provide a greater number of active sites on the electrode surface. The activity of the composite has also been compared with the state of art material Pt/C for HER which requires and overpotential of 27_mV to reach the current density of 10 mA/cm^2. Further to check the kinetics of reaction Tafel plot were drawn from the linear parts of LSV curves as depicted in *Figure 4.8b*. The $CoNiP_4O_{12}$/rGO, $CoNiP_4O_{12}$, $Co_2P_4O_{12}$, $Ni_2P_4O_{12}$ and Pt/C shows the Tafel slope value of 43 mV/dec, 45 mV/dec, 97 mV/dec, 48 mV/dec and 38 mV/dec respectively. Bare graphite shows a Tafel slope value of 323 mV/dec indicating very slow kinetics towards HER. The small Tafel slope value of electrocatalyst suggests higher reaction kinetics rate towards the reaction. In here, $CoNiP_4O_{12}$/rGO shows smallest tafel slope value among other catalyst which is close to the state of art material Pt/C and thus it has highest reaction kinetics for HER process. The value of tafel slope suggests that reaction follows volmer-heyrosky mechanism.

The excellent catalytic activity of metal cyclotetraphophate is due to the nucleophilic effect of $P_4O_{12}^{4-}$ anionic ring which make metal more electron deficient. Therefore, $P_4O_{12}^{4-}$ ring can act as proton acceptor site during HER process. To gain further insights into the reaction taking place at the electrode surface EIS studies were carried out for all the materials at 0.05 V vs RHE as shown in *Figure 4.8c*. The software Nova 1.1, which came pre-installed with Metrohm, was used to fit the resultant EIS curve. Charge transfer resistance (R_{ct}) and a constant phase element (CPE) that was parallel to one another were used to match the EIS data. The solution resistance (R_s) is combined in series with the combinations of CPE and R_{ct}. The Nyquist plot shows the R_{ct} value of 1.5 ohm, 18 ohm 137 ohm and 198 ohm for $CoNiP_4O_{12}$/rGO, $CoNiP_4O_{12}$, $Co_2P_4O_{12}$ and $Ni_2P_4O_{12}$ respectively. The low R_{ct} value of $CoNiP_4O_{12}$/rGO designates that faster electron transfer takes place during the electrochemical process. Therefore, low overpotential, small Tafel slope value and low charge transfer resistance of $CoNiP_4O_{12}$/rGO make it a potential candidate among non-noble electrocatalyst for HER in acidic medium. But for practical application, the durability of the catalyst is an important criterion. To check the durability of the catalyst in acidic medium

chronoamperometric studies were done at overpotential of 0.06 V vs RHE as shown in *Figure 4.8d*. The current density is almost stable up to 24 h with a current retention of 90 %. Further to check the stability of catalyst ICP-MS studies of electrolyte were carried out after chronoamperometric studies. The concentration of Co and Ni is around 10ug/L and 15ug/L respectively that shows the good stability of the catalyst in acidic medium.

The HER activity of the bimetallic cyclotetraphosphate and its composite with rGO has been compared with the other transition metal based catalyst and have been listed in *Table 4.1*.

.

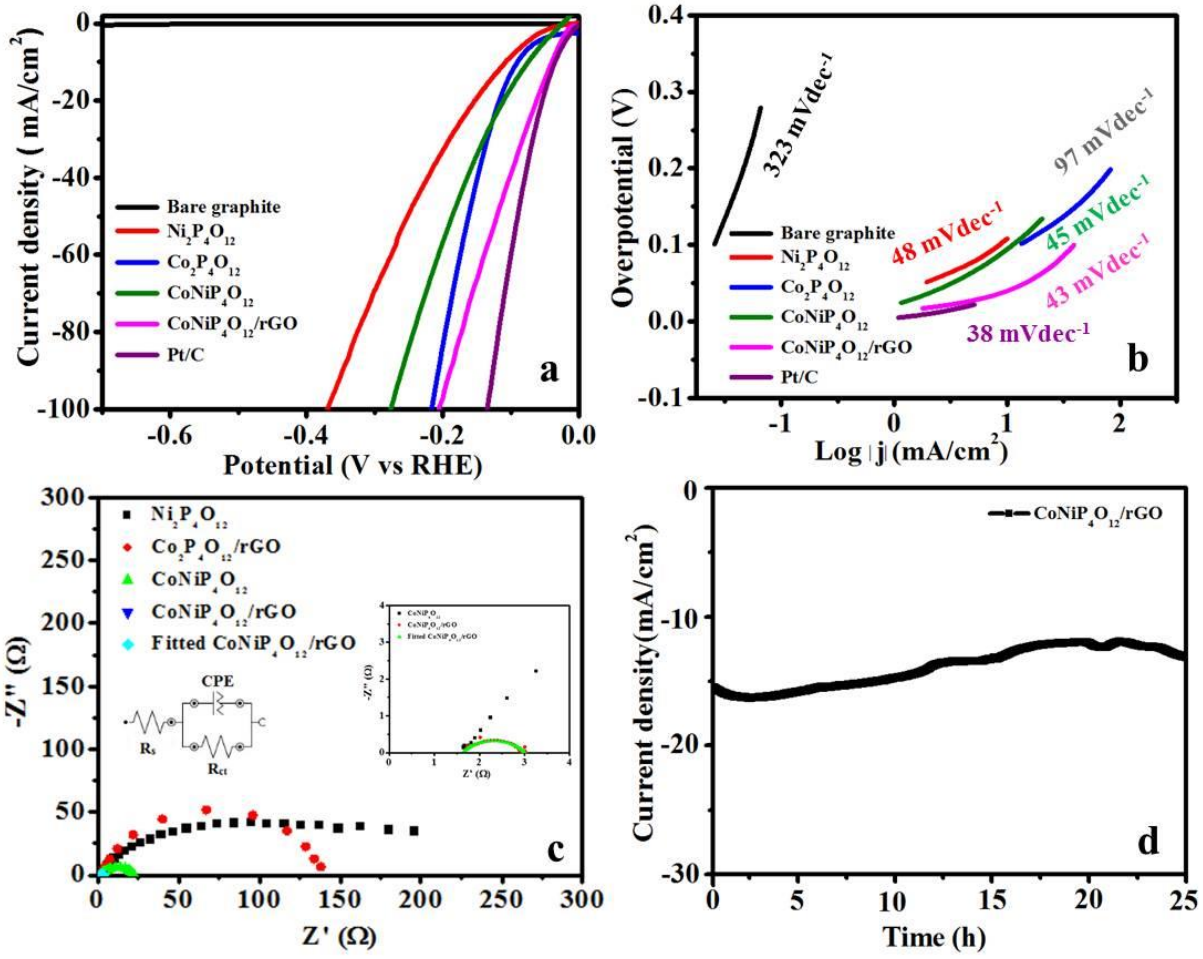

Figure 4.8. a) LSV curves, b) Tafel slope, c) EIS studies of $CoNiP_4O_{12}$ /rGO, $CoNiP_4O_{12}$, $Ni_2P_4O_{12}$,$Co_2P_4O_{12}$ and bare graphite respectively and d) represents stability studies of $CoNiP_4O_{12}$ /rGO

Table 4.1. Comparison table of transition metal based electrocatalyst for HER in 0.5 M H_2SO_4

S.no.	Material	Overpotential (η_{10}) (mV)	Tafel slope (mV/dec)	References
1	$Zn_{0.30}Co_{2.70}S_4$	80	47.5	[18]
2	3D-NiCoP	80	37	[19]
3	MoNiP	134	66	[20]
4	CoNiP Nanoboxes	138	65	[21]
5	Co_2Ni_1N	92	55.3	[22]
6	CoNi@NCNTs-700	130	82.1	[23]
7	$Co_2P_4O_{12}$	92	97	[12]
8	$Ni_2P_4O_{12}$	105	48	[11]
9	$TiO_2@Co_2P_4O_{12}$	198 (η_{20})	113	[10]
10	$Ni_2P_4O_{12}$	131	47.8	[24]
11	$CoNiP_4O_{12}$	75	45	This work
	$CoNiP_4O_{12}$/rGO	41	43	

For an advanced electrocatalyst, the large exposed catalytic active sites are essential.[25] To measure the electrochemical active surface area (ECSA), the simple cyclic voltammetry (CV) method was used (*Figures 4.9*). The cyclic voltammogram for the prepared catalysts were recorded in the non-faradic region in the potential window of -0.10 to 0.10 V vs Ag/AgCl (*Figure 4.9a-c*). The electrochemical double layer capacitance has been obtained from the slope of the curve between difference in anodic and cathodic current densities vs scan rate. The electrochemical double layer capacitance (C_{dl}) of $CoNiP_4O_{12}$ is 9 mF/cm^2 which is higher than that of $Co_2P_4O_{12}$ which has a C_{dl} value of 5 mF/cm^2, demonstrating that the addition of a second metal can greatly boost the capacitance of metal cyclotetraphosphate materials (*Figure 4.9d*). Additionally, $CoNiP_4O_{12}$/rGO has a C_{dl} value of 11 mF/cm^2 which is higher than that of $CoNiP_4O_{12}$. The ECSA is directly proportional to C_{dl} as shown in the

equation 4.1. Therefore $CoNiP_4O_{12}$/rGO has a higher ECSA and more accessible surface for the electrolyte than other catalysts.

$$ECSA = \frac{C_{dl}}{C_S} \qquad 4.1$$

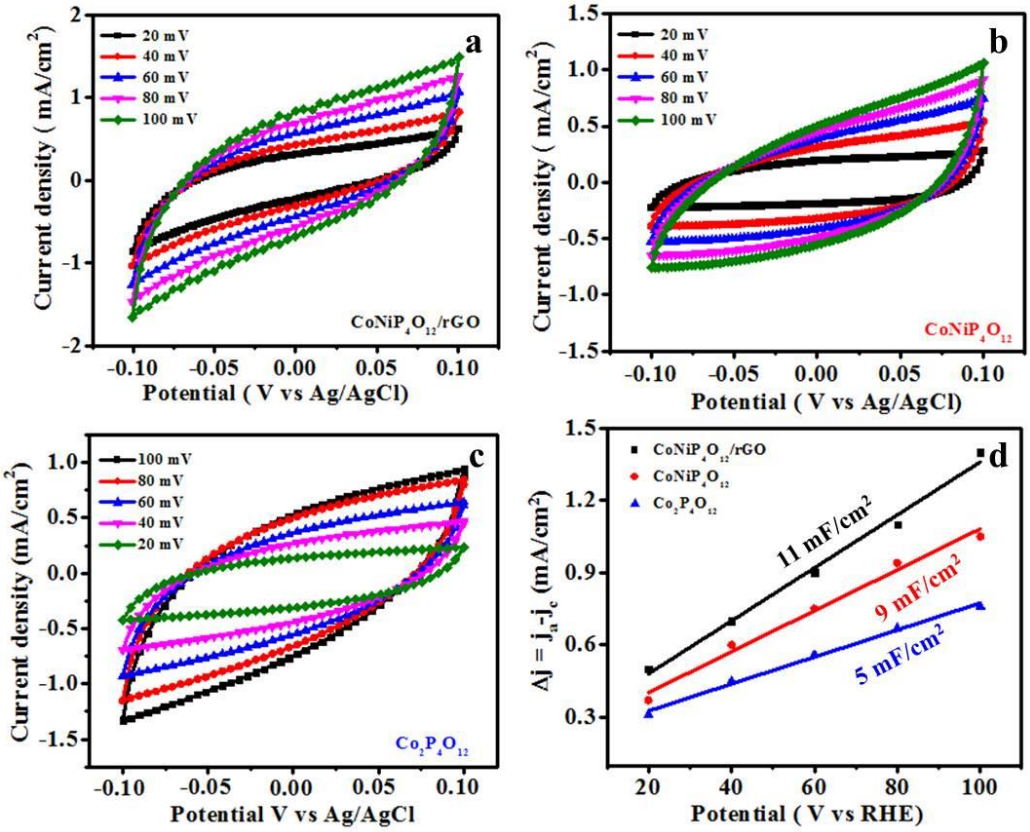

Figure 4.9. a) CV curves with different scan rates in non-faradaic region b) and c) capacitive current at different scan rate

Further Post electrochemical studies of the catalyst were carried out by using PXRD and XPS. From the diffraction pattern it was observed that there is no change in the phase and diffraction peaks of $CoNiP_4O_{12}$/rGO as shown in *Figure 4.10*. Additionally, we have also carried high resolution XPS. In XPS there is no change in the peaks of catalyst of Co 2p, Ni 2p, P 2p and O 1s as shown in the *Figure 4.11*. Post electrochemical analysis using PXRD and XPS indicates the high stability of the catalyst in the acidic medium. Thus, in the present work the activity of the bimetallic cyclotetraphosphate has been enhanced for the HER activity by making a composite with the rGO which is a highly durable and robust catalyst for the HER in the acidic medium.

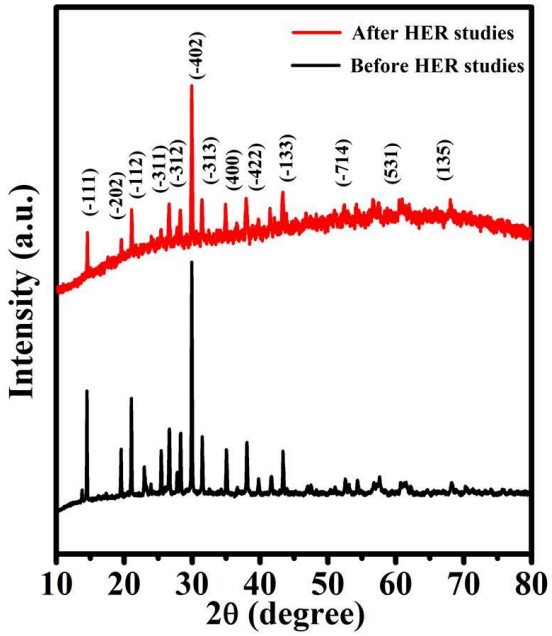

Figure 4.10. Powder X-ray diffraction pattern before and after stability studies

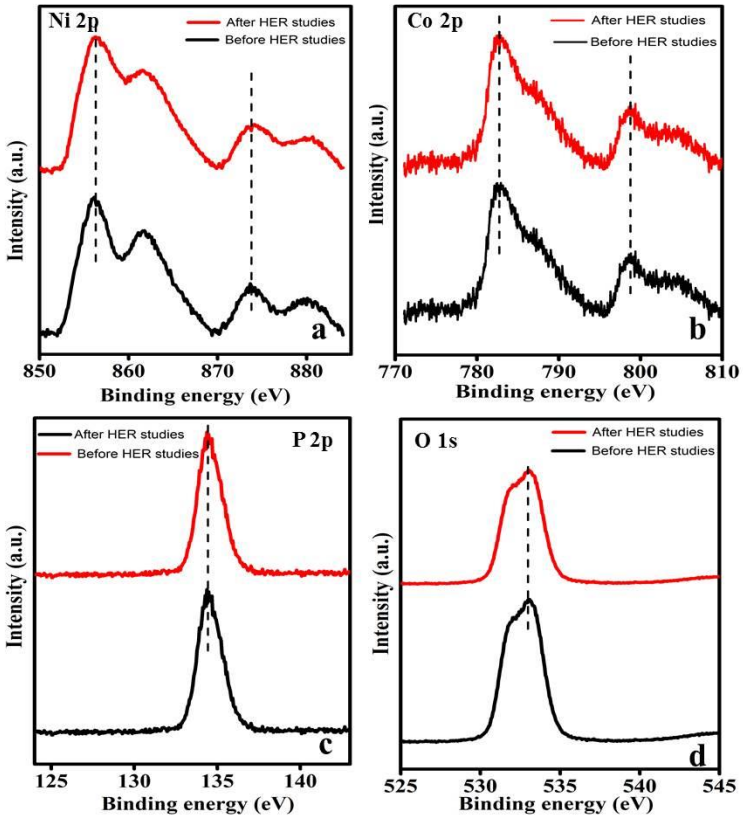

Figure 4.11 XPS studies of $CoNiP_4O_{12}$ /rGO after stability

4.4. Conclusions

In the present chapter, to increase the electrocatalytic activity of monometallic cyclotetraphosphate we have synthesized bimetallic cylotetraphopshate. $CoNiP_4O_{12}$ show low overpotential (74 mV), tafel slope (45 mV/dec) and charge transfer resistance (18 ohm) than its corresponding monometallic cyclotetraphosphates $Co_2P_4O_{12}$ and $Ni_2P_4O_{12}$. This high activity towards HER is due to second metal incorporation which increases its intrinsic catalytic behavior by synergistic effect of both the metals. Further catalytic activity of the bimetallic cyclotetraphosphate has been increased by synthesizing its composite with rGO ($CoNiP_4O_{12}$/rGO) which provide higher electrical conductivity and decreases the charge transfer resistance during electrochemical process. $CoNiP_4O_{12}$/rGO requires overpotential of 41 mV to reach the benchmark of 10 mA/cm^2 and shows stability up to 25 h in acidic medium. With regard to HER applications, current study not only offers us a unique, reasonably priced hydrogen-evolving electrocatalyst with good activity and durability, but also a fundamental design methodology for other transition metal phosphorous based materials.

4.5. References

1. Adam, A. *et al.* Interconnected Hollow Cobalt Phosphide Grown on Carbon Nanotubes for Hydrogen Evolution Reaction. *ACS Appl. Mater. Interfaces* **10**, 29407–29416 (2018).
2. Yue, X., Yi, S., Wang, R., Zhang, Z. & Qiu, S. Cobalt Phosphide Modified Titanium Oxide Nanophotocatalysts with Significantly Enhanced Photocatalytic Hydrogen Evolution from Water Splitting. *Small* **13**, 1–9 (2017).
3. Lukowski, M. A. *et al.* Enhanced hydrogen evolution catalysis from chemically exfoliated metallic MoS2 nanosheets. *J. Am. Chem. Soc.* **135**, 10274–10277 (2013).
4. Chen, Y. *et al.* Superior electrocatalysis for hydrogen evolution with crumpled graphene/tungsten disulfide/tungsten trioxide ternary nanohybrids. *Nano Energy* **47**, 66–73 (2018).
5. Zhai, L. *et al.* In Situ Phase Transformation on Nickel-Based Selenides for Enhanced Hydrogen Evolution Reaction in Alkaline Medium. *ACS Energy Lett.* **5**, 2483–2491 (2020).

6. Liu, X. *et al.* A porous nickel cyclotetraphosphate nanosheet as a new acid-stable electrocatalyst for efficient hydrogen evolution. *Nanoscale* **10**, 9856–9861 (2018).
7. Patil, D. R. *et al.* Cobalt Cyclotetraphosphate ($Co_2P_4O_{12}$): A New High-Performance Electrode Material for Supercapacitors. *ACS Appl. Energy Mater.* **2**, 2972–2981 (2019).
8. Wang, J. *et al.* Crystalline-Amorphous $Ni_2P_4O_{12}$/NiMoOx Nanoarrays for Alkaline Water Electrolysis: Enhanced Catalytic Activity via In Situ Surface Reconstruction. *Small* **18**, (2022).
9. Huang, J. *et al.* A New Member of Electrocatalysts Based on Nickel Metaphosphate Nanocrystals for Efficient Water Oxidation. *Adv. Mater.* **30**, 1–9 (2018).
10. Lv, C., Xu, S., Yang, Q., Huang, Z. & Zhang, C. Promoting electrocatalytic activity of cobalt cyclotetraphosphate in full water splitting by titanium-oxide-accelerated surface reconstruction. *J. Mater. Chem. A* **7**, 12457–12467 (2019).
11. Ankush, Yadav, K. K., Guchhait, S. K., Wadhwa, R. & Jha, M. Surface phosphorization of nickel oxalate nanosheets to stabilize ultrathin nickel cyclotetraphosphate nanosheets for efficient hydrogen generation. *Mater. Res. Bull.* **139**, 111275 (2021).
12. Ankush, Yadav, K. K., Guchhait, S. K., Rana, S. & Jha, M. Excellent hydrogen generation from ultrathin nanosheets of cobalt cyclotetraphosphate. *Mater. Sci. Eng. B* **265**, 114983 (2021).
13. Li, Y. *et al.* Metal–organic frameworks derived interconnected bimetallic metaphosphate nanoarrays for efficient electrocatalytic oxygen evolution. *Wiley Online Libr.* **30**, (2020).
14. Lamiel, C., Lee, Y. R., Cho, M. H., Tuma, D. & Shim, J. J. Enhanced electrochemical performance of nickel-cobalt-oxide@reduced graphene oxide//activated carbon asymmetric supercapacitors by the addition of a redox-active electrolyte. *J. Colloid Interface Sci.* **507**, 300–309 (2017).
15. Wang, J. *et al.* Preparation of cobalt sulfide@reduced graphene oxide nanocomposites with outstanding electrochemical behavior for lithium-ion batteries. *RSC Adv.* **10**, 13543–13551 (2020).
16. Boonchom, B. & Vittayakorn, N. A rapid synthesis of cobalt cyclotetraphosphate

Co2P 4O12 at low temperature. in *Ceramics International* **39**, (2013).

17. Wu, Z. *et al.* Highly efficient and stable MoP-RGO nanoparticles as electrocatalysts for hydrogen evolution. *Electrochim. Acta* **232**, 254–261 (2017).
18. Huang, Z. F. *et al.* Hollow Cobalt-Based Bimetallic Sulfide Polyhedra for Efficient All-pH-Value Electrochemical and Photocatalytic Hydrogen Evolution. *J. Am. Chem. Soc.* **138**, 1359–1365 (2016).
19. Ma, B., Yang, Z., Chen, Y. & Yuan, Z. Nickel cobalt phosphide with three-dimensional nanostructure as a highly efficient electrocatalyst for hydrogen evolution reaction in both acidic and alkaline electrolytes. doi:10.1007/s12274-018-2226-2
20. Li, J. *et al.* Bimetallic Phosphides as High-Efficient Electrocatalysts for Hydrogen Generation. *Inorg. Chem.* **60**, 1624–1630 (2021).
21. Lu, Y. *et al.* MOF-derived cobalt–nickel phosphide nanoboxes as electrocatalysts for the hydrogen evolution reaction. *Nanoscale* **11**, 21259–21265 (2019).
22. Feng, X., Wang, H., Bo, X. & Guo, L. Bimetal-Organic Framework-Derived Porous Rodlike Cobalt/Nickel Nitride for All-pH Value Electrochemical Hydrogen Evolution. *ACS Appl. Mater. Interfaces* **11**, 8018–8024 (2019).
23. Xie, Y. *et al.* MOFs derived carbon nanotubes coated CoNi alloy nanocomposites with N-doped rich-defect and abundant cavity structure as efficient trifunctional electrocatalyst. *Elsevier*
24. Liu, X. *et al.* A porous nickel cyclotetraphosphate nanosheet as a new acid-stable electrocatalyst for efficient hydrogen evolution. *Nanoscale* **10**, 9856–9861 (2018).
25. Long, X. *et al.* Metallic Iron-Nickel Sulfide Ultrathin Nanosheets As a Highly Active Electrocatalyst for Hydrogen Evolution Reaction in Acidic Media. *J. Am. Chem. Soc.* **137**, 11900–11903 (2015).

Chapter 5

Mechanistic aspects of excellent hydrogen evolution from cobalt phosphide nanorods derived using cobalt oxalate rods

5.1. Introduction

Hydrogen is reflected as a source of clean, sustainable, eco-friendly and high energy density fuel for the future.[1–3] Electrolysis of water to generate hydrogen is one of the main methodology to produce high purity hydrogen at a low cost.[4–7] Water electrolysis involves two reactions named as oxygen evolution reaction (OER) occurrs at the anode and hydrogen evolution reaction (HER) at cathode respectively. Both reactions (HER and OER) have sluggish kinetics in absence of catalyst, therefore active electrocatalysts will always be needed to accelerate the process. Earlier, noble metals like Platinum and Palladium are considered as best electrocatalyst for the HER via water splitting; though, owing to their expensiveness and scarcity in nature, their wide implementation is not feasible.[8–11] Therefore, efficient, low-priced and earth crust rich electrocatalysts are in great demand. Recently, transition metals based electrocatalysts are utilized for hydrogen-related clean energy conversion processes. Earlier, transition metal phosphides (TMPs)[12,13], sulphides[14–16], carbides[17,18] and nitrides[19,20] are widely used as electrocatalyst for hydrogen evolution reaction (HER). Among them, nanostructured transition metal phosphides of nickel, cobalt, molybdenum, tungsten and iron are the most efficient catalyst towards HER.[21–25] In transition metal phosphide, cobalt phosphide is not explored well; however, the earlier reports of Cobalt phosphide shows a reasonable HER activity, Cobalt phosphide nanostructures have been synthesized using different methods and shows efficient HER activities in acidic aqueous electrolyte.[26,27] But the major drawback for their use is the limited number of active sites and its poor electrical conductivity.[28] Efforts have been made to tailor their structure to increase the activity of the catalyst and to improve their physiochemical properties.[29] Zhu Li et al. has synthesized hollow cobalt phosphide nanoparticles anchored on rGO and obtained an overpotential of 190 mV at 10 mA cm^{-2}.[30] Doping of metals such as Vanadium, Nickel and Gold has been done on CoP surface to enhance their catalytic activity.[31–33] Cobalt Phosphide has also been incorporated in the MOFs and carbon nitride structures to achieve better performance.[29,34] In the present work, Co_2P nanorods were synthesized by carrying out phosphorization of cobalt oxalate rods without any modification or use of another metal by simply maintaining the morphology of the precursor. Cobalt oxalate rods were firstly synthesized by micellar route using cationic surfactant (CTAB). The synthesized Co_2P

nanorods showed an overpotential of 117 mV to attain 10 mA cm^{-2} current density and are highly durable in acidic media**.**

5.2. Experimental

5.2.1. Chemicals Required

Sodium hypophosphite monohydrate ($NaH_2PO_2.H_2O$, 99% Sigma Aldrich), Sulfuric acid (H_2SO_4, 98% Merck), Cetyl-tri-methyl ammonium bromide (CTAB, 99 % CDH), Cobalt nitrate hexahydrate (Co $(NO_3)_2.6H_2O$, 98 % Merck), methanol (CH_3OH, 99 % CDH), 5 % Pt/C (5 % platinum on carbon, Sigma-Aldrich) and Ammonium oxalate ($(NH_4)_2C_2O_4$, 99 %, Merck) were used as received. The detailed experimental method has been discussed in supporting information.

5.2.2. Synthesis of cobalt oxalate and cobalt phosphide

Micellar route was opted for the synthesis of cobalt oxalate, in which CTAB was used as capping agent. In a typical synthesis of cobalt oxalate, 50 mL of aqueous solution of 0.1 M $Co(NO)_3.6H_2O$ and 0.1 M $(NH_4)_2C_2O_4$ were taken and 1 % v/v of CTAB was added to both the solutions and stirred for 1 h. Both solutions were mixed and stirred for 12 h which leads to the formation of a pink color precipitate. The precipitates were collected after centrifugation and washed with methanol and chloroform (1:1 v/v) mixture to remove any impurity of surfactant and dried in a hot air oven. For further synthesis of cobalt phosphide, first cobalt oxalate and NaH_2PO_2 were taken in 1:5 w/w ratio and grinded together in mortar pastel. The grinded mixture has been transferred into recrystallized alumina boat and annealed at 350 ºC for 6 h in argon atmosphere. After annealing a black colored sample of cobalt phosphide was obtained and stored in vacuum desiccator.

5.2.3. Fabrication of working electrode

To perform the electrochemical measurements, the electrodes were prepared by layer deposition of cobalt phosphide sample on to a graphite substrate. For this, firstly, the cobalt phosphide dispersion was prepared by dispersing 5 mg of sample in 200 µl of ethanol and ultra-sonicated for 45 min. Further, 10 µl of Nafion was added to the above dispersion and ultra-sonicated for another 15 minutes. Finally, the 20 µl of this dispersion was drop casted on to a graphite substrate and dried in vacuum oven at 60 ºC for 2 h.

5.2.4. Characterization

Bruker D8 advance diffractometer is used to determine the phase and structure of the materials which is equipped with Cu-$K_{\alpha 1}$ (λ= 1.54Å) source. The shape and size of all the materials have been studied using Transmission electron microscope (TEM, JEOL JEM-2100). The compositional studies of cobalt phosphide were measured by EDAX (energy dispersive X-ray spectroscopy) analyzer coupled with TEM JEOL JEM-2100. Electrochemical performance of all the materials has been evaluated on the Metrohm PGSTAT-30 Autolab workstation. Contact angle studies were performed using drop analyser DSA25-KRUSS GmbH. Post electrochemical stability studies for the leaching of catalyst in the electrolyte is carried out using Agilent -7900 ICP-MS spectrometry, X-ray photoelectron spectroscopy was performed on Thermoscientific K-alpha X-ray Photoelectron Spectrometer (XPS) System equipped with Al as a source.

5.2.5. Electrochemical measurements

Electrochemical performance of all the materials has been measured on a three-electrode system present in the Metrohm PGSTAT-30 Auto lab workstation. In this experiment, all studies were carried out in 50 ml of sulphuric acid (0.5 M H_2SO_4). For, Graphite rod was used as counter electrode and cobalt phosphide coated graphite sheet (0.5*1 cm^2) was used as working electrode. Apart from that Ag/AgCl reference electrode has been used in the present experiment. For HER measurement, linear sweep voltammetry (LSV) studies of the prepared materials have been done at a scan rate of 5 mV/sec in the potential gap of 0 V to -1 V vs Ag/AgCl. To measure intrinsic resistance of all materials electrochemical impedance spectroscopy (EIS) was done at potential of -0.4 V vs Ag/AgCl in the frequency range of 0.01 Hz to 100 kHz. The potentials were converted using Nernst Equation with respect to RHE [35].

$$E_{RHE} = E_{Ag/AgCl} + 0.059\ pH + 0.21\ V \qquad 5.1$$

All the measurements were also carried out for Pt/C to compare the electrochemical activity of Co_2P with that of state of art material.

5.3. Results and discussion

Here, an effort was made to fabricate efficient electrocatalyst towards HER via electrochemical water splitting. The present work was done in two steps: In the first step, the synthesis of anisotropic cobalt oxalate rods via micellar route. In the second step, the conversion of 1-D cobalt oxalate to cobalt phosphide with retention of morphology was done at a slow annealing rate. Finally, the synthesized cobalt phosphide nanorods were utilized for hydrogen evolution and the mechanism behind it was investigated.The product obtained after the reaction of Co^{2+} micelle with $C_2O_4^{2-}$ micelle was analyzed by PXRD pattern. The entire diffraction pattern matched with the reported $Co_2C_2O_4.2H_2O$ orthorhombic phase (JCPDS no. 00-025-250) (*Figure 5.1*). The reflections (hkl) indexed with 202, 112, 004, 114, 400, 313, 022, 116, 510, 512, 317, 131, and 620 corresponds to 2θ value at 18.65, 21.29, 22.71, 24.85, 29.16, 30.07, 34.98, 39.08, 43.34, 46.81, 48.43, 52.52and 62.98 ° respectively.

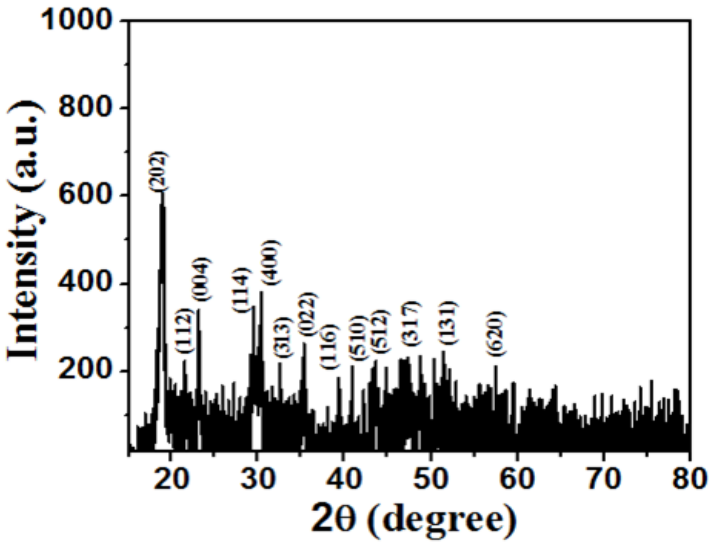

Figure 5.1. Diffraction pattern of as synthesized $CoC_2O_4.2H_2O$

Further, the morphological studies of the cobalt oxalate have been done using TEM (*Figure 5.2*) which shows that rod-like structure has been formed having length ~2.2 µm, diameter ~ 0.5 µm, with an aspect ratio of 4.4. The mechanism for the growth of cobalt oxalate rods has been studied using zeta potential. To synthesize cobalt oxalate aqueous solution ammonium oxalate and cobalt nitrate were taken separately with CTAB for the formation of micelles. The zeta potential studies show that $C_2O_4^{2-}$ micelles had a surface potential value of + 8.95 mV while for Co^{2+} micelles is + 11.2 mV. For the formation of cobalt oxalate rods both

capped micelles of Co^{2+} and $C_2O_4^{2-}$ were mixed together. The rods of cobalt oxalate have a zeta potential of -38.5 mV indicating their high stability.

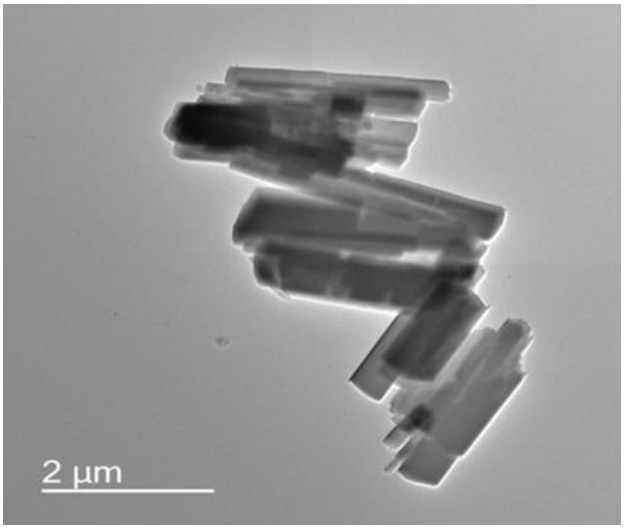

Figure 5.2. TEM image of as synthesized $CoC_2O_4.2H_2O$

CTAB is a cationic surfactant due to the positive charge on the ammonium head group and the zeta potential value of cobalt oxalate indicates that it has a negatively charged surface. Based on the observation of the zeta potential results it is anticipated that cationic CTAB molecules show template effect and organize themselves in such a fashion that it leads to the linear arrangement of ligand and metal. Therefore, the growth is constrained along one dimension and leads to the formation of cobalt oxalate rods [36]. Earlier, efforts have been made by Sharma et al. to synthesize anisotropic cobalt oxalate nanorods via the thermal decomposition method maintaining a slow heating rate [37]. Here, we attempted a similar methodology to retain the morphology of cobalt oxalate nanorods during the phosphorization process using NaH_2PO_2 as a phosphorus source. The well-grinded solid-state mixture of cobalt oxalate and NaH_2PO_2 was annealed at 350 ºC in Argon atmosphere at a slow heating rate of 2 ºC/min. *Figure 5.3a* shows the PXRD pattern of the annealed sample and it is well-matched with the orthorhombic phase of Co_2P (JCPDS no 01-89-3032) and 2θ values at 40.7, 43.3, 44.1, 48.8, 52.1 and 54 ° corresponds to 112, 211, 103, 020 and 302 planes, respectively. *Figure 5.3b* shows the morphological studies of Co_2P examined by TEM which depicts the presence of nanorods of size up to length 59 nm and width 15 nm. The high-resolution TEM image (*Figure 5.3c*) clearly shows inter-planar spacing of 0.20 nm of Co_2P

(211) crystal plane, which confirms that phosphorization is successfully done. The TEM-EDX confirms the occurrence of phosphorous and cobalt elements in the material (*Figure 5.3d*).

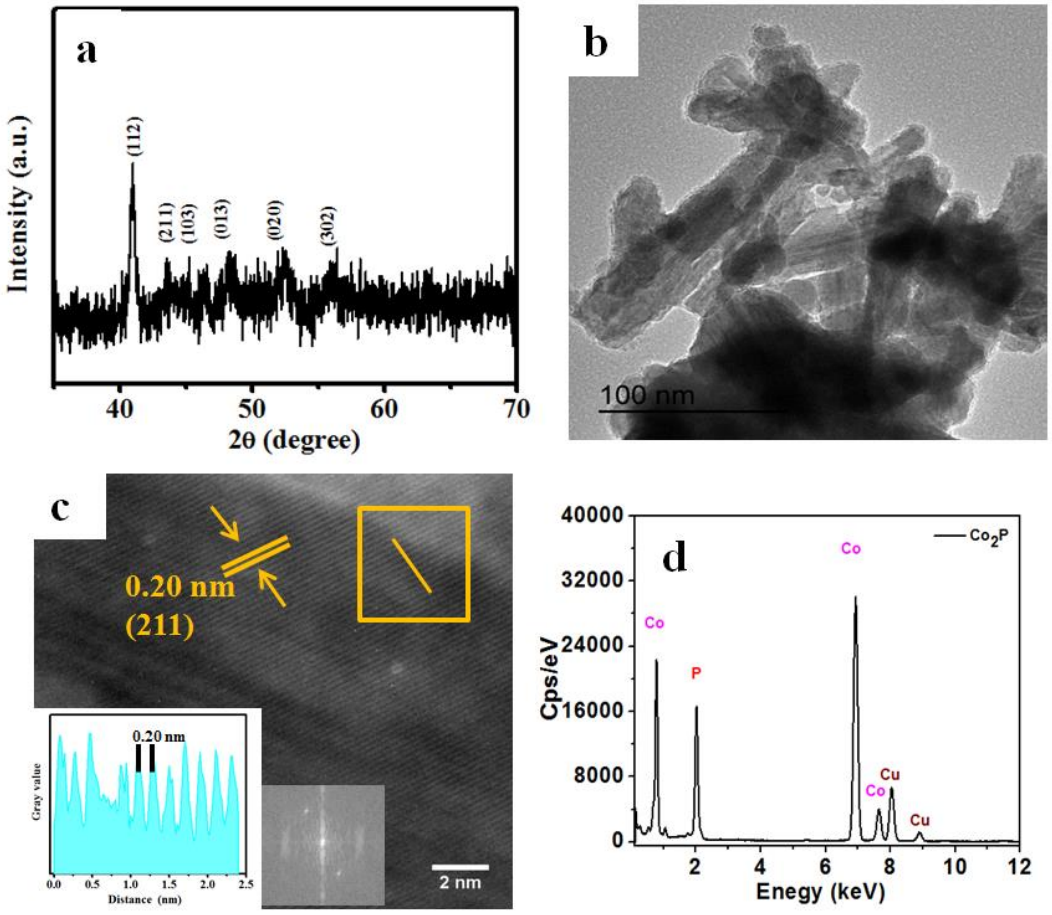

Figure 5.3. a) Powder X-ray diffraction pattern b) TEM micrograph c) HRTEM micrograph (insight plot profile and FFT) and d) elemental composition by TEM-EDAX of Co_2P

For the synthesis of Co_2P, NaH_2PO_2 has been utilized as a phosphorous source. The mechanism for the synthesis of the Co_2P nanorods can be better understood in this way; when the sodium hypophosphite was heated over the temperature of 250 ºC, they tend to decompose to give PH_3 which further reacts with the cobalt precursor to form Co_2P nanorods. The reactions involved are

$$2\ NaH_2PO_2 \rightarrow PH_3 + Na_2HPO_4$$

$$12\ CoC_2O_4 + 6\ PH_3 \rightarrow 6\ Co_2P + 24\ CO_2 + 9\ H_2$$

This surfactant-free type of solid-gas reaction is appropriate for retaining the morphology and dimensions of the precursors.[38,39] The shrinkage of cobalt oxalate rods to cobalt phosphide nanorods have been studied by TGA. The TGA study of $CoC_2O_4.2H_2O$ has been done which shows that up to 280 ºC there is no significant change in graph (*Figure 5.4*). The weight loss of $CoC_2O_4.2H_2O$ was done in 2 steps. In first step corresponds to evaporation of water and in second step CoC_2O_4 decomposes into Co_3O_4 and CO_2 [40].

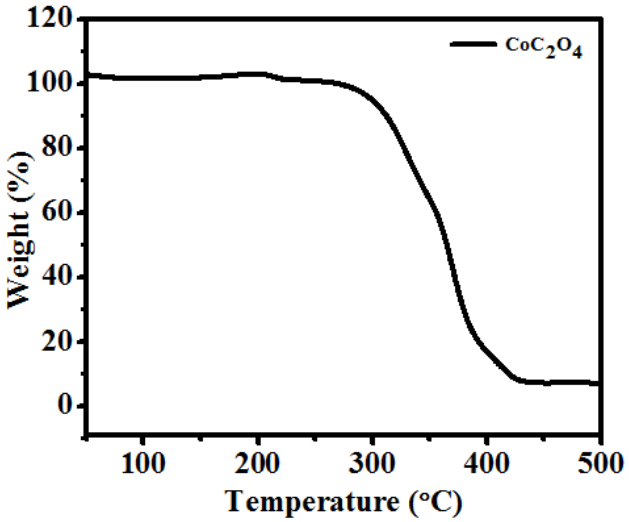

Figure 5.4. Thermogravimetric analysis (TGA) curve of $Co_2C_2O_4.2H_2O$

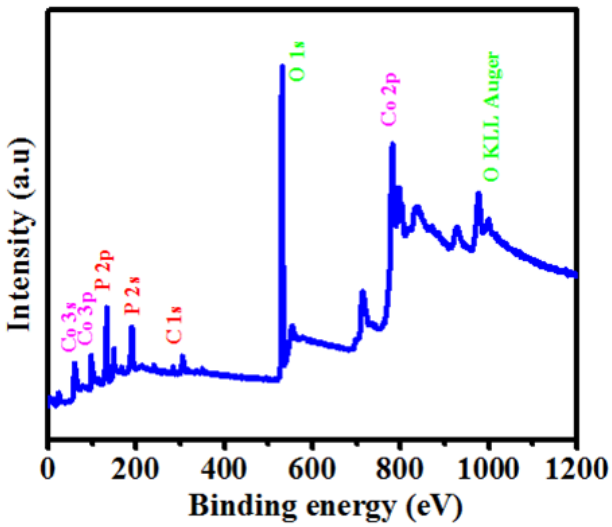

Figure 5.5. XPS survey spectrum of as synthesized Co_2P

To further analyze chemical state and elemental composition X-ray photoelectron spectroscopy (XPS) was done on the surface of Co_2P. An XPS survey spectrum shows the presence of Co, P and O elements in the sample as shown in *Figure 5.5*.

The High-resolution XPS spectra of Co 2p and P 2p are shown in *Figure 5.6a-b*. *In Figure 5.6a*, Co 2p spectrum splits into two doublet peaks of $2p_{3/2}$ at 778.3 eV, 781.9 eV and $2p_{1/2}$ at 793.3 eV, 798.2 eV respectively which are in close agreement with the earlier reports.[38,41] In Co 2p spectrum, the peaks at 781.9 eV and 798.2 eV attributed to Co^{2+} binding energies and the peaks at 778.3 eV and 793.3 eV are attributed to cobalt phosphide [42]. In P 2p spectrum (*Figure 5.6b)*, peak at 129.4 eV attributed to $2p_{3/2}$ and 130.3 eV attributed to $2p_{1/2}$ respectively, which corresponds to cobalt phosphide. In P 2p spectrum, the peak at $2p_{3/2}$ at 134.2 eV ascribed to oxidized phosphorous (P-O) species on the surface [42]. The positive shift of cobalt $2p_{3/2}$ peak in Co_2P from that of metallic cobalt (777.9 eV) show that there is some partial charge on Co ($0< \delta >2$) and there is negative shift of phosphorous $2p_{3/2}$ peak (129.4 eV) from Co_2P than that of elemental phosphorous (130.2 eV) illustrate there is some partial negative charge . Therefore it shows that electron density in Co_2P moves from cobalt to phosphorous [43].

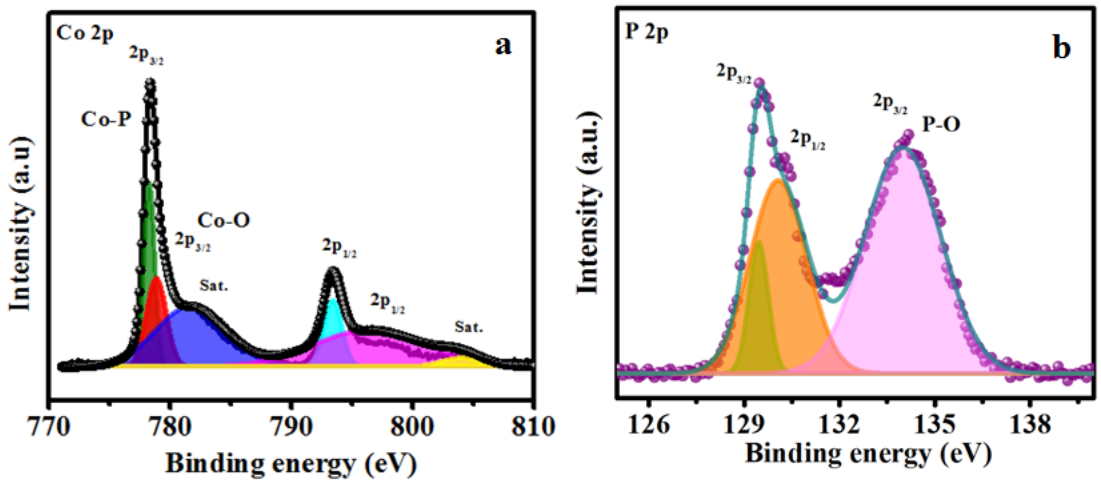

Figure 5.6. High-resolution XPS spectra of Co_2P nanorods a) Co 2p and b) P 2p

5.3.1. Electrochemical performance

The catalytic activity of the synthesized cobalt phosphide nanorods for HER was analysed using LSV studies. To compare HER activity of cobalt phosphide, the electrochemical measurements of $Co_2C_2O_4$, bare graphite and 5 % Pt/C catalyst were also carried out.

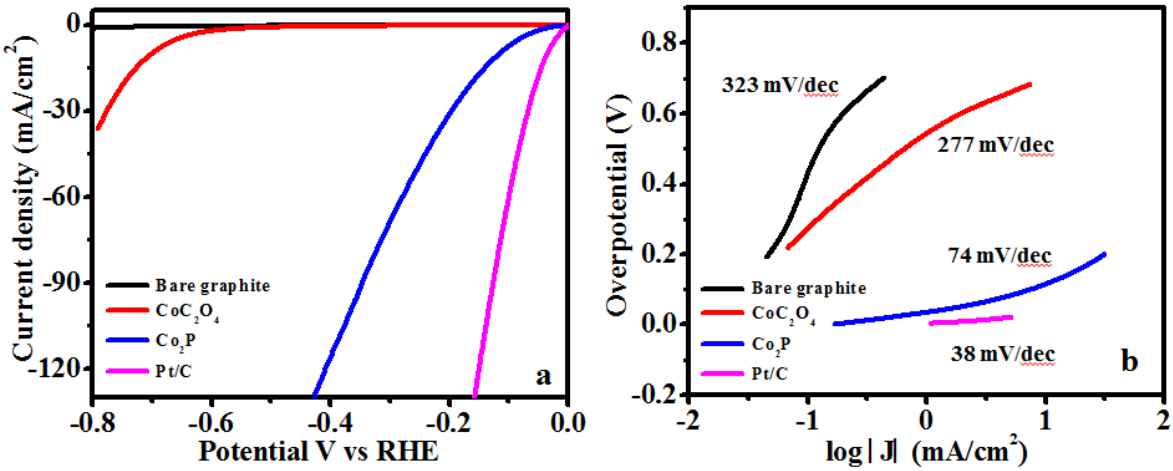

Figure 5.7. a) LSV curves and b) Tafel slope of Co_2P, Pt/C, $Co_2C_2O_4$ and bare graphite

The LSV curves shown in *Figure 5.7a* indicates that the cobalt phosphide shows a potential of 117 mV and 163 mV to achieve the cathodic current density of 10 and 20 mA/cm^2 where as that of bare graphite does not even reach this benchmark. This signifies that graphite has a very little contribution towards the electrocatalytic HER activity. However, at the same time, for the 5 % Pt/C catalyst a small overpotential(η_{10}= 37 mV) is required. A Comparison table of the HER efficiency in terms of overpotential, Tafel slope with the Co_2P nanorods in 0.5 M H_2SO_4 has given in *Table 5.1*. The low overpotential of cobalt phosphide indicates its high efficiency for HERTafel slope gives information about the kinetics of the electrocatalytic reaction. To get insights about the kinetics of cobalt phosphide nanorods, Tafel plots were derived from the linear region of the polarization curve of Co_2P by fitting it to the Tafel equation ($\eta = b \log j + x$) where b is Tafel slope, η is overpotential, and j is the current density. In the acidic medium, three major reactions takes place based on the two mechanisms that are followed during the HER process.[44]

$$H^+ (aq) + e^- \rightarrow H_{ads} \quad 5.2$$

$$H_{ads} + H^+ (aq) + e^- \rightarrow H_2 (g) \quad 5.3$$

$$H_{ads} + H_{ads} \rightarrow H_2\,(g) \qquad 5.4$$

During the first step, discharge process takes place, in which the capturing proton (H^+) and transferred electron to the surface of the catalyst get combined resulting in the formation of adsorbed hydrogen atom. During second step, in the Heyrovsky mechanism H_2 is evolved when a proton and new electron are combined with H_{ads} and when the Tafel mechanism is followed; H_2 is evolved by the combination of adjacent H_{ads}. The Tafel slope in case of Pt/C is 38 mV/dec^{-1} and it is comparable to that of the earlier values.[45] The obtained value of Tafel slope for the cobalt phosphide was 74 mVdec^{-1} which is much smaller than that of cobalt oxalate (277 mVdec^{-1}) and bare graphite (323 mVdec^{-1}) as depicted in *Figure 5.7b*. Furthermore, as the Tafel slope for Co_2P is 74 mVdec^{-1}, which indicates that Volmer–Heyrovsky reaction mechanism is being followed for HER.[46] The cobalt phosphide nanorods suggest more favourable conditions and high charge transfer kinetics towards electrocatalytic HER owed to its small Tafel slope.

Table 5.1. Electrochemical performance of different catalysts for HER in 0.5 M H_2SO_4

S.no.	Material	Overpotential (mV)	Tafel slope (mV/decade)	References
1	Cobalt phosphide nanorods	167 (η_{20})	51.7	[42]
2	MOF-derived nanostructured cobalt phosphide assemblies	181 (η_{10})	69	[34]
3	Co_2P/NCNT	171 (η_{20})	62	[47]
4	Co_2P/CNT	219 (η_{20})	74	[47]
5	Ni-Co-S/FTO	280 (η_{10})	93/70	[48]
6	CoP -CNT hybrid	139 (η_{10})	53	[49]
7	CoP@NC-NG	135 (η_{10})	59.3	[44]
9	Cu_3P	143 (η_{10})	67	[50]
10	Co_2P/CoP	144 (η_{10})	58	[51]

11	CoP@C nanocables	170 (η_{10})	61	[52]
12	CoP Hollow polyhedron	159 (η_{10})	59	[53]
13	N-Co@G	265 (η_{10})	98	[54].
14	FeP NPs@NPC	130 (η_{10})	67	[55]
15	H-CoP@rGO	190 (η_{10})	83	[30]
16	Co_2P nanorods	117 (η_{10}) 163 (η_{20})	74	This work

Further, EIS studies were done to gain insights into charge transfer resistance during the electrocatalysis process. The Nyquist plot of Co_2P nanorods, bare graphite and CoC_2O_4 is shown in *Figure 5.8* which was measured at -0.4 V vs Ag/AgCl. The Nova 1.1 software was used to fit EIS data. The EIS data were fitted into a Randles circuit. The semicircle observed is mainly attributed to the R_{ct}. The R_{ct} value was found to be 9 Ω for Co_2P that leads to high charge transfer and conductivity as compared to CoC_2O_4 (4200 Ω) and graphite (952 Ω).

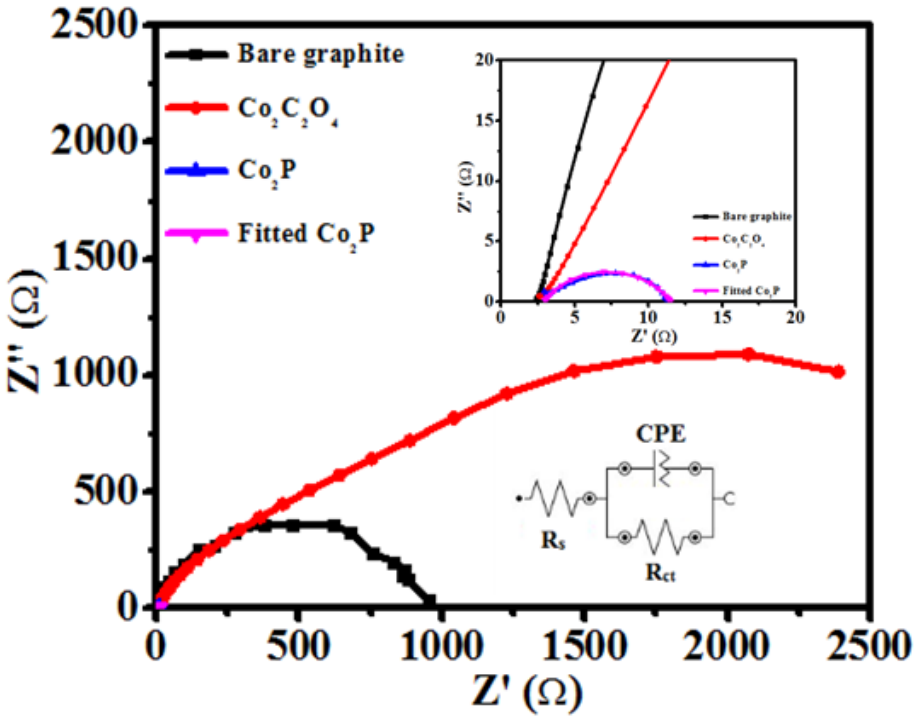

Figure 5.8. EIS studies of Co_2P nanorods, $Co_2C_2O_4$ and bare graphite

On the other hand, in the bode plot (*Figure 5.9a-b*), the peaks in the phase angle occur at higher frequencies is near to 100 Hz, while no well-resolved semicircle is not observed in the Nyquist plots, suggesting high frequency relaxation. This high-frequency relaxation is typically due to the fast charge transfer process during the HER process.[56] Further, to shed more light on the surface wettability effect on the reaction kinetics, we have also performed contact angle measurements using a drop shape analyzer. It has been found that the contact angle for the Co_2P and the bare graphite was ~ 46 º and ~ 95 º respectively (*Figure 5.10a-b*).

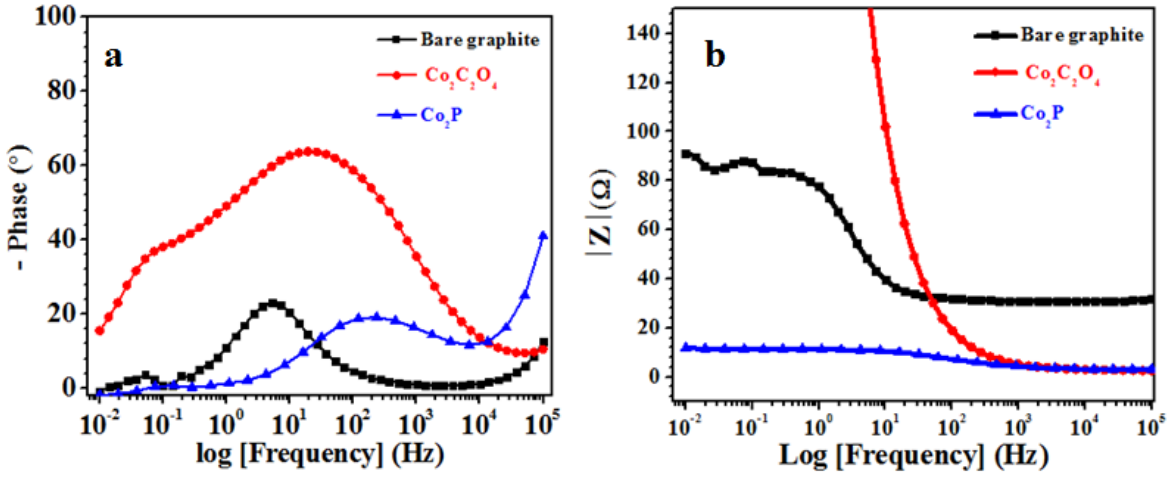

Figure 5.9. a) Bode phase and b) Bode modulus of bare graphite, CoC_2O_4 and Co_2P

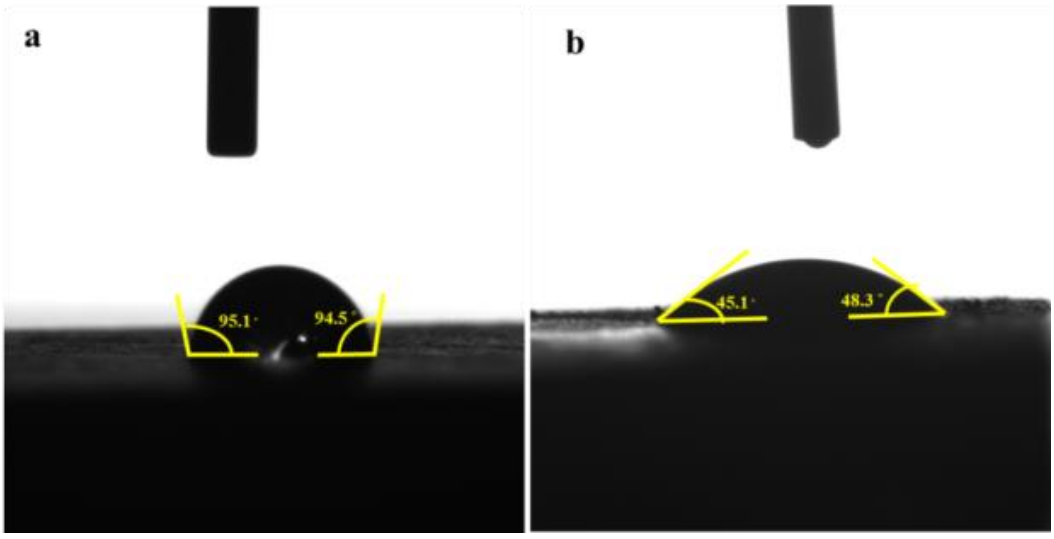

Figure 5.10. Water Contact angle measurements by sessile drop method for a) bare graphite and b) Co_2P

The low contact angle for Co_2P confirms the superior hydrophilic nature of the catalyst to that of bare graphite which shows less adhesion of the bubble onto the surface of the electrode during catalysis and consequently facilitates the faster hydrogen evolution.

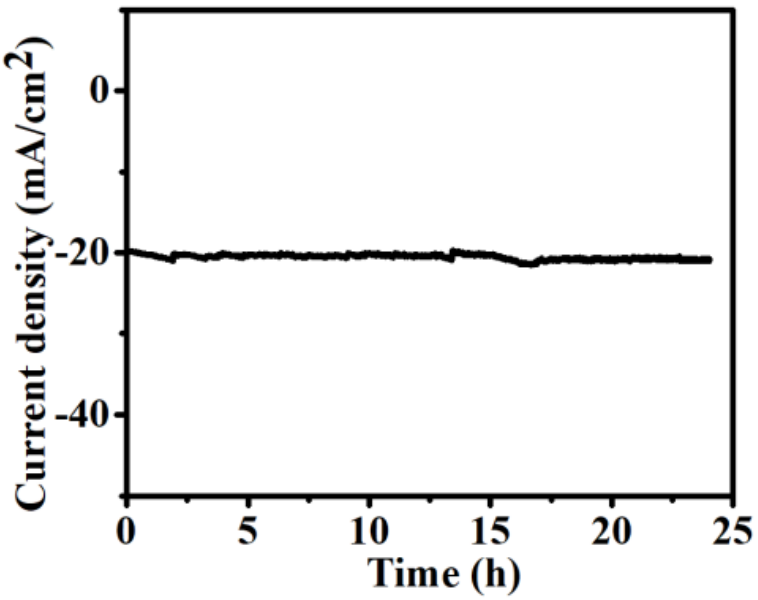

Figure 5.11. Chronoamperometric studies of Co_2P nanorods

The stability of the electrocatalyst during the electrochemical HER analysis is a crucial factor for the implementation of electrocatalyst on an industrials scale. To check this, chronoamperometry studies were performed by applying a biased voltage of -0.4 V vs Ag/AgCl on Co_2P catalyst for 24 h in 0.5 M H_2SO_4. As depicted in *Figure 5.11*, an excellent stability is shown by Co_2P and the increment in the current density takes place due to the participation of more active sites. Further, the integrity of the electrocatalyst under acidic conditions was evaluated. Inductively coupled plasma MS (ICP-MS) analysis was done to check whether there is leaching of Co_2P in the electrolyte solution by analyzing the Co^{2+} concentration in the electrolyte after chronoamperometric studies. A very low concentration (~5 ppb) of Co^{2+} in the supernatant for the Co_2P sample was obtained which indicates that there is almost negligible leaching of Co_2P in the H_2SO_4 solution and the catalyst is stable under acidic environment. The stability of the catalyst was also checked by post stability XPS studies in which it shows the presence of Co and P elements. A high-resolution spectra indicates that the Co $2p_{3/2}$ peak of Co^{2+} and P $2P_{3/2}$ of P-O species is more

intense than that of Co-P. The increase in the intensity is due to the more oxidized species (Co-O and P-O) present on the surface of catalyst (*Figure 5.12 a-b*).

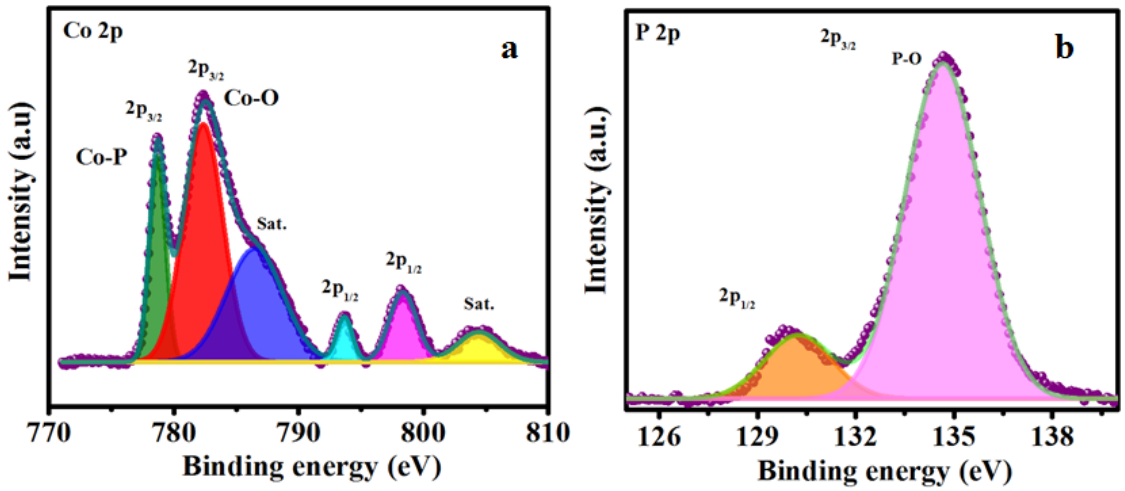

Figure 5.12. High-resolution XPS spectra after HER studies of a) Co 2p and b) P 2p

Further, to get an insight into the actual active sites of Co_2P nanorods that plays a crucial role in the catalytic activity, the electrochemically active surface area (ECSA) of Co_2P nanorods was calculated using C_{dl} (double layer capacitance) method. The C_{dl} is calculated via CV measurements in the non-faradic region. The ECSA for the prepared catalyst has been calculated using following equation:

$$ECSA = \frac{C_{dl}}{C_s} \quad (6)$$

The value of specific capacitance (C_s) in acidic media is 0.035 mF cm^{-2} [57]. For the C_{dl} calculation CV measurements are done at different scan rates in a potential gap of 0 V to -0.1 V vs Ag/AgCl (*Figure 5.13a*). A linear relationship between current density and scan rate was observed at a potential of -0.05 V (*Figure 5.13b*). The difference between anodic and cathodic current density is plotted concerning scan rate (v), the slope of graph (*Figure 5.13c*) gives the value of C_{dl}. The C_{dl} has been calculated as shown in equation 7.

$$C_{dl} = \frac{i}{v} \quad (7)$$

Where '*i*' is the current density. The C_{dl} value of Co_2P is found to be 455 µF and ECSA is found to be 13 cm^2.

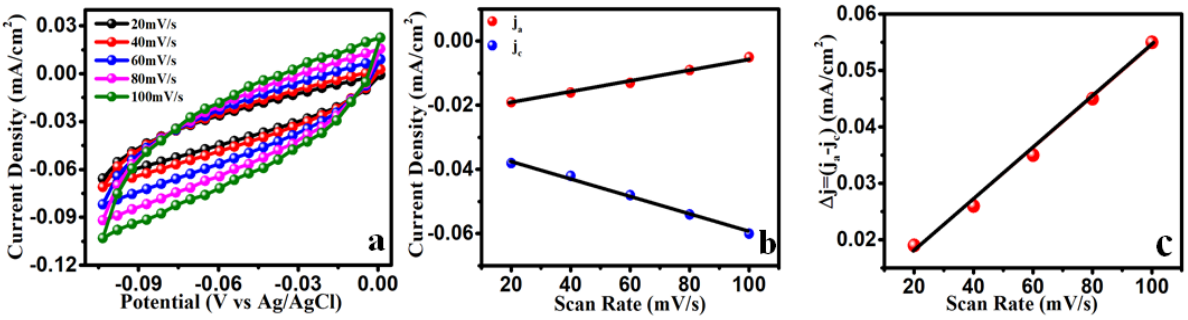

Figure 5.13. (a) CV curves for C_{dl} measurement at different scan rates (b-c) capacitive current at -0.05 V

5.4. Conclusions

In summary, we have successfully synthesized anisotropic cobalt phosphide nanorods from cobalt oxalate rods by slow heating followed by phosphorization. Co_2P nanorods are an efficient electrocatalyst towards HER due to their low overpotential (-117 mV), Tafel slope (74 mV/dec), contact angle, surface charge transfer resistance that results in faster kinetics and shows excellent stability of up to 24 h. The synthesis method described here can be effectively used for fabrication of other metal phosphides which can also be extended for the synthesis of inorganic materials into distinct morphologies with potential applications.

5.5. References

1. Dawood, F., Anda, M. & Shafiullah, G. M. Hydrogen production for energy: An overview. *International Journal of Hydrogen Energy* **45**, 3847–3869 (2020).
2. Thomas, J. M., Edwards, P. P., Dobson, P. J. & Owen, G. P. Decarbonising energy: The developing international activity in hydrogen technologies and fuel cells. *Journal of Energy Chemistry* **51**, 405–415 (2020).
3. Xu, Y., Kraft, M. & Xu, R. Metal-free carbonaceous electrocatalysts and photocatalysts for water splitting. *Chemical Society Reviews* **45**, 3039–3052 (2016).
4. Chi, J. & Yu, H. Water electrolysis based on renewable energy for hydrogen production. *Cuihua Xuebao/Chinese Journal of Catalysis* **39**, 390–394 (2018).
5. Wang, S. *et al.* Molybdenum-Carbide-Modified Nitrogen-Doped Carbon Vesicle

Encapsulating Nickel Nanoparticles: A Highly Efficient, Low-Cost Catalyst for Hydrogen Evolution Reaction. *J. Am. Chem. Soc.* **137**, 15753–15759 (2015).

6. Xia, Z. Hydrogen evolution: Guiding principles. *Nature Energy* **1**, 1–2 (2016).
7. Huang, Z. F. *et al.* Hollow Cobalt-Based Bimetallic Sulfide Polyhedra for Efficient All-pH-Value Electrochemical and Photocatalytic Hydrogen Evolution. *J. Am. Chem. Soc.* **138**, 1359–1365 (2016).
8. Shao, Q., Wang, P., Zhu, T. & Huang, X. Low Dimensional Platinum-Based Bimetallic Nanostructures for Advanced Catalysis. *Acc. Chem. Res.* **52**, 3384–3396 (2019).
9. Xu, H., Shang, H., Wang, C. & Du, Y. Ultrafine Pt-Based Nanowires for Advanced Catalysis. *Adv. Funct. Mater.* **30**, 2000793 (2020).
10. Huang, B. *et al.* Ru@Pt/C core-shell catalyst for SO_2 electrocatalytic oxidation in electrochemical Bunsen reaction. *Electrochim. Acta* **331**, 135315 (2020).
11. Alinezhad, A. *et al.* Direct Growth of Highly Strained Pt Islands on Branched Ni Nanoparticles for Improved Hydrogen Evolution Reaction Activity. *J. Am. Chem. Soc.* **141**, 16202–16207 (2019).
12. Liu, X. *et al.* Hierarchical Bimetallic Ni-Co-P Microflowers with Ultrathin Nanosheet Arrays for Efficient Hydrogen Evolution Reaction over All pH Values. *ACS Appl. Mater. Interfaces* **11**, 42233–42242 (2019).
13. Zhao, J. *et al.* Construction of the Ni_2P/MOP heterostructure as a high-performance cocatalyst for visible-light-driven hydrogen production. *ACS Appl. Energy Mater.* **3**, 10910–10919 (2020).
14. Wu, Z. *et al.* Interface Engineering of MoS_2 for Electrocatalytic Performance Optimization for Hydrogen Generation via Urea Electrolysis. *ACS Sustain. Chem. Eng.* **7**, 16577–16584 (2019).
15. Dou, S. *et al.* Large Interlayer Spacing of Few-Layered Cobalt-Tin-Based Sulfide Providing Superior Sodium Storage. *ACS Appl. Mater. Interfaces* **12**, 41546–41556 (2020).
16. Zhao, Y. *et al.* Self-Templating Strategies for Transition Metal Sulfide Nanoboxes as Robust Bifunctional Electrocatalysts. *Chem. Mater.* **32**, 1371–1383 (2020).
17. Liu, Y. & Mustain, W. E. Evaluation of tungsten carbide as the electrocatalyst support

for platinum hydrogen evolution/oxidation catalysts. *Int. J. Hydrogen Energy* **37**, 8929–8938 (2012).

18. Choi, J. S., Bugli, G. & Djéga-Mariadassou, G. Influence of the degree of carburization on the density of sites and hydrogenating activity of molybdenum carbides. *J. Catal.* **193**, 238–247 (2000).
19. Mei, X., Li, C., Lam, F. L. Y. & Hu, X. Nanosheet-like Ternary Metal Sulfide as a pH-Universal Catalyst for the Hydrogen Evolution Reaction. *ACS Appl. Energy Mater.* **3**, 6172–6179 (2020).
20. Chen, W.-F. *et al.* Hydrogen-Evolution Catalysts Based on Non-Noble Metal Nickel-Molybdenum Nitride Nanosheets. *Angew. Chemie Int. Ed.* **51**, 6131–6135 (2012).
21. Yu, X. *et al.* 'superaerophobic' Nickel Phosphide Nanoarray Catalyst for Efficient Hydrogen Evolution at Ultrahigh Current Densities. *J. Am. Chem. Soc.* **141**, 7537–7543 (2019).
22. Su, L. *et al.* Surface reconstruction of cobalt phosphide nanosheets by electrochemical activation for enhanced hydrogen evolution in alkaline solution. *Chem. Sci.* **10**, 2019–2024 (2019).
23. Zhang, X. *et al.* Molybdenum Phosphide/Carbon Nanotube Hybrids as pH-Universal Electrocatalysts for Hydrogen Evolution Reaction. *Adv. Funct. Mater.* **28**, 1706523 (2018).
24. Xu, K., Fu, X., Li, H. & Peng, Z. A novel composite of network-like tungsten phosphide nanostructures grown on carbon fibers with enhanced electrocatalytic hydrogen evolution efficiency. *Appl. Surf. Sci.* **456**, 230–237 (2018).
25. Mohiuddin, M. *et al.* Synthesis of two-dimensional hematite and iron phosphide for hydrogen evolution. *J. Mater. Chem. A* **8**, 2789–2797 (2020).
26. Popczun, E. J., Read, C. G., Roske, C. W., Lewis, N. S. & Schaak, R. E. Highly Active Electrocatalysis of the Hydrogen Evolution Reaction by Cobalt Phosphide Nanoparticles. *Angew. Chemie* **126**, 5531–5534 (2014).
27. Popczun, E. J. *et al.* Highly branched cobalt phosphide nanostructures for hydrogen-evolution electrocatalysis. *J. Mater. Chem. A* **3**, 5420–5425 (2015).
28. Cao, H. *et al.* Flower-like CoP microballs assembled with (002) facet nanowires via precursor route: Efficient electrocatalysts for hydrogen and oxygen evolution.

Electrochim. Acta **259**, 830–840 (2018).

29. Wang, H., Li, Y., Wang, R., He, B. & Gong, Y. Metal-organic-framework template-derived hierarchical porous CoP arrays for energy-saving overall water splitting. *Electrochim. Acta* **284**, 504–512 (2018).
30. Li, Z. *et al.* Synthesis of hollow cobalt phosphide nanocrystals with ultrathin shells anchored on reduced graphene oxide as an electrocatalyst toward hydrogen evolution. *Appl. Surf. Sci.* **506**, 144975 (2020).
31. Du, X. *et al.* Vanadium doped cobalt phosphide nanorods array as a bifunctional electrode catalyst for efficient and stable overall water splitting. *Int. J. Hydrogen Energy* **46**, 599–608 (2021).
32. Du, B. *et al.* Direct growth of nickel-doped cobalt phosphide nanowire cluster on carbon cloth for efficient hydrogen evolution reaction. *Electrochem. commun.* **127**, 107051 (2021).
33. Wang, X. *et al.* Gold-Incorporated Cobalt Phosphide Nanoparticles on Nitrogen-Doped Carbon for Enhanced Hydrogen Evolution Electrocatalysis. *ACS Appl. Mater. Interfaces* **12**, 16548–16556 (2020).
34. Li, L., Li, X., Ai, L. & Jiang, J. MOF-derived nanostructured cobalt phosphide assemblies for efficient hydrogen evolution reaction. *RSC Adv.* **5**, 90265–90271 (2015).
35. Yadav, K. K. *et al.* Synthesis of zirconium diboride and its application in the protection of stainless steel surface in harsh environment. *J. Solid State Electrochem.* (2019). doi:10.1007/s10008-019-04408-0
36. Ranjan, R. *et al.* Controlling the size, morphology, and aspect ratio of nanostructures using reverse micelles: A case study of copper oxalate monohydrate. *Langmuir* **25**, 6469–6475 (2009).
37. Sharma, S., Garg, N., Ramanujachary, K. V., Lofland, S. E. & Ganguli, A. K. Design of anisotropic Co_3O_4 nanostructures: Control of particle size, assembly, and aspect ratio. *Cryst. Growth Des.* **12**, 4202–4210 (2012).
38. Liang, F. *et al.* Microwave-assisted hydrothermal synthesis of cobalt phosphide nanostructures for advanced supercapacitor electrodes. *CrystEngComm* **20**, 2413–2420 (2018).

39. Shi, Y. & Zhang, B. Recent advances in transition metal phosphide nanomaterials: Synthesis and applications in hydrogen evolution reaction. *Chemical Society Reviews* **45**, 1529–1541 (2016).
40. Wang, D., Wang, Q. & Wang, T. Morphology-controllable synthesis of cobalt oxalates and their conversion to mesoporous Co_3O_4 nanostructures for application in supercapacitors. *Inorg. Chem.* **50**, 6482–6492 (2011).
41. Callejas, J. F., Read, C. G., Popczun, E. J., McEnaney, J. M. & Schaak, R. E. Nanostructured Co2P electrocatalyst for the hydrogen evolution reaction and direct comparison with morphologically equivalent CoP. *Chem. Mater.* **27**, 3769–3774 (2015).
42. Huang, Z. *et al.* Cobalt phosphide nanorods as an efficient electrocatalyst for the hydrogen evolution reaction. *Nano Energy* **9**, 373–382 (2014).
43. Ali, M., Anjum, R., Datt Bhatt, M., Lee, M. H. & Lee, J. S. Sulfur-Doped Dicobalt Phosphide Outperforming Precious Metals as a Bifunctional Electrocatalyst for Alkaline Water Electrolysis. *Chem. Mater* **30**, 8861–8870 (2018).
44. Ma, J. *et al.* Polyaniline Derived N-Doped Carbon-Coated Cobalt Phosphide Nanoparticles Deposited on N-Doped Graphene as an Efficient Electrocatalyst for Hydrogen Evolution Reaction. *Small* **14**, 1702895 (2018).
45. Wang, T. *et al.* An efficient Co_3S_4/CoP hybrid catalyst for electrocatalytic hydrogen evolution. *Sci. Rep.* **7**, 1–9 (2017).
46. Tian, J., Liu, Q., Cheng, N., Asiri, A. M. & Sun, X. Self-supported Cu3P nanowire arrays as an integrated high-performance three-dimensional cathode for generating hydrogen from water. *Angew. Chemie - Int. Ed.* **53**, 9577–9581 (2014).
47. Pan, Y., Lin, Y., Chen, Y., Liu, Y. & Liu, C. Cobalt phosphide-based electrocatalysts: Synthesis and phase catalytic activity comparison for hydrogen evolution. *J. Mater. Chem. A* **4**, 4745–4754 (2016).
48. Irshad, A. & Munichandraiah, N. Electrodeposited Nickel-Cobalt-Sulfide Catalyst for the Hydrogen Evolution Reaction. *ACS Appl. Mater. Interfaces* **9**, 19746–19755 (2017).
49. Wu, C., Yang, Y., Dong, D., Zhang, Y. & Li, J. In Situ Coupling of CoP Polyhedrons and Carbon Nanotubes as Highly Efficient Hydrogen Evolution Reaction

Electrocatalyst. *Small* **13**, (2017).

50. Tian, J., Liu, Q., Cheng, N., Asiri, A. M. & Sun, X. Self-Supported Cu 3 P Nanowire Arrays as an Integrated High-Performance Three-Dimensional Cathode for Generating Hydrogen from Water . *Angew. Chemie* **126**, 9731–9735 (2014).
51. Tian, L., Yan, X., Chen, X., Liu, L. & Chen, X. One-pot, large-scale, simple synthesis of Co:XP nanocatalysts for electrochemical hydrogen evolution. *J. Mater. Chem. A* **4**, 13011–13016 (2016).
52. Wang, C. *et al.* Alternative synthesis of cobalt monophosphide@C core-shell nanocables for electrochemical hydrogen production. *J. Power Sources* **286**, 464–469 (2015).
53. Liu, M. & Li, J. Cobalt Phosphide Hollow Polyhedron as Efficient Bifunctional Electrocatalysts for the Evolution Reaction of Hydrogen and Oxygen. *ACS Appl. Mater. Interfaces* **8**, 2158–2165 (2016).
54. Fei, H. *et al.* Cobalt nanoparticles embedded in nitrogen-doped carbon for the hydrogen evolution reaction. *ACS Appl. Mater. Interfaces* **7**, 8083–8087 (2015).
55. Pu, Z. *et al.* Phytic acid-derivative transition metal phosphides encapsulated in N,P-codoped carbon: An efficient and durable hydrogen evolution electrocatalyst in a wide pH range. *Nanoscale* **9**, 3555–3560 (2017).
56. Amaral, L., Cardoso, D. S. P., Šljukić, B., Santos, D. M. F. & Sequeira, C. A. C. Room Temperature Ionic Liquids as Electrolyte Additives for the HER in Alkaline Media. *J. Electrochem. Soc.* **164**, F427–F432 (2017).
57. Zhou, Z. *et al.* Hydrogen evolution reaction activity of nickel phosphide is highly sensitive to electrolyte pH. *J. Mater. Chem. A* **5**, 20390–20397 (2017).

Chapter 6

Synthesis of Iron phosphide nanoparticles and their investigation towards hydrogen generation

6.1. Introduction

Global energy crisis has led to the advent of alternative non carbonaceous and sustainable energy sources so as to mitigate the dependency of fossil fuels. Hydrogen as an efficient, clean and energy dense carrier has emerged as savior to potential energy catastrophe. Despite being the most abundant element Hydrogen has to be produced from various sources. Traditionally Hydrogen can be obtained by Methanol steam reforming[1] and gasification of coal.[2] Amongst the diverse methods, electrocatalytic water splitting has proved to be one of the most mature technologies for Hydrogen generation.[3] Ideally water electrolyzers should possess significant activity and stability towards water splitting reaction, which suffers from the bottleneck of poor kinetics of Oxygen Evolution Reaction (OER) taking place at anode due to transfer of four electron. For efficient Hydrogen evolution reaction (HER) there is always a search of electrocatalysts which have low overpotential and high current density. Platinum, Ruthenium and Iridium are important state-of-the-art materials for HER but their commercial and industrial applications are unsubstantiated due to their high cost and scarce abundance[4]. Although many non-noble metal catalysts like selenides[5], Carbides[6], Chalcogenides[7,8], Nitrides[9], Oxides[10,11], Sulfides[12] and phosphides[13–15] have been widely used as they have rich abundance, lesser cost and excellent catalytic activity. The main flaw remains significant in terms of abundant scaling up of catalyst besides various electrochemical parameters like overpotential for HER. Iron Phosphide being the phosphide of most abundant and inexpensive metal Iron accounts for its ease in large scale production.[16] Among all 3d-transition-metal-based phosphides, iron phosphides are especially attractive because Fe comprises 5% of the Earth's crust and is the most abundant transition metal. FeP nanosheets which were having an overpotential of 250 mV was prepared by Zhangs group through anion exchange reaction between organic-inorganic hybrid with P ions.[17] Callejas' et al. synthesized FeP by decomposition of $Fe(CO)_5$ in a mixture of oleylamine and 1-octadecene and then phosphorylation with triocylphosphine.[18] Most of these methods are labour intensive and not so cost effective as well as involve complex organic reagents. So, there is a pressing need to design an economic and simple process for synthesis route for HER electrocatalysts. The synthesis of iron phosphide nanoparticles has been achieved by a one-step solid-state reaction route by phosphorizing α-Fe_2O_3. The as synthesized nanoparticles of iron phosphide show excellent catalytic activity towards HER in acidic and

basic medium. The FeP nanoparticles need an low overpotantial of 63 mV and 121 mV to reach the current density of 10 mA/cm^2 and good stability in both acidic and basic medium.

6.2. Experimental

Material: Ferrous sulphate (FeSO4, 99 % CDH). Sodium hypophosphite monohydrate (NaH_2PO_2, 99% Sigma Aldrich), Sulfuric acid (H_2SO_4, 98% Merck), Cetyl-tri-methyl ammonium bromide (CTAB, 99 % CDH), Cobalt nitrate hexahydrate (Co $(NO_3)_2.6H_2O$, 98 % Merck), methanol (CH_3OH, 99 % CDH), 5 % Pt/C (5 % platinum on carbon, Sigma-Aldrich) and Ammonium oxalate ($(NH_4)_2C_2O_4$, 99 %, Merck) were used as received. The detailed experimental method has been discussed in supporting information.

Synthesis of iron oxalate and iron oxide

In this experiment, 0.1M $FeCl_2$ and $(NH4)_2C_2O_4$ were dissolved in a 100 ml of water, then 1% of CTAB was added in the above solution and stirred for 7 days. The precipitates were collected and washed with a mixture of chloroform and methanol (1:1). The precipitates were dried in a vacuum oven at 70 ºC overnight. The as obtained product was subsequently calcined at 250 °C to form iron oxide.

Synthesis of iron phosphide

For synthesis, iron oxide and NaH_2PO_2 were taken in 1:5 w/w ratio and grinded in a mortar pastel and calcined at 350 ºC in presence of Ar atmosphere for 6 h. The as obtained product was washed with distilled water to remove impurities from the product and dried in a vacuum oven at 70 ºC overnight.

Preparation of iron phosphide electrode

To fabricate, dispersion of 5 mg of iron phosphide is taken in a 200 ul of ethanol and then ultra-sonicated for 30 minutes. After that nafion as a binder was added to the above dispersion and sonicated for another 15 minutes. The prepared dispersion (10 ul) was drop casted on graphite sheet and dried in vacuum for 2 h.

6.2.1. Characterization

Bruker D8 advance diffractometer is used to determine the phase and structure of the materials which is equipped with Cu-$K_{\alpha 1}$ (λ= 1.54Å) source. The shape and size of all the

materials have been studied using Transmission electron microscope (TEM, JEOL JEM-2100). The compositional studies of iron phosphide were measured by EDX (energy dispersive X-ray spectroscopy) analyzer coupled with TEM JEOL JEM-2100. Electrochemical performance of all the materials has been evaluated on the Metrohm PGSTAT-30 Autolab workstation. Contact angle studies were performed using drop analyzer DSA25-KRUSS GmbH. Post electrochemical stability studies for the leaching of catalyst in the electrolyte is carried out using Agilent -7900 ICP-MS spectrometry, X-ray photoelectron spectroscopy was performed on Thermoscientific K-alpha X-ray Photoelectron Spectrometer (XPS) System equipped with Al as a source.

6.2.2. Electrochemical measurements

Electrochemical performance of all the materials has been measured on a three-electrode system present in the Metrohm PGSTAT-30 Auto lab workstation. In this experiment, all studies were carried out in 50 ml of 0.5 M H_2SO_4 and 1 M KOH. For counter electrode, Graphite rod was used, however for working electrode cobalt phosphide coated graphite sheet (0.5*1 cm^2) was used. Apart from that Ag/AgCl reference electrode has been used in the present experiment. For HER measurement, linear sweep voltammetry (LSV) studies of the prepared materials have been done at a scan rate of 5 mV/sec in the potential window of 0 V to - 1 V vs Ag/AgCl. To measure intrinsic resistance of all materials electrochemical impedance spectroscopy (EIS) was done at potential of -0.4 V vs Ag/AgCl in the frequency range of 0.01 Hz to 100 kHz. The potentials were converted using Nernst Equation with respect to RHE [19].All the measurements were also carried out for Pt/C to compare the electrochemical activity of Co_2P with that of state of art material.

6.3. Result and Discussion

In the present chapter, we have done the synthesis of iron phosphide nanoparticles and further utilized as electrocatalyst for hydrogen evolution. The above work has been performed in three steps. The first step deals with the synthesis of ferrous oxalate by micellization. In the second step, the ferrous oxalate was converted into iron oxide which is further annealed with phosphorous source to form iron phosphide. In the final step, the synthesized iron phosphide has been utilized as an electrocatalyst efficiently and its mechanistic insights have been explored. The yellow product was formed after the

micellization of $FeCl_2.4H_2O$ with that of di- ammonium oxalate which was characterized by PXRD. The PXRD (*Figure 6.1)* shows the Bragg's reflection at 2θ of 18.3˚, 23.2 ˚, 28.5˚, 34.4˚, 37.9˚, 42.8˚, 45.1˚, 48.4˚. All the diffraction Peaks corresponds to orthorhombic Ferrous oxalate (JCPDS card no. 00-022-0635).

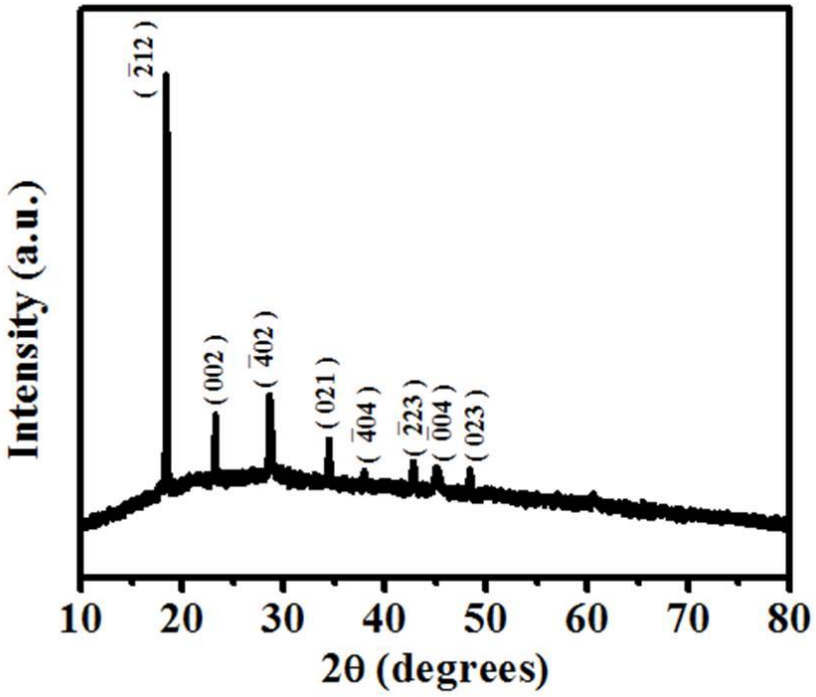

Figure 6.1. Powder X-ray diffraction pattern of $FeC_2O_4.2H_2O$

The as synthesized ferrous oxalate was calcined at 250 ºC to form iron oxide which was further confirmed by the PXRD. The diffraction peaks at 2θ of 24.2˚, 33.2˚, 35.6˚, 40.9˚, 49.5˚, 54.1˚, 62.4˚, 64.1˚ corresponds to (-212), (002), (-402), (021), (-404), (-223), (-004) and (023) plane and matches with iron (II) oxide as shown in *Figure 6.2a* (JCPDS card no. 00-002-0919). The morphological and compositional studies were carried out using TEM and TEM-EDAX. TEM micrograph (*Figure 6.2b, c*) shows the formation of dandelion like morphology of the iron oxide having size 0f 120 nm. TEM-EDAX confirms existence of Fe and O elements in the sample (*Figure 6.2d).* The as synthesized iron oxide is further annealed with phosphorous source at 350 ºC in an inert atmosphere to form iron phosphide. The black product formed after annealing was investigated using PXRD and TEM.

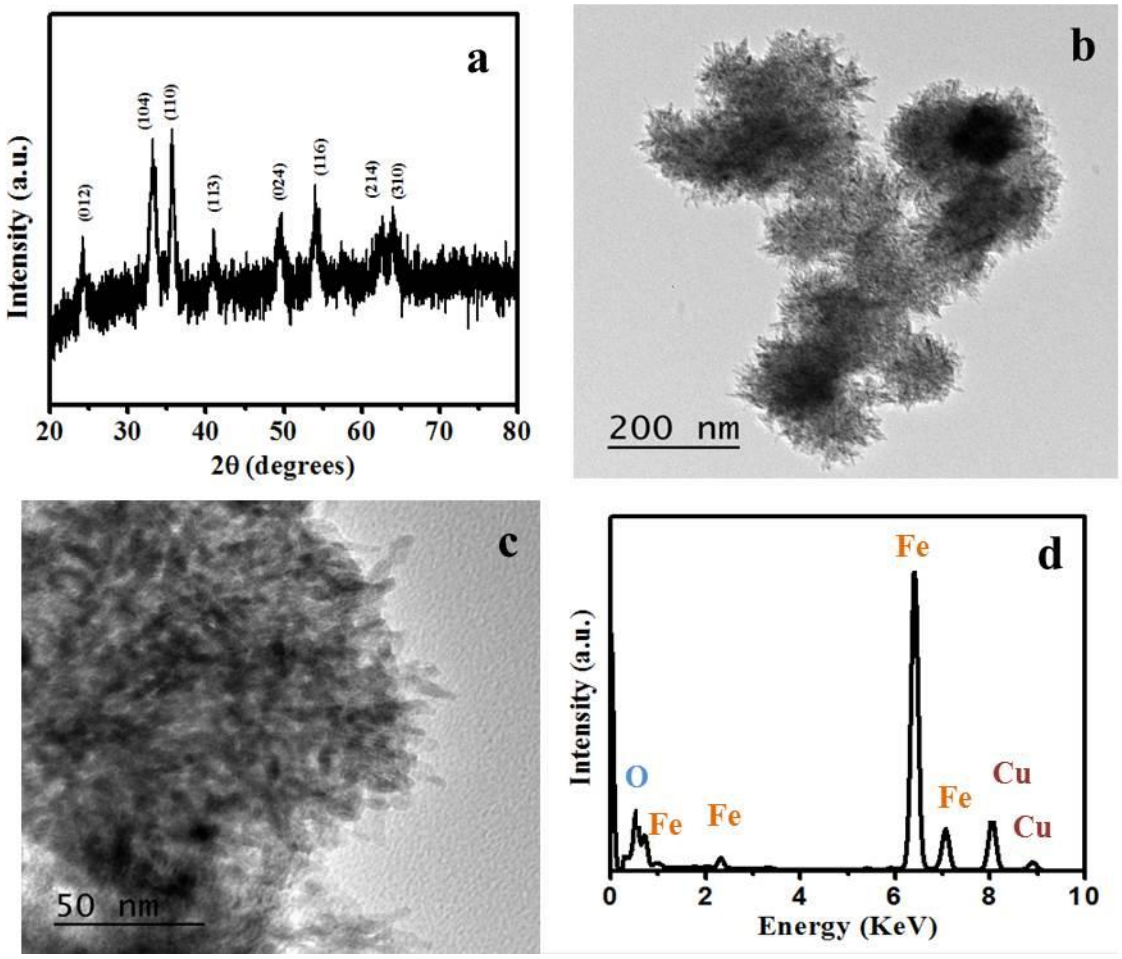

Figure 6.2. a) Powder X-ray diffraction pattern b), c) TEM image and d) TEM –EDAX of Fe_2O_3

The PXRD (*Figure 6.3a)* shows the Bragg's reflection at 020, -206, 112, 021, 102, -206, 002, -425, -313, 011, 211 and -311 which corresponds to orthorhombic phase of FeP (JCPDS no. 03-065-2595) having space group Pnma(62). The elemental and morphological studies were carried out using TEM and FESEM. TEM micrographs (*Figure 6.3b, c)* show the formation of sheet like structures having size ~5 µm which is made up of nanoparticles having size of 100 nm. Further High-resolution TEM is done for the structural confirmation which shows interplanar distance of 0.20 nm that corresponds to (112) crystal plane of the FeP as depicted in *Figure 6.3d*. Additionally, the FESEM studies were also carried out and FESEM micrograph (*Figure 6.4a*) shows the formation of sheets like structure of size up to 5 µm and the elemental mapping has been done to check the uniform distribution of iron and phosphorous on the iron phosphide nanoparticles as shown in *Figure 6.4b-d*.

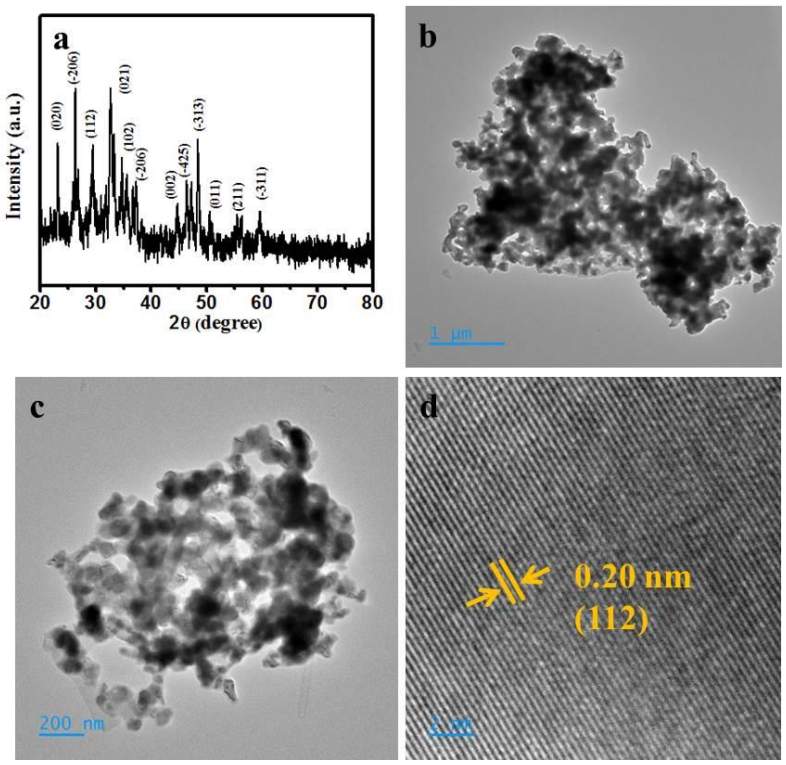

Figure 6.3. a) Powder X-ray diffraction pattern b), c) TEM image and d) HRTEM image of FeP nanoparticles

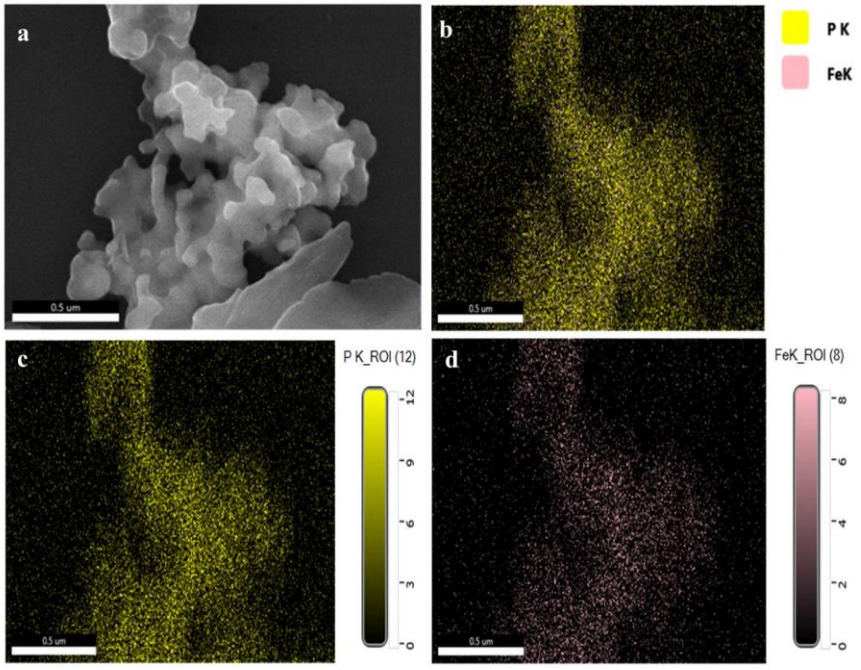

Figure 6.4. a) FESEM image of FeP particles and (b-d) elemental mapping of Fe and P

To further analyze the chemical state and compositional studies XPS studies were carried out on the sample. The XPS survey (*Figure 6.5a)* scan confirms the presence of Fe and P in the sample. To evaluate the binding state of elements High Resolution XPS studies were done. In Fe 2p narrow scan (*Figure 6.5b)* two peaks are observed at 707 eV and 720 eV corresponds to Fe-P bond in FeP. The peaks observed at 710 eV and 723 eV corresponds to Fe^{2+} which comes due to the surface oxidation of sample. In P 2p narrow scan, two peaks were observed at 129.4 eV and 134.3 eV as depicted in *Figure 6.5c*. The peak at 129.4 eV attributed to $2p_{3/2}$ and 130.3 eV attributed to $2p_{1/2}$ respectively, which corresponds to Fe-P bond in FeP. The peak at 134.2 eV ascribed to oxidized phosphorous (PO_4^{3-}) species on the surface of the sample under air atmosphere. The binding energy of Fe 2p (707 eV) is slightly shifts towards positive as that of Fe metallic peak (706.8) which shows that there is some charge on $Fe^{\delta+}$ ($0<\delta>2$) in FeP. In BE of P 2p (129.4 eV) there is small negative shift from that of elemental P (130.3 eV) which shows there is partially negative charge on $P^{\delta-}$ in FeP. This negative charge is due to partial transfer of electrons from Fe to P. Therefore, positively metallic site Fe (δ^+) act as the hydride-acceptor and negatively P site (δ^-) act as proton-acceptor centres respectively to expedite the HER.

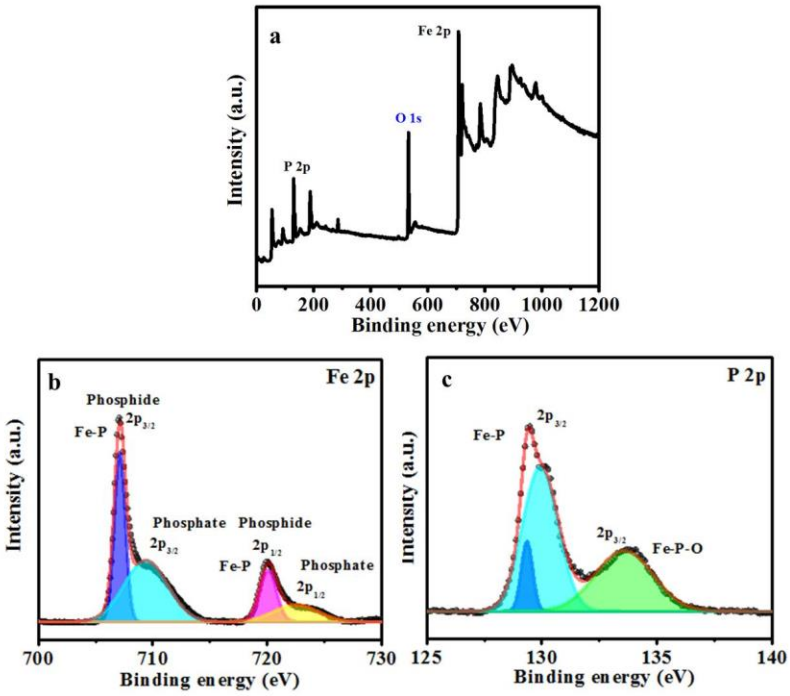

Figure 6.5. High-resolution XPS spectra of as synthesized FeP nanoparticles a) Fe 2p and b) P 2p

6.3.1. Hydrogen evolution studies in acidic media

The HER performance of all the prepared samples were examined in 0.5 M H_2SO_4. LSV curves of all prepared electrodes shown in *Figure 6.6a*. To compare our results with that of state of art material, all studies are carried out with 5% Pt-C. The graphite sheet is used as a substrate for the preparation of working electrode. The graphite sheet shows negligible HER activity as the current density is very low in case of bare graphite. The state of art Pt-C shows low overpotential of 27 mV to reach the benchmark of 10 mA/cm^2 whereas FeP nanoparticles shows overpotential of 48 mV to reach the benchmark. The Fe_2O_3 and FeC_2O_4 show a very high overpotential of 786 mV to reach 5 mA/cm^2 and 756 mV to reach 10 mA/cm^2 current density respectively. Among all the materials FeP shows a high activity towards the HER due to its low overpotential as compared to others. Further to check the kinetics, the tafel slope obtained from corresponding LSV curves are shown in *Figure 6.6b*. The tafel slope of Pt/C, FeP nanoparticless, Fe_2O_3, FeC_2O_4 and bare graphite are 48, 57, 239, 171 and 353 mV/dec respectively. The low tafel slope of FeP nanoparticelss shows its higher activity and kinetic towards HER than that of other materials. Mainly, the reaction takes place in three steps as follows:

$$E + H_3O^+ + e^- \rightarrow E - H_{ads} + H_2O \qquad \text{Volmer Step} \qquad 6.1$$

$$E - H_{ads} + H_3O^+ + e^- \rightarrow H_2 + H_2O \qquad \text{Heyrovsky Step} \qquad 6.2$$

$$2E - H_{ads} \rightarrow 2E + H_2 \qquad \text{Tafel Step} \qquad 6.3$$

The low tafel slope value of FeP shows it follows Volmer-Heyrovsky mechanism to carry out the reaction. Additionally, we have also performed electrochemical impedance spectroscopy (EIS) @ 0.1 V vs RHE. The Nyquist plot as shown in *Figure 6.6c*, It has been observed that FeP the FeP shows the lowest charge transfer resistance value (R_{ct}= 4.5 ohm) as compare to that of Fe_2O_3, FeC_2O_4 and bare graphite which show high charge resistance 922, 3202 and 3004 Ohm. The low value Rct value of FeP that there is an easy flow of electron between electrolyte and electrode during electrochemical reaction. The low Rct value of FeP nanoparticles make it more efficient electrocatalyst towards HER.

The durability of the catalyst is very crucial factor for electrocatalyts for practical application. To check the durability of the catalyst chronoamperometric studies were done at overpotential of 100 mV. The chronoamperometric studies show that FeP nanoparticles retains the current density of 20 mA/cm^2 upto 20 h in acidic media as shown in *Figure 6.6d*.

Further the stability of the catalyst was tested by performing the ICP-MS of electrolyte after stability studies. The ICP-MS shows that presence of 10 ppb of Fe in the solution which confirms its robustness in acidic medium.

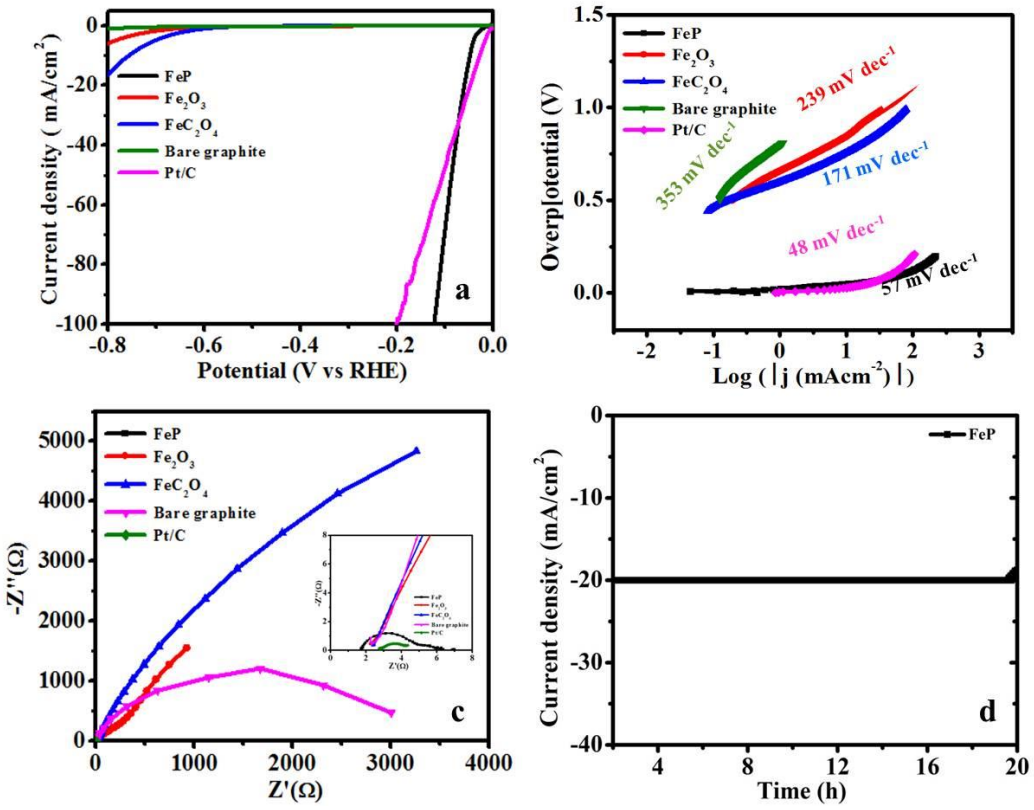

Figure 6.6. a) LSV curves, b) Tafel slope, c) EIS studies of FeP nanoparticels, Pt/C, FeC_2O_4, Fe_2O_3, bare graphite and d) Chronoamperometric studies of FeP nanoparticels in 0.5 H_2SO_4

6.3.2. Hydrogen evolution properties of iron phosphide in basic media

The electrochemical activity of FeP nanoparticles, FeC_2O_4, Fe_2O_3, bare graphite and Pt/C were also evaluated in 1 M KOH. *Figure 6.7a* shows the LSV curves of FeP nanoparticles, FeC_2O_4, Fe_2O_3, bare graphite and Pt/C. As observed, the HER activity of FeP nanoparticles show better activity than FeC_2O_4, Fe_2O_3 and bare graphite. The state of art material Pt/C achieves the current density of 10 mA/cm^2 low overpotential of 55 mV. FeP nanoparticles requires an overpotential of 121 mV as compared to FeC_2O_4, Fe_2O_3 and bare graphite requires 583, 624 and 753 mV to reach the 10 mA/cm^2 current density. Further to check the kinetics of the reaction, The corresponding tafel plot were drawn from the linear region of

polarization curves of FeP nanoparticles, FeC_2O_4, Fe_2O_3, bare graphite and Pt/C are depicted in *Figure 6.7b*. The FeP nanoparticles shows the smallest tafel slope (61 mV/dec) which closer to that of Pt/C (49 mV/dec) as compared to FeC_2O_4 (138 mV/dec), Fe_2O_3 (138 mV/dec), bare graphite (189 mV/dec). The low value of tafel slope suggests the better HER kinetics of FeP nanoparticles. The value of tafel slope suggests that FeP follows volmer Heyrovsky mechanism during the reaction.

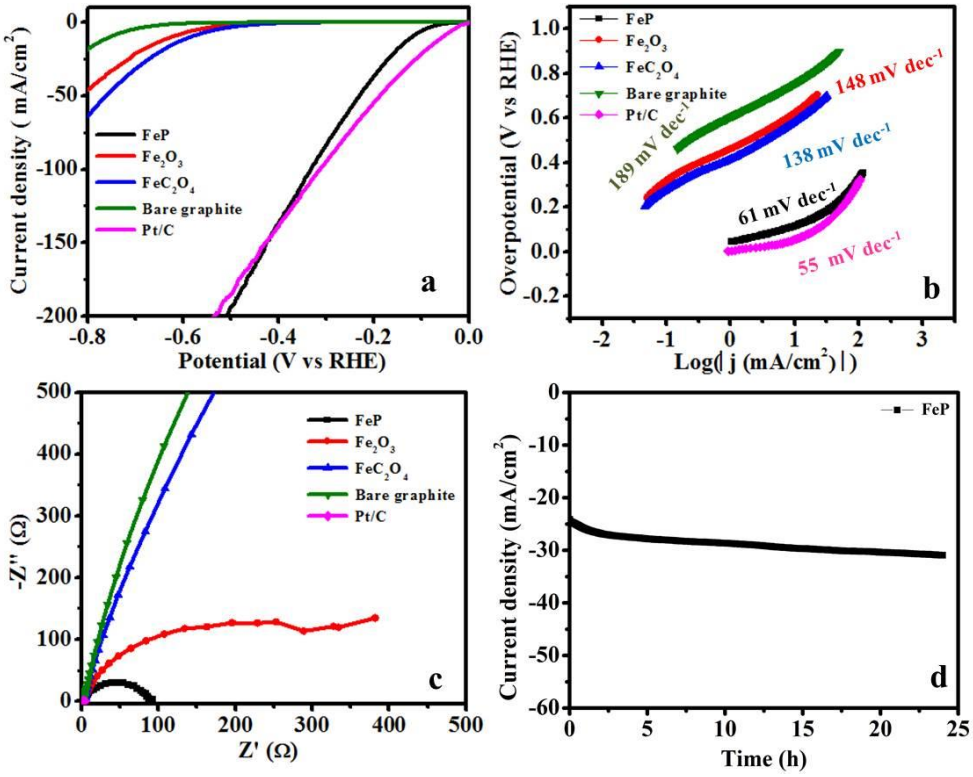

Figure 6.7. a) LSV curves, b) Tafel slope, c) EIS studies of FeP nanoparticles, Pt/C, FeC_2O_4, Fe_2O_3 and bare graphite and d) Chronoamperometric studies of FeP nanoparticles in 1M KOH

To investigate further about charge transfer properties of the catalysts, the electrochemical impedance studies were done @ 1.4 V vs RHE. . The Nyquist plot of the FeP nanoparticles shows smaller charge transfer resistance than that of FeC_2O_4, Fe_2O_3 and bare graphite (*Figure 6.7c)*. The charge transfer resistance (R_{ct}) in FeP nanoparticles is 92 ohm which is lower than that of FeC_2O_4 (1533 ohm), Fe_2O_3 (288 ohm), and bare graphite (1870 ohm) which suggests a faster charge-transfer capacity of FeP during the HER process. The overall result of LSV, Tafel slope and EIS measurements indicate that FeP has the best

electrocatalytic activity for HER and the trend for OER activity follows the order FeP> FeC_2O_4> Fe_2O_3>Bare graphite. Stability of the catalyst is an important factor for practical application. The chronoamperometric studies were done @ 200 mV overpotential. The FeP nanoparticles shows stability up to 24 h as shown in *Figure 6.7d*.

Table 6.1. Comparison of different iron phosphide electroctalysts towards HER

S.no.	Material	Electrolyte	Current density (j) (mV)	Overpotential (η) (mV)	Tafel slope (mV/dec)	References
1	FeP nanoparticles	0.5 M H_2SO_4	10 20	154 187	65	[20]
2	FeP nanosheets	0.5 M H_2SO_4	10	117	56	[21]
3	FeP nanorods	0.5 M H_2SO_4	10	120	55	[22]
4	FeP nanoparticles	0.5 M H_2SO_4	10	112	64	[23]
5	FeP film	1 M KOH	10	110	60	[24]
		0.5 M H_2SO_4	10	66	55	
6	FeP cubes	1 M KOH	10	140	62	[25]
		0.5 M H_2SO_4	10	110	59	
7	FeP nanoparticles	0.5 M H_2SO_4	10	130	57	[26]
8	FeP	0.5 M H_2SO_4	10	135	78	[27]
9	FeP nanosheets	0.5 M H_2SO_4	10	100	67	[28]
10	FeP/CNT	0.5 M H_2SO_4	10	68	58	[29]
11	FeP nanowires	1 M KOH	10	221	134	[30]
		0.5 M H_2SO_4	10	45	53	
12	FeP nanoparticles	0.5 M H_2SO_4	10	63	57	This work
		1 M KOH	10	121	61	

Further to get insights we have calculated electrochemical surface area by double layer capacitance method (C_{dl}). The higher the Cdl value than higher will be the electrochemical surface area. For this cyclic voltammetry scan were carried out in non- faradaic region as shown in *Figure 6.8a-c*. The FeP nanoparticles shows highest C_{dl} value of 31.5 $mFcm^2$ as compared to that of Fe_2O_3 and FeC_2O_4 which show very less C_{dl} value of 0.4 $mFcm^2$and 0.5 $mFcm^2$ respectively as shown in *Figure 6.8d*. The higher C_{dl} value of FeP nanoparticle suggest that FeP has highest electrochemical surface area as compared to other catalysts. The higher area provides more active sites during electrochemical reaction for HER.

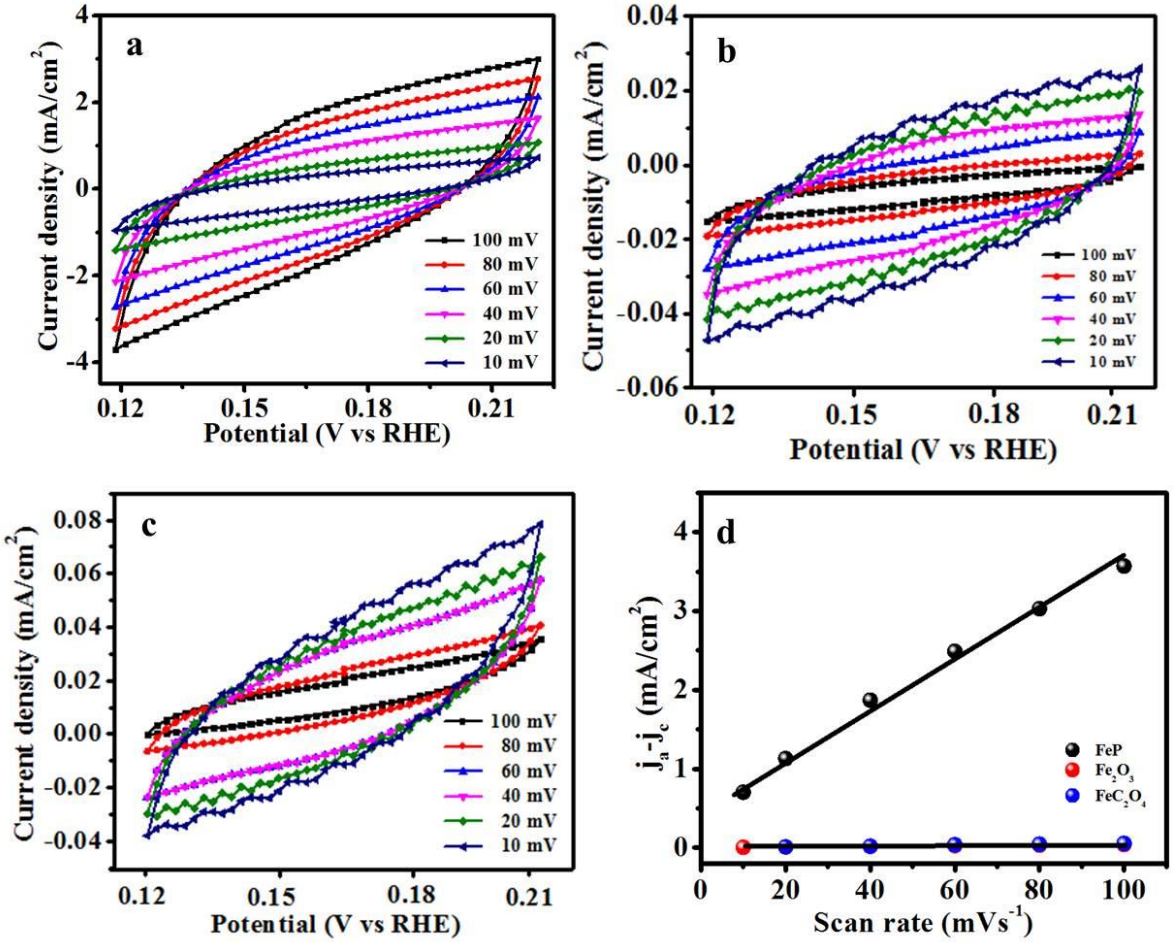

Figure 6.8. CV scans in non-faradaic region with different scan rates a) FeP nanoparticles, b) Fe_2O_3, c) FeC_2O_4 and d) capacitive current at different scan rate

The wettability studies of iron phosphide nanoparticles were done using sessile drop method. The less contact angle of electrolyte with that of surface of elctrocatalyst is a crucial factor. The lower the contact angle with the surface of catalyst more hydrophilic in nature and easier

the electrolyte will diffuse on the surface and higher the contact angle more it will show hydrophobic nature. In here FeP nanoparticles show super hydrophilic nature and contact angle of 0 degree whereas bare graphite shows an contact angle of 83˚ as shown in *Figure 6.9*. This hydrophilic nature of FeP helps in diffusion of electrolyte and helps prevents adhesion of hydrogen bubbles on the surface which further block the active sites during electrochemical reaction.

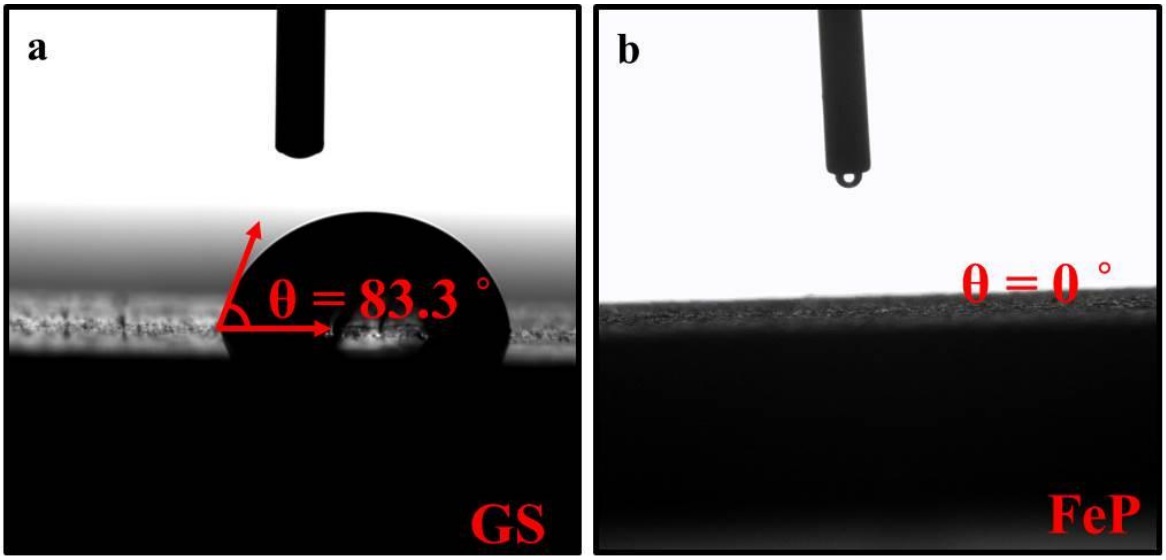

Figure 6.9. Contact angle studies of a) bare graphite and b) FeP nanaoparticles

6.3.3. Post stability characterization of FeP nanoparticles

Post catalytic studies have also been carried to measure the change in the composition of FeP nanoparticles. For this we have performed post electrocatalytic XPS studies on the electrode surface. In High-resolution XPS, after HER studies in 0.5 M H_2SO_4 there is minimum changes have occurred on the surface of catalyst. The peak at 707 eV is remains prominent which shows the active surface of iron phosphide during HER process in acidic medium and there is no phosphate ion involved during electrochemical reaction. The formation of phosphate on the surface gets dissolved in the acidic medium. Therefore, there is no intense peak observed after catalytic studies in acidic medium whereas as after catalytic studies in 1 M KOH the intense peak of phosphate is observed due to formation metal phosphate layer on the catalyst during electrochemical reaction process as shown in *Figure 6.10* and *Figure*

6.11. The intensity of P 2p peak at 134.3 eV is more intense as after the electrocatalytic studies.

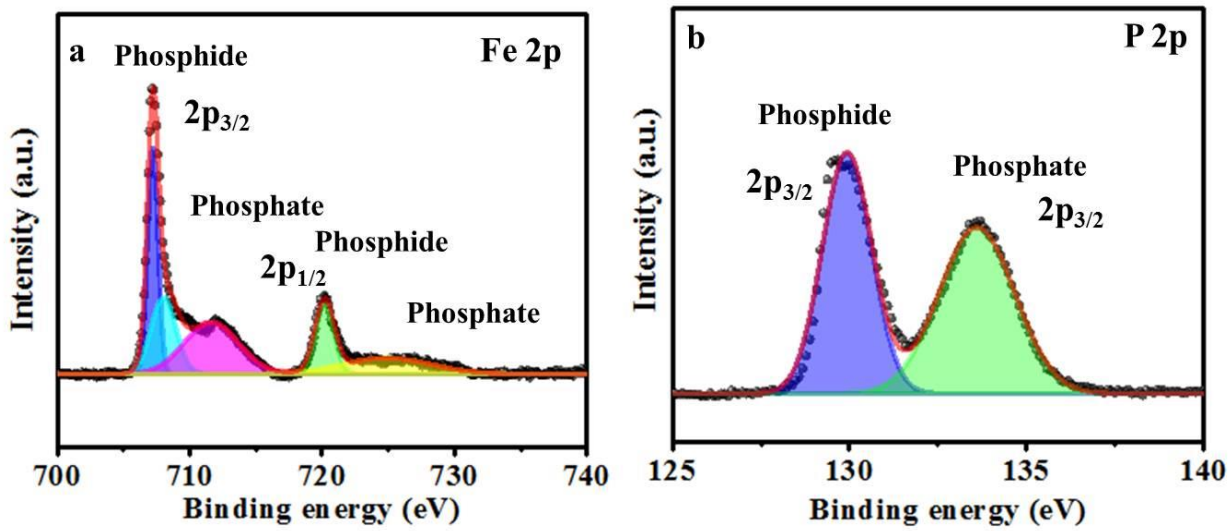

Figure 6.10. Post stability studies of FeP in 0.5 M H_2SO_4

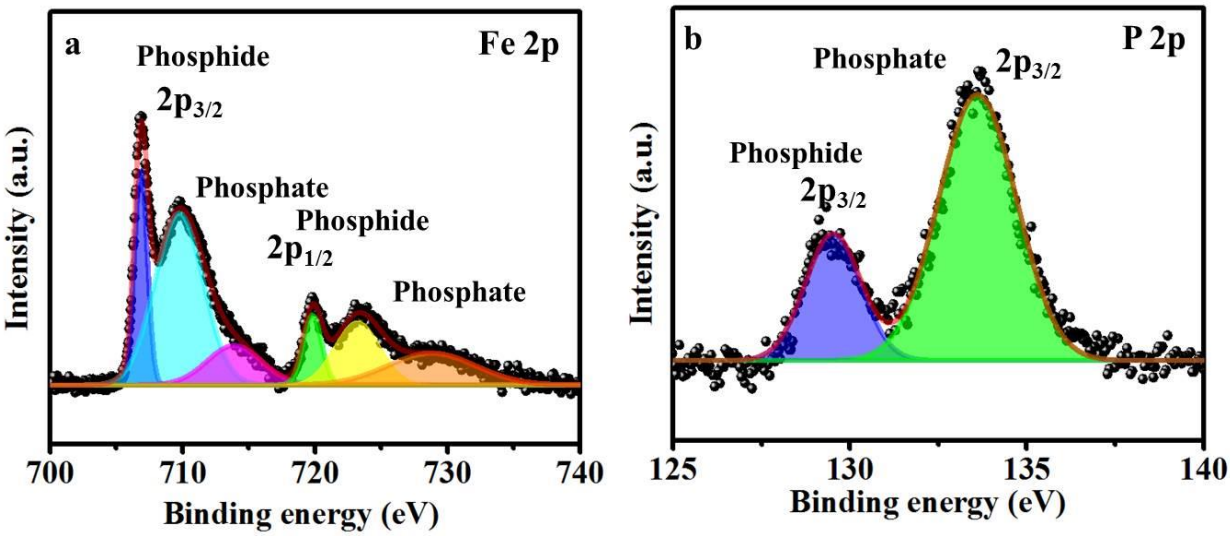

Figure 6.11. Post stability studies of FeP in 1 M KOH

6.4. Conclusions

In this chapter, we have synthesized iron phosphide nanoparticles. FeP nanoparticles are highly active towards hydrogen generation in both acidic (0.5 M H_2SO_4) and basic media (1 M KOH). FeP nanoparticles shows an overpotential of 48 mV and 130 mV to reach 10 mA/cm^2 in acidic and basic medium respectively. The high activity of FeP nanoparticles

attributed to its low charge resistance to increase its intrinsic properties and highly hydrophilic nature that helps in easy diffusion of electrolyte over the surface of electrode. This hydrophilic also prevents adhesion of hydrogen bubbles formed at the surface of electrode. In FeP nanoparticles, positive charge on Fe acts as hydride acceptor and negatively charged P acts a proton acceptor which facilitates HER during electrochemical reaction.

6.5. References

1. Dupont, V., Ross, A. B., Knight, E., Hanley, I. & Twigg, M. V. Production of hydrogen by unmixed steam reforming of methane. *Chem. Eng. Sci.* **63**, 2966–2979 (2008).
2. Stiegel, G. J. & Ramezan, M. Hydrogen from coal gasification: An economical pathway to a sustainable energy future. *Int. J. Coal Geol.* **65**, 173–190 (2006).
3. Jia, H. *et al.* Aerosol-spray metal phosphide microspheres with bifunctional electrocatalytic properties for water splitting. *J. Mater. Chem. A* **6**, 4783–4792 (2018).
4. Peng, X. *et al.* Recent advance and prospectives of electrocatalysts based on transition metal selenides for efficient water splitting. *Nano Energy* **78**, 105234 (2020).
5. Li, C. & Baek, J. B. Recent Advances in Noble Metal (Pt, Ru, and Ir)-Based Electrocatalysts for Efficient Hydrogen Evolution Reaction. *ACS Omega* **5**, 31–40 (2019).
6. Yang, C. *et al.* Ni-Activated Transition Metal Carbides for Efficient Hydrogen Evolution in Acidic and Alkaline Solutions. *Adv. Energy Mater.* **10**, 2002260 (2020).
7. Navakoteswara Rao, V. *et al.* Metal chalcogenide-based core/shell photocatalysts for solar hydrogen production: Recent advances, properties and technology challenges. *J. Hazard. Mater.* **415**, 125588 (2021).
8. Askari, M. B., Salarizadeh, P., Rozati, S. M. & Seifi, M. Two-dimensional transition metal chalcogenide composite/reduced graphene oxide hybrid materials for hydrogen evolution application. *Polyhedron* **162**, 201–206 (2019).
9. Li, J., Zhang, B., Song, Q., Xu, X. & Hou, W. Sulfur and molybdenum Co-doped graphitic carbon nitride as a superior water dissociation electrocatalyst for alkaline hydrogen evolution reaction. *Ceram. Int.* **46**, 14178–14187 (2020).
10. Ling, T. *et al.* Well-Dispersed Nickel- and Zinc-Tailored Electronic Structure of a

Transition Metal Oxide for Highly Active Alkaline Hydrogen Evolution Reaction. *Adv. Mater.* **31**, 1807771 (2019).

11. Cho, Y. Bin, Yu, A., Lee, C., Kim, M. H. & Lee, Y. Fundamental Study of Facile and Stable Hydrogen Evolution Reaction at Electrospun Ir and Ru Mixed Oxide Nanofibers. *ACS Appl. Mater. Interfaces* **10**, 541–549 (2018).
12. Bhat, K. S. & Nagaraja, H. S. Hydrogen evolution reaction at extreme pH conditions of copper sulfide micro-hexagons. *J. Sci. Adv. Mater. Devices* **5**, 361–367 (2020).
13. Pan, Y. *et al.* Monodispersed nickel phosphide nanocrystals with different phases: Synthesis, characterization and electrocatalytic properties for hydrogen evolution. *J. Mater. Chem. A* **3**, 1656–1665 (2015).
14. Mabayoje, O. *et al.* Hydrogen Evolution by Ni_2P Catalysts Derived from Phosphine MOFs. *ACS Appl. Energy Mater.* **3**, 176–183 (2020).
15. Wang, D. *et al.* Hydrogen evolution catalyzed by cobalt-promoted molybdenum phosphide nanoparticles. *Catal. Sci. Technol.* **6**, 1952–1956 (2016).
16. Zhao, R. *et al.* Nanobundles of Iron Phosphide Fabricated by Direct Phosphorization of Metal–Organic Frameworks as an Efficient Hydrogen-Evolving Electrocatalyst. *Chem. – A Eur. J.* **26**, 4001–4006 (2020).
17. Xu, Y., Wu, R., Zhang, J., Shi, Y. & Zhang, B. Anion-exchange synthesis of nanoporous FeP nanosheets as electrocatalysts for hydrogen evolution reaction. *Chem. Commun.* **49**, 6656–6658 (2013).
18. Callejas, J. F. *et al.* Electrocatalytic and photocatalytic hydrogen production from acidic and neutral-pH aqueous solutions using iron phosphide nanoparticles. *ACS Nano* **8**, 11101–11107 (2014).
19. Yadav, K. K. *et al.* Synthesis of zirconium diboride and its application in the protection of stainless steel surface in harsh environment. *J. Solid State Electrochem.* (2019). doi:10.1007/s10008-019-04408-0
20. Tian, L., Yan, X. & Chen, X. Electrochemical Activity of Iron Phosphide Nanoparticles in Hydrogen Evolution Reaction. *ACS Catal.* **6**, 5441–5448 (2016).
21. Mohiuddin, M. *et al.* Synthesis of two-dimensional hematite and iron phosphide for hydrogen evolution. *J. Mater. Chem. A* **8**, 2789–2797 (2020).
22. Du, H., Gu, S., Liu, R. & Li, C. M. Highly active and inexpensive iron phosphide

nanorods electrocatalyst towards hydrogen evolution reaction. *Int. J. Hydrogen Energy* **40**, 14272–14278 (2015).

23. Cho, G., Kim, H., Park, Y. S., Hong, Y. K. & Ha, D. H. Phase transformation of iron phosphide nanoparticles for hydrogen evolution reaction electrocatalysis. *Int. J. Hydrogen Energy* **43**, 11326–11334 (2018).
24. Lu, Z. peng & Sepunaru, L. Electrodeposition of iron phosphide film for hydrogen evolution reaction. *Electrochim. Acta* **363**, 137167 (2020).
25. Shi, J. *et al.* Novel electrocatalyst of nanoporous FeP cubes prepared by fast electrodeposition coupling with acid-etching for efficient hydrogen evolution. *Electrochim. Acta* **329**, 135185 (2020).
26. Pu, Z. *et al.* Phytic acid-derivative transition metal phosphides encapsulated in N,P-codoped carbon: An efficient and durable hydrogen evolution electrocatalyst in a wide pH range. *Nanoscale* **9**, 3555–3560 (2017).
27. Tang, F. *et al.* Potential-driven surface active structure rearrangement over FeP@ NC towards efficient electrocatalytic hydrogen evolution. *pubs.rsc.org*
28. Xu, Y., Wu, R., Zhang, J., Shi, Y. & Zhang, B. Anion-exchange synthesis of nanoporous FeP nanosheets as electrocatalysts for hydrogen evolution reaction. *Chem. Commun.* **49**, 6656–6658 (2013).
29. Wu, F. *et al.* In situ catalytic etching strategy promoted synthesis of carbon nanotube inlaid with ultrasmall fep nanoparticles as efficient electrocatalyst for hydrogen evolution. *ACS Sustain. Chem. Eng.* **7**, 12741–12749 (2019).
30. Lv, C. *et al.* The hierarchical nanowires array of iron phosphide integrated on a carbon fiber paper as an effective electrocatalyst for hydrogen generation. *pubs.rsc.org*

Chapter 7

Conclusion and future prospects

Phosphorous-based materials are great potential towards energy conversion and energy storage technologies like fuel cell, metal-air batteries and electrolysis. The present thesis deals with synthesis of phosphorous-based materials using different process. The as synthesized phosphorous-based materials are further utilized for hydrogen evolution reaction (HER).The thesis is divided into seven chapters.

The first chapter of the thesis explains how energy is a basic social necessity that is essential for promoting economic and civilizing human development. Although there are many diverse energy options, we primarily depend on on fossil fuels, which also raise the issue of climate change because they emit greenhouse gases. So we have to find an alternative renewable energy source which can fulfil our energy demands in the future without affecting environment. In this regard, hydrogen is considered as the best candidate for clean future energy source because of its high energy density and water as byproduct. We also discussed hydrogen production methods without effecting environment. Among all the methods, electrolysis of water is the best method to produce hydrogen at largescale. Apart from that we have also discussed limitations of electrolysis and need of elctrocatalyst for HER. The principle of HER and how can we evaluate electrocatlyst for HER process. We also talk about characterization techniques used for as-synthesized materials for the structure, morphology and their mechanistic aspects.

In the second chapter, ultrathin cobalt cyclotetraphosphate (thickness ~ 1-2 nm) has been synthesized by phosphorization of cobalt oxalate at 350 ºC. The as-obtained product was further utilized as cathode material. Cobalt oxalate precursor has been synthesized via micellar route at room temperature. The as-prepared $Co_2P_4O_{12}$ has been deposited on graphite sheet and used as a working electrode for HER. In comparison with Pt/C (η_{20} = 54 mV), nanosheets of $Co_2P_4O_{12}$ requires 118 mV overpotential to achieve 20 mA/cm^2 current density in 0.5 M H_2SO_4 and almost same current was retained even after 24 h.

In the next chapter, ultrathin nickel cyclotetraphosphate ($Ni_2P_4O_{12}$) nanosheets (thickness ~ 1.5 nm) have been stabilized at low temperature using nickel oxalate nanosheets and diphosphorus pentaoxide as a starting material. The synthesis of nickel oxalate nanosheets (thickness ~5-6 nm) has been done at room temperature using a simple micellar route wherein CTAB has been used as a surfactant. $Ni_2P_4O_{12}$ shows an overpotential of 105 mV

measured at 10 mV/cm^2 current density and small Tafel slope (48 mV/dec). The good catalytic activity of $Ni_2P_4O_{12}$ nanosheets attributes to highly nucleophilic nature of $P_4O_{12}^{4-}$ anion ring which leads to some positive charge on metal ion. Therefore, In $Ni_2P_4O_{12}$ the anion $P_4O_{12}^{4-}$ acts as proton acceptor during HER process. $Ni_2P_4O_{12}$ nanosheets show good stability up to 17 h in acidic medium. The stability $Ni_2P_4O_{12}$ nanosheets are due to polymeric nature of $P_4O_{12}^{4-}$ anion.

In fourth chapter, the catalytic activity of metal cyclotetraphosphate has enhanced by synthesizing bimetallic cyclotetraphophate. The synthesized $CoNiP_4O_{12}$ shows better catalytic activity than $Co_2P_4O_{12}$ and $Ni2P_4O_{12}$. The $CoNiP_4O_{12}$ requires overpotential of 74 mV to attain the current density of 10 mA/cm^2 which is lower than that of $Co_2P_4O_{12}$ and $Ni2P_4O_{12}$. This enhancement in the e catalytic activity of $CoNiP_4O_{12}$ is due to synergistic effect of Co and Ni which intrinsic electron transfer during electrochemical reaction. Further to decrease the overpotential, the composite of $CoNiP_4O_{12}$/rGO was synthesized that shows an overpotential of 41 mV and higher kinetics and lower charge transfer resistance during electrochemical reaction. The higher activity $CoNiP_4O_{12}$/rGO attributes its surface area and increased electrical conductivity which provide more active sites and low charge resistance during HER process.

We have also synthesized Transition metal phosphides (TMPs). TMPs evolved as a fascinating candidate for the electrocatalytic properties owing to their earth abundance and inexpensive nature as compared to expensive and less abundant noble metals. In view of the above, in the present chapter, cobalt phosphide nanorods were synthesized using cobalt oxalate rods. The precursor cobalt oxalate rods were firstly prepared by micellar route at room temperature. Further, phosphorization of cobalt oxalate nanorods has been done at different heating rates. Interestingly, it is observed that cobalt oxalate morphology was retained during its phosphorization to yield cobalt phosphide at a slow heating rate. Pure cobalt phosphide nanorods show good catalytic performance for HER due to its small overpotential (η_{10}) of 117 mV and great stability.

In sixth chapter of thesis, we have synthesized iron phosphide nanoparticles of orthorhombic phase of size ~ 60 nm. FeP nanoparticles are highly active towards hydrogen generation in both acidic (0.5 M H_2SO_4) and basic media (1 M KOH). FeP nanoparticles shows an

overpotential of 48 mV and 130 mV to reach 10 mA/cm^2 in acidic and basic medium respectively. The high activity of FeP nanosheets attributed to its low charge resistance to increase its intrinsic properties, and highly hydrophilic nature that helps in easy diffusion of electrolyte over the surface of electrode. In FeP nanoparticles, positive charge on Fe acts as hydride acceptor and negatively charged P acts a proton acceptor which facilitates HER.

Table 7.1.Comparison of synthesized phosphorous-based materials towards HER in acidic media

Material	Overpotential (mV)	Tafel slope (mV/dec)
$Co_2P_4O_{12}$	92	97
$Ni_2P_4O_{12}$	105	48
$CoNiP_4O_{12}$	74	45
$CoNiP_4O_{12}$/rGO	41	43
Co_2P	117	74
FeP	48	57

In summary here, we have synthesized different phosphorous based materials such as transition metal cycloetraphosphates and transition metal phosphides using different synthesis process and precusors. The as-synthesized phosphorous based material shows the excellent catalytic activity for hydrogen generation. These synthetic procedures can be applied further applied to other metal phosphates and phosphides in the future.

List of Publications

Patents

1. A Process for producing $LaFeMnO_6$ from iron ore and applications thereof , S. Sarkar, M. Jha, K. K. Yadav, S. K. Guchhait, K. Sood, **Ankush**, Patent application number 202131014754

List of Papers (Published and communicated)

1. **Ankush,** K. K.Yadav, S. K. Guchhait, Ritika Wadhwa and Menaka Jha* "Surface phosphorization of nickel oxalate nanosheets to stabilize ultrathin nickel cyclotetraphosphate nanosheets for efficient hydrogen generation", *Mat.l Res. Bull., 2021, 139,* 111275.
2. **Ankush**, Krishna K. Yadav, Sujit Kumar Guchhait, Supriya Rana, Menaka Jha. Excellent hydrogen generation from ultrathin nanosheets of cobalt cyclotetraphosphate. *Mat. Sci. Eng. B,* 2021**,** 265, 114983.
3. **Ankush;** M. M. Devi; S. K. Guchhait, Sureshbabu G. N., M. Sreekanth, N. Kalaiselvi, A. K. Ganguli and Menaka Jha* "Energy Efficient Electrodes for Lithium-ion Batteries: Recovered and Processed from Spent Primary Batteries", *Journal of hazardous material*, 2020, 384, 121112.
4. **Ankush,** Ritika Wadhwa; Sunaina and Menaka Jha* "Mechanistic aspects of cobalt phosphide nanorods derived using cobalt oxalate rods for hydrogen generation" *Materials Science and Engineering: B* (under revision).
5. **Ankush,** Ritika Wadhwa and Menaka Jha* "Promoting the catalytic activity of metal cycloteraphophate for electrochemical hydrogen evolution" (manuscript communicated).
6. **Ankush**; Arushi Arora; Ritika Wadhwa and Menaka Jha* "Synthesis of Iron phosphide nanoparticles and its application towards hydrogen generation" (manuscript communicated).
7. Ritika Wadhwa, **Krishna K. Yadav**, Tanmay Goswami, Ankush, Sujit Kumar Guchhait, Sunaina, S.T. Nishanthi, Hirendra N. Ghosh, Menaka Jha. Black Gold decorated Zirconia: An efficient electrocatalyst for ethanol oxidation. *ACS Appl. Mater. Interfaces*, **2021**, 13, 8, 9942–9954.

8. Sunaina, Krishna K. Yadav, **Ankush**, Sujit Kumar Guchhait, Kritika Sood, S. K. Mehta A. K. Ganguli, and Menaka Jha* "Mechanistic insights of enhanced photocatalytic efficiency of SnO_2-SnS_2 heterostructures derived from partial sulphurization of SnO_2" *Separation and Purification Technology*, 2020, 242, 116835
9. Krishna K. Yadav, M. Sreekanth, **Ankush**, S. Ghosh, Menaka Jha. New Process for Stabilization of Vertically Aligned GdB_6 nanorods and their Field Emission Properties. *CrystEngComm*, **2020,** 22, 5473-5480.
10. Supriya Rana, Krishna K. Yadav, Kritika Sood, **Ankush**, S. K. Mehta, Menaka Jha. Low Temperature Hydrothermal Method for Synthesis of Fe_2O_3 and their Oxygen Evolution Performance. *Electroanalysis***, 2020,** 32, 1-8**.**
11. Krishna K. Yadav, Sujit Kumar Guchhait, Sunaina, **Ankush**, C. M. Hussain, A. K. Ganguli, and Menaka Jha* "Synthesis of zirconium diboride and its application in the protection of stainless steel surface in harsh environment", *Journal of Solid State Electrochemistry*, 2019, 23 (12), 3243-3253.
12. K. K. Yadav; G. Kumar; **Ankush**; A. Arora; S Ghosh and Menaka Jha*, "An insight of enhanced field emission from vertically oriented $La_XNd_{1-X}B_6$ nanorods", *Materials chemistry and Physics***,** 2022, 279, 125694.
13. K. K. Yadav; G. Kumar; **Ankush**; S Ghosh and Menaka Jha*, "Design of new process for stabilization of LaxGd1-xB6 nanorods and their Field Emission properties", *Mat. Sci. Eng. B***,** 2022**,** 282, 115759.
14. Nausad Khan, Krishna K. Yadav, Ritika Wadhwa, **Ankush**, and Menaka Jha*, One-pot green method for fabrication of MoS_2 decorated graphite rod and their application in H_2 evolution, *Material Letters*, 2022, 313,131784.